ABSTRACT

Title of Dissertation:	LIGHT-DRIVEN CHEMICAL CREATION OF FLUORESCENT QUANTUM DEFECTS
	Lyndsey Rae Powell, Doctor of Philosophy, 2018
Dissertation directed by:	Professor YuHuang Wang, Department of Chemistry and Biochemistry

Fluorescent quantum defects are emerging as a new frontier in nanoscience. In semiconducting single-walled carbon nanotubes (SWCNTs) these symmetry-breaking defects are introduced into the sp^2 carbon lattice, generating localized trap states for excitons. The emission from these states, which we call defect photoluminescence (PL), is only observed at very low defect densities, making precise control of the chemistry used to generate the defects imperative. In this dissertation I address the chemistry related to the generation of these defects in semiconducting SWCNTs. Typically, the organic reactions used to covalently modify SWCNTs are slow and imprecise, such as in the case of aryldiazonium chemistry. We use visible light that is tuned into resonance with SWCNTs to drive their functionalization by aryldiazonium salts and generate bright defect PL, accelerating the reaction and significantly improving the efficiency of covalent bonding to SWCNTs. We further expand this optical technique to another chemistry with which we demonstrate tunable switching

between the inactive and reactive isomers of a diazoether compound, for highly controllable modification of nanostructures. This technique is used to selectively functionalize a SWCNT chirality within a mixture, to the near exclusion of other chiralities, even among semiconductors that are nearly identical in diameter and electronic structure. Furthermore, we address the challenge of PL self-quenching in highly concentrated systems of carbon nanomaterials, which occurs fundamentally due to the spectral overlap in their emission and absorption spectra. We demonstrate that fluorescent quantum defects extend the PL-concentration linearity over a significantly wider range than their unmodified counterparts. This optical technique and chemistry provide opportunities to chemically tailor SWCNTs at the single chirality level for improved separations, passivation, and lithography, and for generation of bright defect PL, even within highly concentrated systems.

LIGHT-DRIVEN CHEMICAL CREATION OF FLUORESCENT QUANTUM DEFECTS

by

Lyndsey Rae Powell

Dissertation submitted to the Faculty of the Graduate School of the
University of Maryland, College Park, in partial fulfillment
of the requirements for the degree of
Doctor of Philosophy
2018

Advisory Committee:
Professor YuHuang Wang, Chair
Professor Philip DeShong
Professor John Fourkas
Professor Zhihong Nie
Professor Min Ouyang, Dean's Representative

Acknowledgements

First and foremost I must thank my two greatest supporters throughout this process, and my entire life for that matter, my parents. Their love, encouragement, and support have made this work possible. I am also grateful to Dr. Alexander Scammell whose encouragement and thoughtful advice have been a tremendous aid during my graduate career.

My advisor, Professor YuHuang Wang, has been an immense source of knowledge, inspiration, and guidance throughout my graduate career. I am consistently amazed at his persistence and creativity and am thankful for all he has done to help me succeed during my time at UMD. I am also appreciative of my committee members, Profs. Min Ouyang, Philip DeShong, John Fourkas, and Zhihong Nie, for their contributions and helpful advice related to this work.

During my graduate career I have been fortunate to have met and worked with many people who have provided me with insight, perspective, and support. Among the many I could list, I would especially like to thank Dr. Yanmei Piao, Allen Ng, Mijin Kim, and Dr. Hyejin Kwon.

I would also like to thank my undergraduate research advisor, Professor Robin Lammi, at Winthrop University. She provided me with the guidance, experience, and opportunities that I would not have had otherwise.

I also gratefully acknowledge the funding that I have personally received from the GAANN and the Millard and Lee Alexander Fellowships through the Department of Chemistry and Biochemistry. In addition, my research has been graciously supported

in part by the National Science Foundation (CHE-1507974), by the Air Force Office of Scientific Research (FA9550-16-1-0150), and by the National Institutes of Health (R01GM114167).

Table of Contents

List of Tables

List of Figures

.

List of Abbreviations

^{1}H-NMR: Proton nuclear magnetic resonance

(6,5)-SWCNT-$C_6H_4NO_2$: Notation used to describe the (6,5) single-walled carbon nanotube that has been covalently modified with nitroaryl functional groups

(n,m): Notation used to describe the chirality of the single-walled carbon nanotube by the 'n' and 'm' indices which denote the unit vectors along which a graphene sheet could be wrapped to generate the chirality

(SWCNT~D): Notation used to describe the physisorbed single-walled carbon nanotube and aryldiazonium molecule

(SWCNT-D): Notation used to describe the covalently bonded single-walled carbon nanotube and aryl functional group

6-31G(d,p): Split-valence basis set used to represent the electronic wave function in density functional theory

A: Absorbance

A: Pre-exponential factor

AFM: Atomic force microscopy

AQE: Apparent quantum efficiency

B3LYP: Becke, three-parameter, Lee-Yang-Parr Hybrid functional

CB: Conduction Band

D phonon: Symmetry-breaking, defect-induced Raman scattering, 1300 cm^{-1}

D: Deuterium

D/G: Ratio of the Raman disorder mode and G band

Defect PL: Defect photoluminescence

DFT: Density functional theory

DNA: Deoxyribonucleic acid

DOS: Density of states

DZ: Aryldiazonium salt

E: Energy

E: Notation describing the configuration of substituents about a double bond in which the two groups of higher priority are on opposite sides of the double bond

$\mathbf{E_{11}^-}$: Defect-induced intra-bandgap transition in SWCNT

$\mathbf{E_{11}}$: Excitonic SCWNT energy transition between the first valence and conduction band van Hove singularities

$\mathbf{E_{22}}$: Excitonic SWCNT energy transition between the second valence and conduction band van Hove singularities

$\mathbf{E_{33}}$: Excitonic SWCNT energy transition between the third valence and conduction band van Hove singularities

$\mathbf{E_a}$: Activation energy

$\mathbf{E_g}$: Band gap energy, energy difference between the top of the conduction band and the bottom of the valence band

eV: Electronvolt

FWHM: Full width at half maximum

G band: In-plane stretching mode, E_{2g}, of the sp^2-hybridized carbon lattice, 1590 cm^{-1}

h: Hour

HiPco: High-pressure carbon monoxide

HOMO: Highest occupied molecular orbital

Hz: Hertz

I_{11^-}: Intensity of defect photoluminescence (E_{11}^-)

I_{11}: Intensity of photoluminescence of the native SWCNT excitonic state, E_{11}

IFE: Inner filter effect

InGaAs: Indium gallium arsenide

J: Coupling constant

K: Kelvin

k_c: Rate constant describing the physisorption of the aryldiazonium to the carbon nanotube surface

K_{eq}: Equilibrium constant

k_p: Rate constant describing the covalent bonding of the aryl group to the carbon nanotube

L: Liter

LUMO: Lowest unoccupied molecular orbital

m: Meter

M: Molar

min: Minute

mol: Mole

MWCNT: Multi-walled carbon nanotube

NIR: Near-infrared

NO_2-BDT: *p*-nitrobenzenediazonium tetrafluoroborate

NO_2-DZE: 3-*O*-*p*-nitrobenzenediazoascorbic acid

P: Power

pH: The base 10 logarithm of the molar concentration of hydrogen ions

pK_a: Acid dissociation constant

PL: Photoluminescence

PMT: Photomultiplier tube

ppm: Part per million

ps: Picosecond

q: Charge

QY: Quantum yield

R: Gas constant

R^2: Coefficient of determination

RBM: Radial breathing mode

s: Second

SCE: Standard calomel electrode

SDS: Sodium dodecyl sulfate

SOMO: Singly occupied molecular orbital

SWCNT: Single-walled carbon nanotube

t: Time

T: Temperature

$t_{1/2}$: Half-life

UV: Ultraviolet

V: Volt

VB: Valence band

VHS: Van Hove singularity

vis: Visible

W: Watt

XPS: X-ray photoelectron spectroscopy

Z: Notation describing the configuration of substituents about a double bond in which the two groups of higher priority are on the same side of the double bond

δ: Chemical shift

λ: Wavelength

λ_{ex}: Excitation wavelength

λ_{max}: Wavelength of maximum absorbance

τ: Time constant

φ_{rel}: Relative quantum efficiency

Chapter 1: Fluorescent Quantum Defects

1.1 Defects in Materials.

1.1.1. A Brief History of Crystal Defect Chemistry.

At the start of the 20th century, intense research efforts were focused on the preparation and study of ideal, flawless crystalline inorganic materials. With this goal in mind, a defect, or any deviation from the flawless structure, was viewed as a deficiency. A mere 50 years later, a tremendous amount of effort was being poured into understanding the defects. A newfound interest in crystalline defects was brought about by the discovery that properties of the bulk crystal are ruled by the perturbations of defects.[1] In fact, researchers began to understand that they could use defects to their advantage by understanding how the properties of the material are determined by nature and density of the defects.

Defects can contribute to the optical, electrical, and physical properties of the materials. For example, in the extended sp^3 carbon lattice of diamond, sufficient doping with either the electron donor nitrogen or electron acceptor boron, gives the bulk crystal a yellow or blue color, respectively (Figure 1-1). Doping diamond with semiconductors such as Si or Ge gives the typically insulating material semiconducting properties. Substitutions in semiconductors permit fine tuning of the Fermi level for electrical devices and line dislocations make metals malleable.[2] Careful control of the nature and concentration of defects in materials imparts new functionality. It should be noted that

concentrations of the defects or dopants is crucial, especially in semiconductors. As the impurity concentration is increased above a certain limit, the atoms form a mid-band state, and the crystal loses its semiconducting character, becoming degenerate.[3]

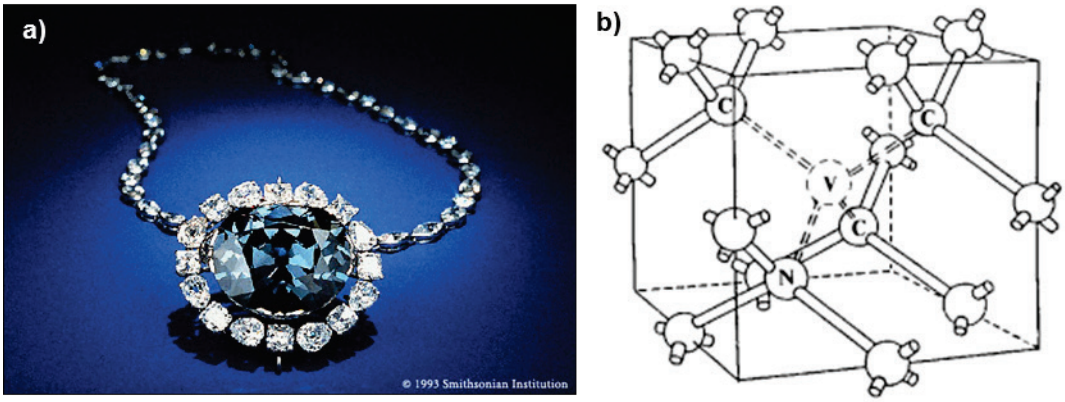

Figure 1-1. Defect crystal chemistry in the bulk 3-D regime. (a) The brilliant blue color of the Hope diamond, which is on display at the Smithsonian, is the result of a number of boron defects within its otherwise perfect sp^3 carbon lattice. Reproduced from ref. 4 with permission. (b) Interest in the nitrogen-vacancy defect in the diamond crystallographic unit cell has recently been renewed thanks to a better understanding of the defect's role in the crystal's properties.

1.1.2. The Impact of Material Dimensions.

Generally, the presence of defects at low concentrations has only a minor impact on the bulk material's properties, such that control of these defects is not critical to the material's performance. For example, even though a defect can theoretically trap or scatter charge carriers in an electrical circuit, the device can still perform well because these sites are electrostatically screened and so many other conduction channels exist.[5] However, these generalizations do not hold at reduced dimensions. One

might imagine that as the size of a crystal decreases, a single atomic defect would have a greater impact, as it represents a greater fraction of the overall crystal structure. In fact, the impact of a single defect at reduced dimensions is related to another factor, the Bohr radii of the wave functions of the charge carriers. The Bohr radius is defined as a distance between the electron and the hole and is unique to each material. As the size of the crystal approaches this Bohr radius the defect becomes more significant to the material's electronic structure. The wave functions become confined within the material's dimensions. In terms of the example of the electrical circuit given earlier, as the dimensions of the material with defects are reduced, fewer alternative conduction channels exist such that defects impact the performance of the device.

The impact of defects on material properties are seen from the bulk 3-D regime down to 0-dimensional materials such as quantum dots.[6] The relative density of defects quickly approaches a limit in which properties are substantially impacted at the nanoscale. At the critical length scale that approaches the Bohr radius in all dimensions, defects have the most impact. A defect's influence moves from the bulk internal lattice in 3-D materials to the material's surface in 2-D materials, and finally to the edge in 1-D and 0-D materials.

Defects in nanomaterials have recently become of interest to investigators. For example, Voiry *et al.*[7] used defects to change the character of layered materials, including as MoS_2, WS_2 and $MoSe_2$, from metallic to semiconducting and demonstrated strong and tunable photoluminescence (PL) from the modified material. In the regime of 1-D materials such as carbon nanotubes, defects from oxygen[8] and substituted aryl groups[9] result in new PL from an optically-allowed mid-gap state. In

2000, Kurtsiefer *et al*.[10] renewed interest in the diamond nitrogen-vacancy center (Figure 1-1) when they discovered that nanocrystals with this defect exhibit strong photon antibunching, making them of interest for quantum computing applications.

Our own interest in defects started with a discovery about semiconducting single-walled carbon nanotubes (SWCNT).[9] We found that covalently attaching conventional functional groups to the sidewall of a carbon nanotube can lead to the creation of an entirely new class of defect behavior. We call these defects *fluorescent quantum defects*. These molecularly tunable fluorescent quantum defects have exciting electronic and optical properties which will be discussed in this dissertation. In this chapter, I will review SWCNT properties, introduce the emerging field of fluorescent quantum defects, and briefly review current literature in this area.

1.2. Defects at the Nanoscale.

1.2.1. An Overview of Single-Walled Carbon Nanotube Structure and Optical Properties.

Carbon nanotubes are cylindrical nanostructures that are the one-dimensional analogs of graphite and graphene.[11] SWCNTs were first grown using transition metal catalysts by Bethune and Iijima in 1993.[12-13] Since that time, both single- and multi-walled carbon nanotubes have been extensively studied because of their remarkable mechanical,[14] electrical,[15] optical,[16] and thermal[17] properties. Physically, SWCNTs are quasi 1-D nanostructures consisting of a hexagonal network of carbon atoms in sp^2-hybridization. SWCNT length, depending on growth condition, can range from tens of nanometers to centimeters (Figure 1-2a). There are many structural varieties of

SWCNTs, each of which can be considered a unique molecule[18] whose properties vary widely depending on the orientation of its graphitic lattice with respect to the tube's longitudinal axis and diameter. These varieties are known as chiralities, and are denoted by their chiral vectors, given by two indices, *n* and *m* (Figure 1-2b). The physical structure of a SWCNT chirality dictates its electronic structure and whether it behaves as a semiconductor or metal.[19]

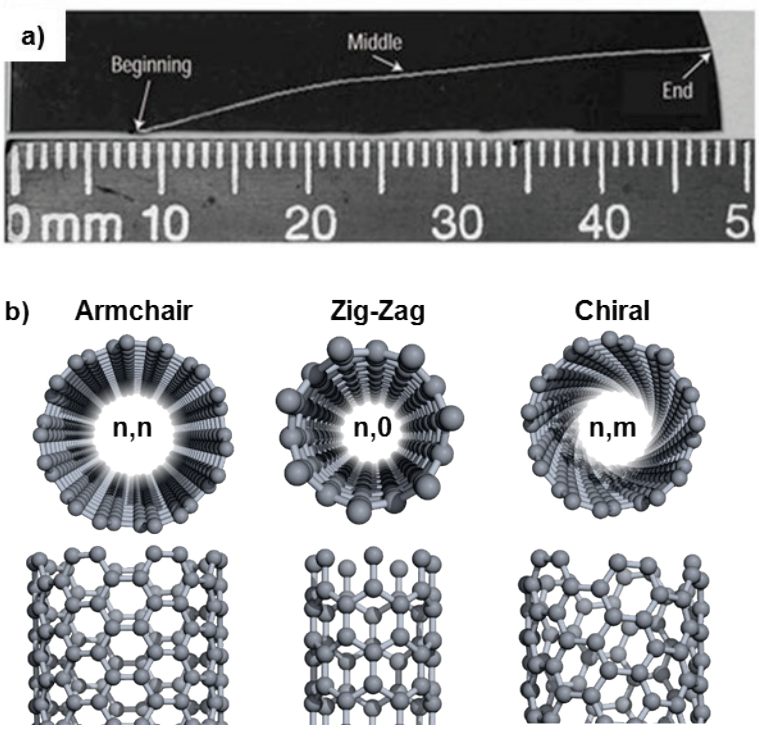

Figure 1-2. Physical structure of carbon nanotubes. Photograph of a 4-cm long multi-walled CNT on a Si substrate. The image of the CNT was formed by superimposing 230 scanning electron microscopy images on the photograph. Reproduced from ref. 20 with permission. (b) Molecular structures of different classes of SWCNTs including armchair and zig-zag (metallic) and chiral (semiconducting) show the many possible orientations of atoms in these nanomaterials. Simulations of molecular structures were performed on CNTbands 2.7.[21]

The electronic structure of nanomaterials varies from that of the corresponding bulk material. Unlike bulk materials with a direct band gap, excited charge carriers in SWCNTs are confined in all but one dimension (Figure 1-2), resulting in the formation of strongly bound and mobile excitons. Excitons are hydrogen-atom-like quasi-particles, bound by strong Coulomb interactions, each carrying a quantum of energy.[22] In semiconducting SWCNTs, excitons are delocalized along the tube's longitudinal axis (Wannier-Mott model)[23] and have strong binding energies (100s of meV; Frenkel model)[23-24] that depend on the chirality.

Because the dimensions of SWCNTs are on the order of the Bohr radius of the exciton, the exciton wave-function is strongly confined in all but the length dimension. This confinement effect results in splitting of the material's energy levels into discrete levels, known as Van Hove singularities, a non-smooth point in the density of electronic states (DOS). Consequently, the electronic structure of SWCNTs is marked by higher density of electronic states near the edges of the conduction and valence bands. The energy levels resulting from this splitting can be predicted using the particle-in-a-box model. Figure 1-3 shows how the reduced dimensions of 1-D and 0-D materials are reflected in their electronic density of states.

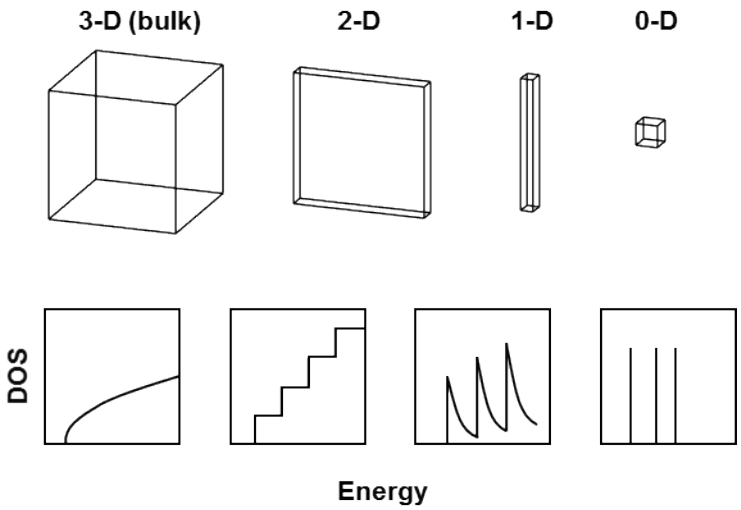

Figure 1-3. Quantum confinement effects on the electronic density of electronic states for materials of different dimensionality. Bulk materials display a continuous rise in available DOS at a given energy, in contrast to materials with reduced dimensionality, in which the DOS becomes more discrete with energy.

The discrete features observed in the optical spectra of isolated chiralities of semiconducting SWCNTs are made possible by their non-continuous DOS. Figure 1-4 shows the dramatic difference in the electronic structure of two SWCNT chiralities, (6,5) and (6,6), which are semiconducting and metallic, respectively. Note how similar the two species are aside from the difference in chiral angle (the arrangement of atoms with respect to the longitudinal axis of the SWCNT). Notably, the semiconducting chirality has a band gap, across which fluorescence can be observed (labelled E_{11}). In the metallic chirality, PL cannot be observed because of the non-zero DOS at the Fermi level (where E = 0 eV), preventing radiative recombination of the E_{11} exciton.

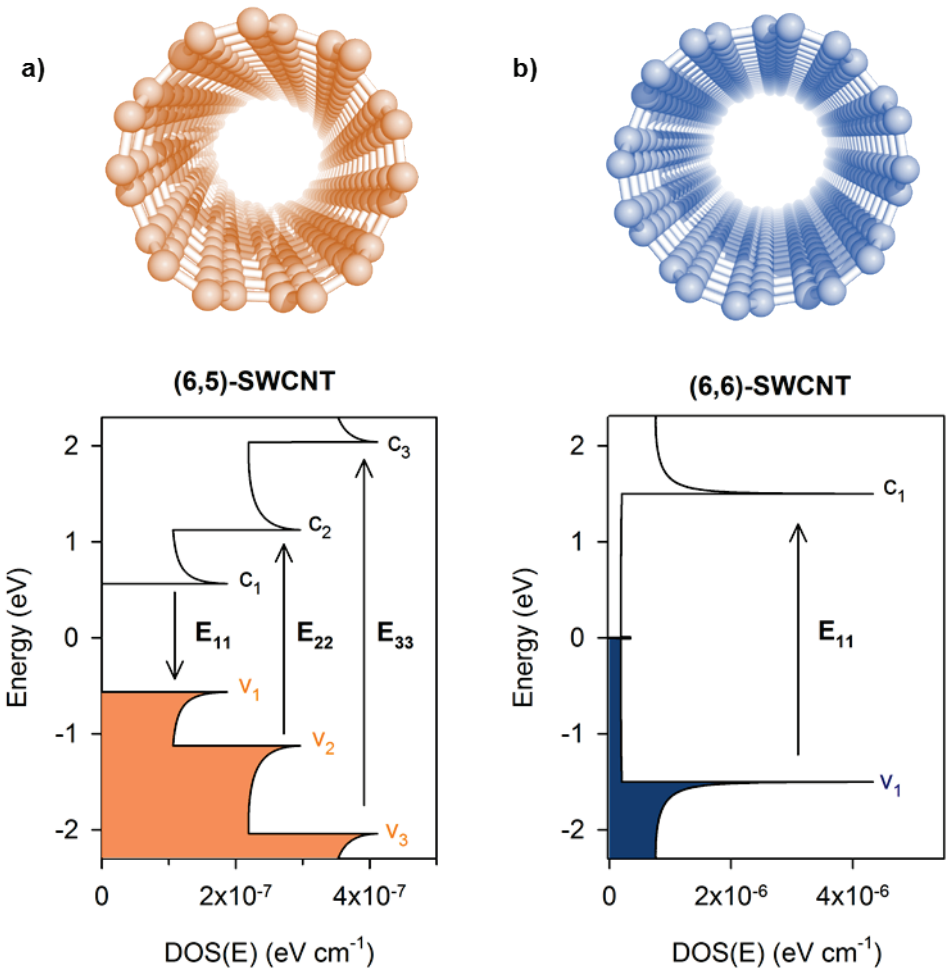

Figure 1-4. Electronic structure of SWCNT types. End-on view of the molecular structures of (a) a semiconducting (6,5)-SWCNT and (b) a metallic (6,6)-SWCNT. The correlated band structures of these SWCNTs (bottom) were computed with CNTBands 2.7 (ref. 25) using the Pz-orbital model simulation method, a 3 eV tight binding energy, and a 1.42 Å carbon-carbon spacing.

Suspension and separation techniques have made it possible to study systems enriched in individual chiralities of SWCNT via UV-visible-NIR absorption and NIR PL spectroscopy. In Figure 1-5, the separation of a surfactant-suspended solution of (6,5)-SWCNT by size-exclusion gel chromatography is characterized by the appearance of the true color of SWCNTs. (6,5)-SWCNTs absorb yellow-green light

(565 nm) at their E_{22} transition (labelled in Figure 1-4a), and consequently appear violet in solution. Figure 1-6 shows correlated UV-visible-NIR absorption spectra and PL excitation-emission maps of suspensions of SWCNTs before and after isolation. Only after separation are the discrete excitonic transitions resolved in the absorption spectra.

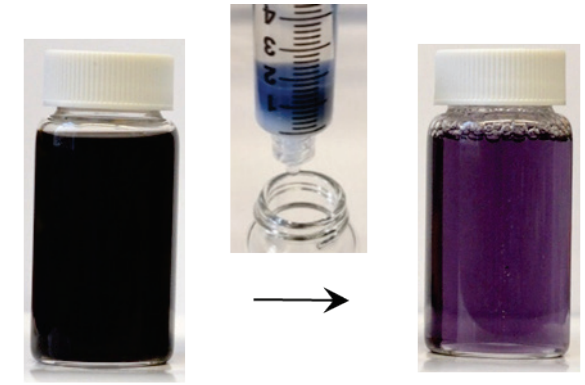

Figure 1-5. Enrichment of suspensions of HiPco SWCNTs with (6,5)-SWCNTs from unsorted suspensions of HiPco-synthesized SWCNTs by size-exclusion gel chromatography. The target chirality of SWCNTs, (6,5), preferentially binds to the gel material and is eluted to generate colorful solutions of semiconducting SWCNTs.

The band gap of a semiconducting SWCNT is typically on the order of 1 eV, and the radiative recombination of an exciton generates the emission of a photon in the NIR range (c_1 to v_1 transition termed E_{11}, see Figure 1-4a).[26] This NIR PL has made SWCNTs a target for research since it was first reported by Riggs *et al*.[16] in 2000. The excitonic origin of PL is SWCNT is supported by monoexponential decay kinetics.[27] Notably, the PL quantum yield (QY) of SWCNTs, < 1%, is far lower than expected for a direct-bandgap semiconductor.[26, 28] This low QY suggests that other non-radiative recombination pathways exist, the most significant of which is the presence of 'dark'

states that lie several meV below the bright exciton state (E_{11}).[29-30] Much study has been devoted to controlling the fate of excitons in SWCNTs and to improving the SWCNT's PL QY. PL brightness can be enhanced by various chemical treatments,[31] and isolation, and removal other quenching routes, but the overall PL QY is still low. Discovery of more methods for efficient PL in SWCNT is key to imaging,[32-33] molecular sensing,[34-35] and optoelectronics,[19] among other applications.

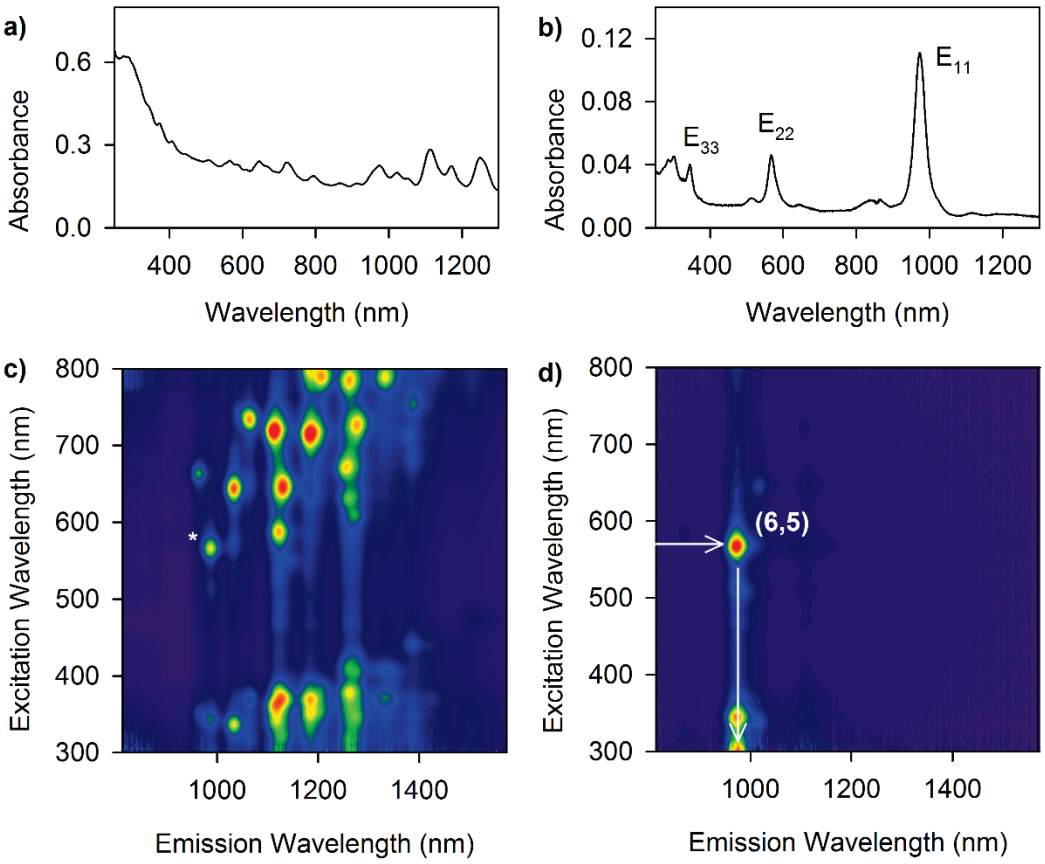

Figure 1-6. Spectroscopy of SWCNTs before and after separation by size-exclusion gel chromatography. (a), (b) UV-vis-NIR absorption spectra and (c), (d) NIR PL excitation-emission maps a, c before and b, d after isolation of the (6,5)-SWCNTs. Wavelengths corresponding to excitation at E_{22} and emission via E_{11} of the (6,5) chirality are denoted with arrows in (d).

1.2.2. Destructive Defects in Single-Walled Carbon Nanotubes.

Historically, the perception among nanomaterial researchers was that defects were something to be avoided. They focused on the growth of ideal carbon lattices, free from defects, which may have resulted from SWCNT synthesis and processing methods.[36-37] After all, the quality of the PL and electrical properties of SWCNT are sensitive to the presence of defects in their crystal structure. The negative connotation of defects in nanomaterials prevailed, especially as researchers sought to chemically modify SWCNTs to improve their solubility and chemical compatibility in various environments. Reports of the abrupt disappearance of optical features and electrical character upon covalent chemical modification were numerous. For example, covalent modification of SWCNTs has been shown to quench fluorescence in a step-wise manner[38] via a non-radiative relaxation pathway (Figure 1-7).[39] Crochet and co-workers monitored single-molecule chemical reactions of SWCNT with a diazonium salt through near-infrared PL microscopy. They observed discrete steps in the reduction of PL intensity among distinct segments of the SWCNT and attributed this phenomenon to the quenching of mobile excitons at localized sites. These results are in direct contrast to recent observations in which defects have unexpected and remarkable roles on the optical properties of SWCNTs.

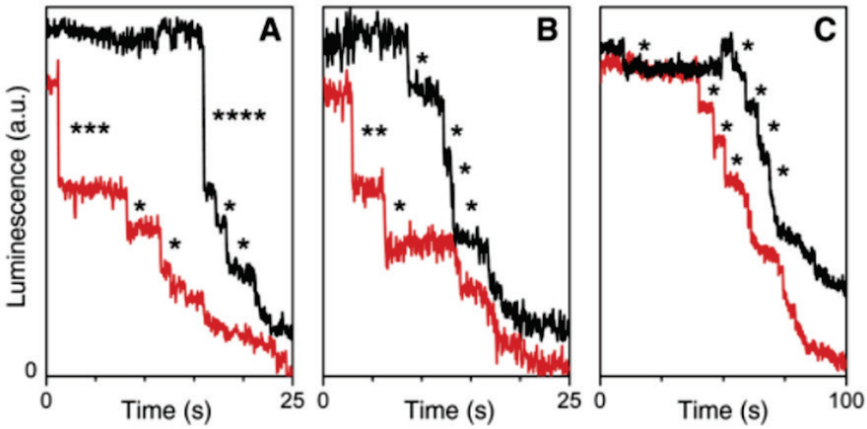

Figure 1-7. Localized quenching of PL from individual SWNTs upon covalent functionalization. Time-dependent PL of diffraction-limited segments of individual SWNTs is shown for (a) (8,3), (b) (8,6), and (11,1) chiralities upon addition of the diazonium salt solution. Each asterisk marks an elementary unit step. In each frame, the red (lower) and black (upper) traces correspond to adjacent segments (each 670 nm in length) of the same nanotube. The black traces have been shifted upward by one unit step for clarity. Reprinted with permission from ref. 38.

1.3. Fluorescent Quantum Defects.

1.3.1. Description of Fluorescent Quantum Defects.

The fluorescent quantum defects that are described in this dissertation have gone mostly unstudied until the last several years, due to the previous understanding that these defects, as distortions of the carbon lattice are detrimental. Here we demonstrate that implanted defects can also be beneficial. The discovery of fluorescent quantum defects provides a new method of tailoring excitons in nanomaterials. These defects can be implanted on SWCNT sidewalls by a variety of chemistries at densities of less than 1 defect per 20 nm of SWCNT length.[9] Figure 1-8 shows a schematic of a

fluorescent quantum defect on an isolated (6,5)-SWCNT. The mobile E_{11} exciton is able to diffuse along the quantum cylinder, until it reaches a fluorescent quantum defect. At this sp^3-hybridized site, the exciton becomes trapped in a quantum well whose depth is proportional to the inductive electronic effect of the defect (shown as a red atom in Figure 1-8 for the sake of clarity). The exciton can then relax back to the ground state via an optically-allowed intraband gap transition (labelled E_{11}^-). The red-shifted emission from this state, which we term *defect PL*, typically lies in the NIR region. One can imagine that this strategy could result in a vast number of new materials because each semiconducting SWCNT chirality may be modified with a broad range of chemical functionalities. Recent PL imaging studies of defects in SWCNT have demonstrated that the defects function as trapping sites for excitons and that emission from the defect-induced state is localized to the defect site.[40] In contrast, SWCNT's intrinsic emission is delocalized throughout the length of the tube.

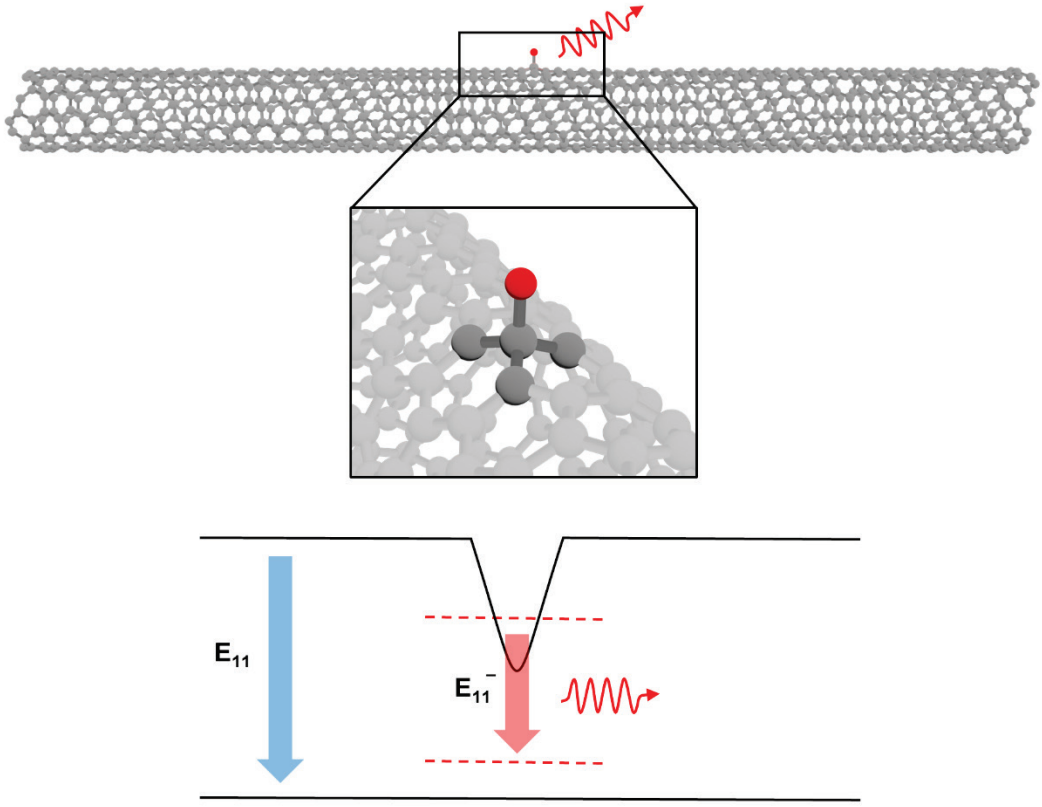

Figure 1-8. A fluorescent quantum defect. The introduction of a sp^3-hybridized defect breaks the symmetry of the otherwise sp^2-hybridized SWCNT lattice, generating an energetic trap state at the site of the defect. In the schematic, the 1-D exciton diffuses along the pristine region of the SWCNT, before becoming trapped at the defect site, where it emits via the tunable state, E_{11}^- (blue), generating defect PL.

1.3.2. Fluorescent Quantum Defect Chemistries.

Although the chemical activity of SWCNTs has been intensively investigated, fewer chemistries have been demonstrated for the generation of fluorescent quantum defects. This is because many of the previous chemistries may quickly produce defect densities which exceed the threshold of defect PL. A lack of available techniques to monitor the reactions at these defect densities is likely another contributor. Fluorescent

quantum defects have been with introduced with diazonium salts,[9, 41] hexanoic acid,[42] and alkyl halides.[43] Expanding the range of chemistries and developing new methods for controlling these defects is essential for realizing the extent of tunability that this new material engineering approach has to offer.

In 2010 Ghosh *et al.* demonstrated that ozonation[8] introduces a new peak, which they term E_{11}*, due to oxygen dopants such as ozonides, epoxides, and ethers. Their effect is described as similar to the case of the sp^3 defect described earlier, causing energy-level splitting and local trapping of excitons that can then emit radiatively. However, in an explanation in a recent work by Miyauchi and colleagues,[44] semi-empirical PM3 modelling suggests that the oxygen atom is instead incorporated into the SWCNT's sp^2-hybridized lattice and the symmetry of the SWCNT is not broken, a key distinction in its structure from the case of sp^3 defects. Furthermore, the position and intensity of the oxygen-dopant-induced PL peak are not chemically tunable.

In 2013, Piao *et al*.[9] used substituted aryldiazonium salts to introduce defects with remarkable tunability, in terms of emission position (up to 250 meV) and intensity (up to 28-times brighter than the intrinsic PL, E_{11}). Normally, the efficiency of PL in SWCNTs is quite low due to the presence of non-radiative, 'dark' states that lie below the bright E_{11} exciton. Interestingly, the trap state can be engineered to lie energetically below these new optically allowed states to provide an energetic outlet in the system. Piao *et al*. also achieved remarkable tunability in terms of emission energy by attaching functional groups with different substituents to SWCNTs. They found that the depth of the trap state was based on the electron-withdrawing nature of the functional group.

The work of Piao *et al*. lays a foundation for chemical creation and control of defect quantum states in low-dimensional carbon materials.

In 2016, Kwon *et al.*[43] expanded the diversity of nanostructures even further. They developed a highly adaptable chemistry making use of alkyl halides to generate more than thirty unique nanostructures and characterized the exceptional properties of the new chemically-modified nanomaterials.[43] That study expanded our understanding of how the inductive effect is related to the chemical nature of the defects and the depth of the trap state. Kwon *et al*. also elucidated the role of divalent defects in SWCNT, finding that they generate even deeper traps for mobile excitons. Further pushing defect PL into the NIR range is important for applications in imaging[40] and telecommunications as well.[45]

1.3.3. Spectroscopic Characterization of Fluorescent Quantum Defects.

It has been well established that chemical modifications of nanotube surfaces can controllably modulate optical properties, but there is still much to be explored. Beyond the fundamental benefit of a new red-shifted emission route for SWCNTs lie other spectroscopic features and characteristics that make defect PL both fundamentally and practically interesting. Principal among these advantages is the relative position of the defect state, which lies below 'dark' states such that PL can be brightened substantially.[8-9] Considerable work has shown that defect PL can be tuned based on the chemical nature and geometry of the defect,[9, 43] but the limits of this effect have yet to be thoroughly investigated.

The potential to excite SWCNTs in the NIR at E_{11} (versus in the visible at E_{22}) and to observe PL via E_{11}^- is another interesting byproduct of this defect state. This possibility increases the number of spectrally distinct NIR imaging probes, and may be important for bioimaging and for developing signature fluorescent probes in the NIR.

Recently, it was found that defect PL decays biexponentially, with a long component that extends the PL lifetime of the system to 100s of ps. Such as long lifetime is a requirement to achieve lasing.[46] It has been shown that defect PL behaves nonlinearly with excitation power density[47] and that it assists in up-conversion of their PL.[48] Most recently, studies of fluorescent quantum defects have moved toward answering important fundamental questions such as the redox potential of defect states[49] and how the defects affect vibrational reorganization energies.[50] These types of discoveries may enable the applications of fluorescent quantum defects such as optoelectronics and deep-tissue PL imaging.

1.3.4. Applications of Fluorescent Quantum Defects.

The NIR emission of SWCNTs may enable applications ranging from imaging,[40] to sensors, to telecommunications, to night vision.[45] Defect PL provides a route to realization of these goals. Kwon *et al*.[51] describe a pH and temperature sensor consisting of amine-functionalized SWCNTs. A major advantage of a NIR PL probe for *in vivo* imaging is that defect PL lies within the biological window, where absorption and fluorescence from biological media are minimal. These sensors are able to spectroscopically monitor pH and temperature of solutions, using the intrinsic PL of SWCNT as an internal standard. The defect PL shifts by as much as 33 meV throughout

the biological pH window (pH 4.5 to 8.5), allowing for reliable resolution of pH changes as small as 0.2 pH units. The sensors can function in a biological medium at high salt concentration. Because the response of the sensors is localized at the sensing functionality, the signal may be more sensitive than other bulk methods.

In 2015, Ma *et al*.[52] demonstrated that oxygen-dopants can function as single photon-sources at room temperature. Although single photon emission had been demonstrated previously for SWCNTs at cryogenic temperatures,[53] the work of Ma *et al*. was the first to exploit these defect states were exploited to trap excitons, permitting antibunching of emitted photons.[52] New experimental results suggest that fluorescent quantum defects can enable the production of even brighter single-photon emitters, as proposed by us in 2013.[9]

1.4. Challenges for Fluorescent Quantum Defects Addressed in this Dissertation.

Fundamental challenges in carbon nanochemistry are the control and understanding of how a chemical reaction progresses on the sp^2 carbon lattice and how the chemistry can be controlled for targeted applications.[54] This dissertation will address these questions by making use of fluorescent quantum defects. The projects are also aimed at addressing critical technical challenges directly related to the incorporation of fluorescent quantum defects into potential applications. In Chapter 2, light is used to drive covalent modification of SWCNT by aryldiazonium salts, improving the reaction rate and efficiency. Significantly, the light used to drive these chemical reactions is resonate with the nanostructures, rather than the aryldiazonium salts. In the Chapter 3, this optical technique is expanded to a diazoether chemistry.

The controlled modulation between an inactive isomer and a reactive isomer of a diazoether compound is probed and used to drive preferential chemical modification of an otherwise less reactive SWCNT chirality in a mixture. In the Chapter 4, the challenge of obtaining quantitative PL measurements in highly concentrated systems of nanostructures is addressed. The quenching effect is reduced via the localized emission from defect PL and an effective increase in the Stokes shift of the system. The linear response range for PL with concentration is extended, SWCNT PL brightness is enhanced, and the effect is also observed in the dense environment of a film of SWCNTs. In Chapter 5, a brief summary and outlook for the future of fluorescent quantum defects is provided, both within our own lab and beyond.

Chapter 2: Optical Excitation of Carbon Nanotubes Drives Their Functionalization by Aryldiazonium Chemistry

The major results presented in this chapter are adapted from: L. R. Powell, Y. Piao, and Y. Wang. The Journal of Physical Chemistry Letters, 2016, 18, 3690-3694.

L.R.P. designed and performed experiments. L.R.P. and Y.W. wrote the manuscript with input from all authors.

2.1. Introduction

Organic reactions have been widely used to modify carbon nanomaterials such as single-walled carbon nanotubes (SWCNTs) and graphene. Covalent attachment of functional groups to SWCNTs can improve their solubility and chemical compatibility.[55-57] However, these new functionalities are typically achieved at the expense of the remarkable electronic and optical properties of SWCNTs. Our recent experiments[9] demonstrate that controlling the functional degree of SWCNTs by diazonium reactions leads to the creation of bright, fluorescent quantum defects. This discovery has motivated a series of new experiments[40, 43, 47, 50, 54] for exciting new opportunities to directly tailor the electronic and optical properties of low dimensional carbon materials through organic chemistry. However, diazonium reactions, and covalent chemistries in general, lack the precision and efficiency required to directly tailor carbon nanomaterials. Here we show that by optically exciting SWCNTs, the creation of fluorescent quantum defects by aryldiazonium salts is accelerated significantly by means of photothermal and electronic mechanisms.

Functionalization of SWCNTs using aryldiazonium salts typically results in low grafting yields[9, 58] due to their susceptibility to self-polymerization and rapid decomposition. This low yield hinders precise control of their functional degree, particularly in the low defect density regime. Although diazonium chemistry can be accelerated electrochemically or by using UV excitation of the salt,[55, 59] these techniques may result in uncontrolled functionalization and high defect densities.

Few optical methods to trigger covalent chemistries on carbon nanomaterials have been reported.[60-61] In the case of SWCNT, the light was used to target the bonding moiety,[59] generating reactive species that impede control of the reaction. Our optically-triggered reaction is instead driven by light that directly targets the SWCNT. The irradiation results in a reaction that is faster and generates brighter defect PL than when left in the dark. Furthermore, the functional degree depends on the photon energy and the extent to which it resonates with chirality-specific optical transitions of the SWCNT.

It is particularly challenging to control the degree of covalent functionalization in the low functional degree regime due to lack of sensitive techniques to monitor reactions. This challenge is addressed here by following the rise of the distinctive defect PL (E_{11}^-), which occurs at a wavelength that is redshifted from that of the native exciton (E_{11}). E_{11}^- signals the covalent bonding of aryl groups to the sp^2 lattice of SWCNTs.[9] This allows the progress of the reaction to be monitored *in situ*, and defect PL to be used as a quantitative indicator of the reaction progress.

2.2. Experimental Methods

2.2.1. Preparation of Suspensions of Chirality-Enriched SWCNTs.

Chirality-enriched SWCNT samples were separated from high-pressure carbon monoxide (HiPco) SWCNTs (Rice University, Lot 194.3) using an adapted gel chromatography procedure.[62] We isolated (6,5)-SWCNTs on a Sephacryl S-200 HR column (GE Healthcare). The SWCNTs used in these experiments were individually suspended by 1% wt./v sodium dodecyl sulfate (SDS, Sigma-Aldrich, 99%) in 99.8% deuterium oxide (D_2O, Cambridge Isotopes, Inc.). The absorbance of the (6,5)-SWCNT solution was adjusted to 0.12 (1 cm optical path length) at E_{11}, corresponding to a carbon concentration of approximately 0.66 mg L^{-1}.[62]

2.2.2. Synthesis of *p*-nitrobenzenediazonium tetrafluoroborate.

p-nitrobenzenediazonium tetrafluoroborate (NO_2-BDT) was synthesized as previously reported[63] from *p*-nitroaniline (99%, Sigma Aldrich) and nitrous acid (48 wt.% tetrafluoroboric acid solution in water, Sigma Aldrich; sodium nitrite, 97%, Sigma Aldrich). The salts were stored at 0 °C until immediately before use.

2.2.3. Optically-Driven SWCNT Functionalization.

An aliquot of 50 μM NO_2-BDT in D_2O was added to a suspension of chirality-enriched (6,5)-SWCNT in a capped 1 cm quartz cuvette, which was stirred and protected from ambient light, by covering the cuvette with aluminum foil, at 21 °C. The addition of the NO_2-BDT solution resulted in less than a 0.3% increase in volume, which avoided significantly changing the concentration of SWCNTs. The temperature of the solution was maintained (at 21 °C unless otherwise noted) throughout the

experiment using a circulating water bath (FL-1027, Horiba Jobin Yvon and Fisher Scientific Isotemp 3016D). The solution temperature was monitored with a LabQuest 2 module and temperature sensor (Vernier). The capped solution was stirred for 20 min with protection from light to allow the aryldiazonium to diffuse to the SWCNT surface. The samples were then continuously irradiated (or protected from light in the case of the dark controls) with the monochromator-selected (10 nm bandpass; 565 nm, 11.5 mW cm^{-2} unless otherwise noted) output from a 450 W Xenon arc lamp (Ushio) for the course of the reaction until the defect PL stabilized. Samples were monitored spectroscopically, infrequently to avoid light contamination, by periodically measuring the PL (see "Spectroscopic Characterization of the Reaction"). Notably, the solutions exhibited stable PL over a period of more than 6 months. The solutions were protected from ambient light and reactions were monitored and characterized spectroscopically.

2.2.4. Power Density Experiments.

Absorptive neutral density filters (Edmund Optics) were placed in the beam path of the incident irradiation to change the irradiation power density. The power density was measured with a calibrated optical power meter (Newport 1916-C) and silicon detector (Newport 918-SL-OD3). All experiments were performed at 21 °C and irradiated throughout the course of the reaction, until defect PL stabilized. The molar ratio of reactants, [NO_2-BDT]:[SWCNT carbon], is 1:500 and 565 nm light was used for these experiments.

2.2.5. Wavelength Dependence Experiments.

Samples were prepared as outlined in "Optically-Driven SWCNT Functionalization" and continuously irradiated with the monochromator-selected (10 nm bandpass) output of the Xenon arc lamp at 21 °C. Each sample was irradiated for the same time period (12 h). The dark control sample was protected from light and measured after 400 h. The molar ratio of reactants is 1:500 for these experiments.

2.2.6. Temperature Dependence Experiments.

A circulating water bath was used to control the temperature of the (6,5)-SWCNT solution within a capped 1 cm quartz cuvette with stirring. The sample was protected from light. Then, an aliquot of 50 μM NO_2-BDT was added to the SWCNTs so that the molar ratio of reactants was 1:500 and the cuvette was capped. The suspension was protected from ambient light for 20 min before being either irradiated with monochromator-selected 565 nm (10 nm bandpass) light or protected from light throughout the course of the reaction. The defect PL was monitored until stable. The temporal evolution of defect PL was fit to an exponential function as outlined later in the text. Note that the PL measurements were taken at the same temperature as the reaction condition to avoid disturbing the reaction and that SWCNT PL is temperature-dependent. The molar ratio of reactants is 1:500 for these experiments.

2.2.7. Spectroscopic Characterization of the Reaction.

Fluorescence spectra and excitation-emission maps were collected on a HORIBA Jobin Yvon Nanolog Spectrofluorometer equipped with a 450 W Xenon arc lamp and a calibrated multichannel InGaAs array detector. Samples were monitored

spectroscopically, infrequently to avoid light contamination, by periodically stopping the irradiation (or protection from light in the case of the dark controls) and measuring the PL (1 s integration time, 565 nm excitation wavelength). The duration of this process was ~20 s per measurement. Note that the reported PL intensities are peak intensities. Ultraviolet/visible/near-infrared (UV-vis-NIR) absorption spectra were measured using a PerkinElmer Lambda 1050 UV-vis-NIR spectrophotometer equipped with a photomultiplier tube and a broadband InGaAs detector after the reaction stabilized.

2.3. Results and Discussion

2.3.1. Optically-Driven Functionalization of SWCNTs.

Figure 2-1a outlines the optically-driven reaction, in which the covalent bonding of an aryl group to the SWCNT occurs by irradiation with light that is tuned into resonance with the nanotube. The optical absorption spectra of the isolated starting materials in Figure 2-1b reveal that the SWCNT can be excited to the exclusion of the aryldiazonium salt at either the second, E_{22} (565 nm; 2.19 eV) or first, E_{11} (980 nm; 1.27 eV) optical transitions of the nanotube. In this study the (6,5)-SWCNT was used as a model system, but our concept can be readily applied to other nanotube chiralities. The nanotubes were stabilized by SDS as individual particles in D_2O. The reaction is initiated by adding an aliquot of a freshly prepared solution of NO_2-BDT to the suspension of SWCNTs and irradiating the solution with light.

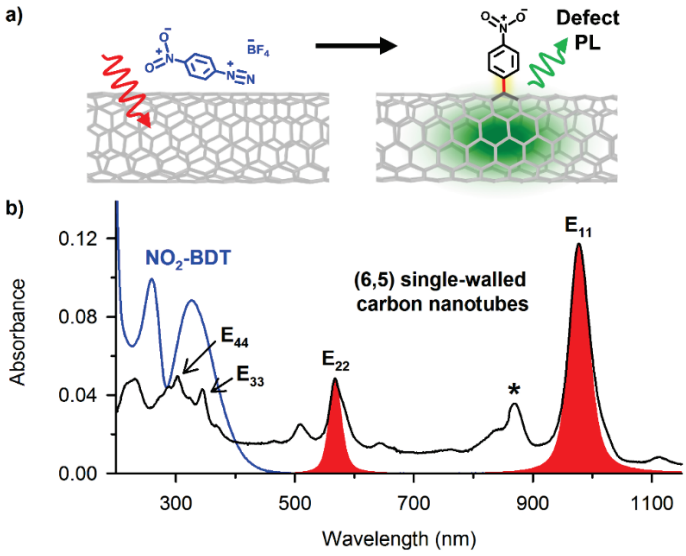

Figure 2-1. Resonant excitation of a SWCNT with light drives covalent functionalization on the sp^2 carbon lattice by diazonium salts.(a) The schematic shows a region of a (6,5)-SWCNT where a NO_2-BDT molecule is converted to a covalently bonded nitroaryl functional group upon irradiation with light which resonates with the chirality-specific excitonic transitions of the SWCNT. This chemistry creates a fluorescent quantum defect whose defect PL at E_{11}^- is used to monitor the reaction. (b) Absorption spectra reveal that (6,5)-SWCNT (black line) can be excited to the exclusion of the NO_2-BDT (40 μM in D_2O, blue line) at either its E_{22} or E_{11} optical transitions (red shaded peaks). The asterisk indicates minor (6,4)-SWCNT content.

In our first experiment we used light was resonant with the E_{22} optical transition of the (6,5)-SWCNTs, 565 nm, sourced from the monochromator-selected (10 nm bandpass) output from a 450 W Xenon arc lamp (Figure 2-2). The reaction was monitored *in situ* by following the evolution of defect PL at E_{11}^- (1140 nm, 1.09 eV in the case of nitroaryl defects) over time, with care taken to minimize light exposure for the controls.

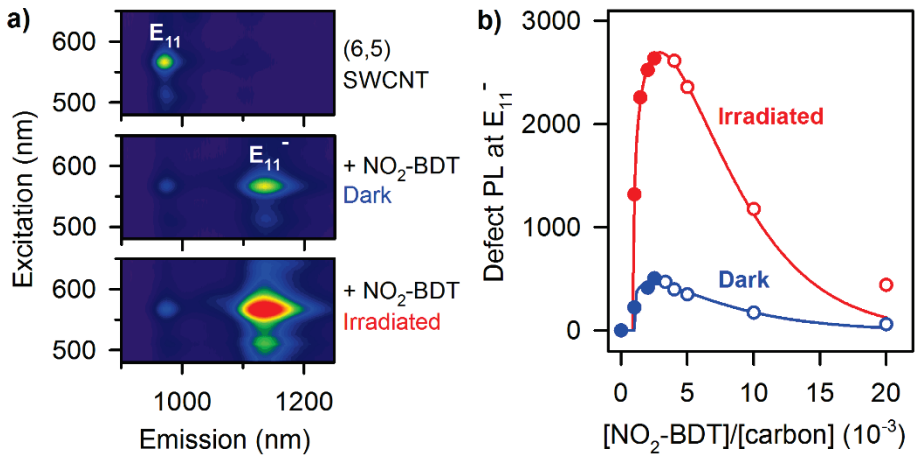

Figure 2-2. Irradiating SWCNTs with light significantly brightens their defect PL. (a) PL excitation-emission maps of (6,5)-SWCNTs that were pristine (top), functionalized under 400 h of protection from light (middle), or functionalized under 12 h of irradiation (bottom). The molar ratio of reactants, [NO_2-BDT]:[SWCNT carbon] is 2.5 × 10^{-3} (1:400). (b) The defect PL intensities (565 nm exc.) vary with the amount of the diazonium salt added after the reaction stabilizes (single experiments) both when irradiated (565 nm) or kept in the dark. Filled circles denote region where functional degree is positively correlated to defect PL. Data points refer to data collected from single experiments.

The PL excitation-emission maps in Figure 2-2a demonstrate that functionalization resulted in defect PL at E_{11}^- and that the irradiation resulted in brighter defect PL versus the dark control. The observed defect PL originates from covalent nitrobenzene defects, not from physically adsorbed diazonium or photo-oxidation of the SWCNT, as confirmed in our previous chemical composition studies that used Raman scattering and X-ray photoelectron spectroscopy.[9] The nitroaryl defect PL is 19 meV red-shifted from that of O-doped (6,5)-SWCNTs (1140 nm versus 1120 nm[8]).

Notably, our light-driven reaction produces much brighter defect PL than the dark control over the range of relative reactant concentrations tested (Figure 2-2b). In

the cases of both irradiated and dark (control) conditions, the intensity of defect PL maximized at a reactant molar ratio, [NO_2-BDT]:[SWCNT carbon], of 2.5 × 10^{-3} (1:400) before rapidly decreasing with increasing amounts of NO_2-BDT. We note that the intensity of defect PL is positively correlated to the functional degree for cases where the relative concentrations of reactants are less than the maximum defect PL intensity.[9] The experiments discussed in this work are carried out so that defect PL intensity is correlated quantitatively to functional degree.

The native E_{11} exciton is quenched with increasing amounts of NO_2-BDT added (Figure 2-3). SWNT PL occurs via an exciton recombination process, and is sensitive to not only covalent defects but also to adsorbed dopants, include aryldiazonium salts.[64]

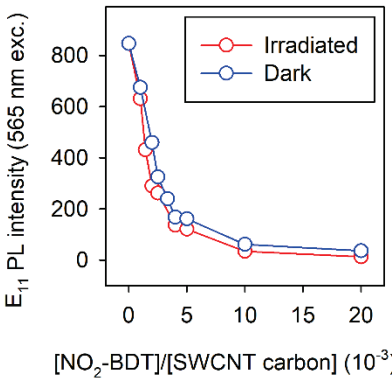

Figure 2-3. PL from E_{11} is quenched with NO_2-BDT added, whether irradiated (565 nm) or protected from light.Measurements were taken after the reaction completed.

The PL excitation-emission maps in Figure 2-4 clearly demonstrate that the new PL peak is red-shifted directly from E_{11}, and it demonstrates the dramatic effect of irradiation on the brightness of the defect emission state.

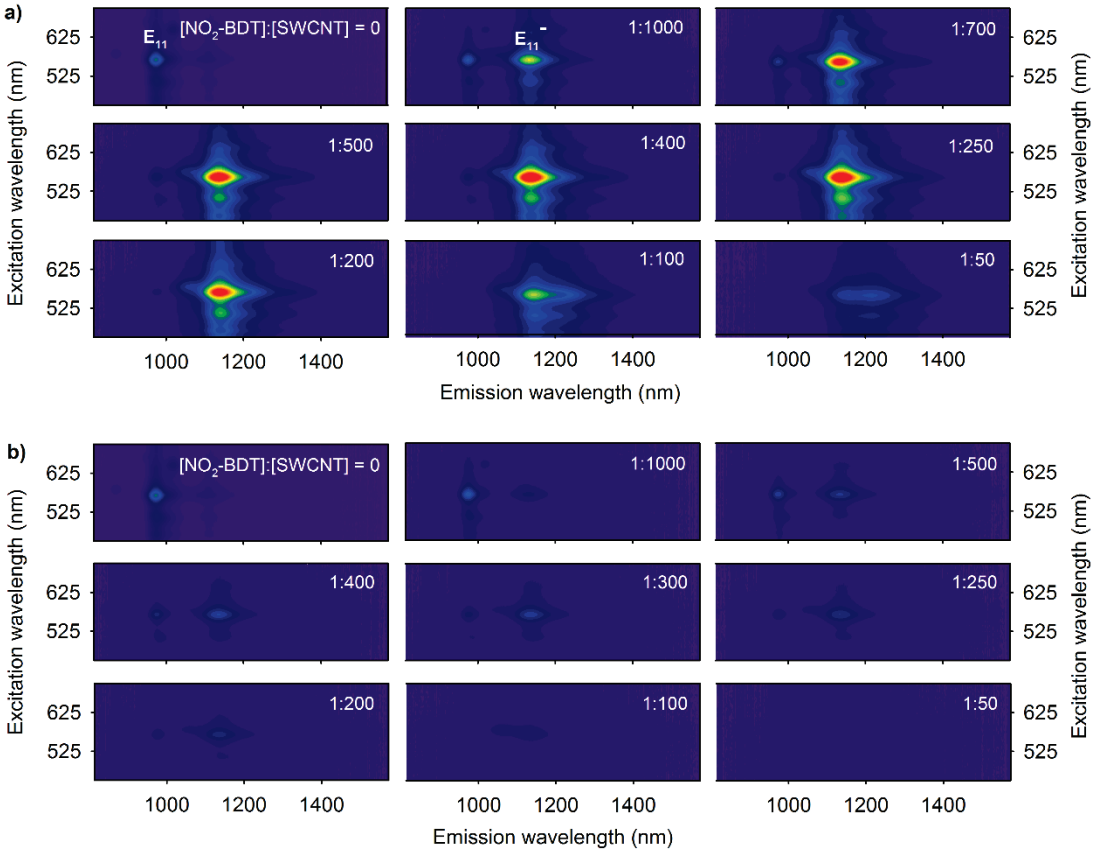

Figure 2-4. PL excitation-emission maps of (6,5)-enriched SWCNT solutions with various amounts of NO_2-BDT. Functionalization was effected either under (a) E_{22}-resonant irradiation (565 nm) or (b) protection from light. Measurements were made after the reaction completed. The PL intensity scale is the same for all maps.

The UV-vis-NIR absorption spectra reveal the changes in the (6,5)-SWCNT's E_{11}^-, E_{11}, E_{22}, and E_{33} states with different amounts of diazonium salt added (Figure 2-5). The absorbance of the E_{11}, E_{22}, and E_{33} states decreases with increasing functional degree. Notably, the absorbance cross-section of the E_{11}^- state is extremely low. A peak is not well-resolved at a position corresponding to the defect state because the density of functional groups is extremely low relative to that of the bulk carbon lattice. The

defect density is approximately 1 defect per 20 nm of SWCNT length, as was approximated by previous X-ray photoelectron spectroscopy studies.[9]

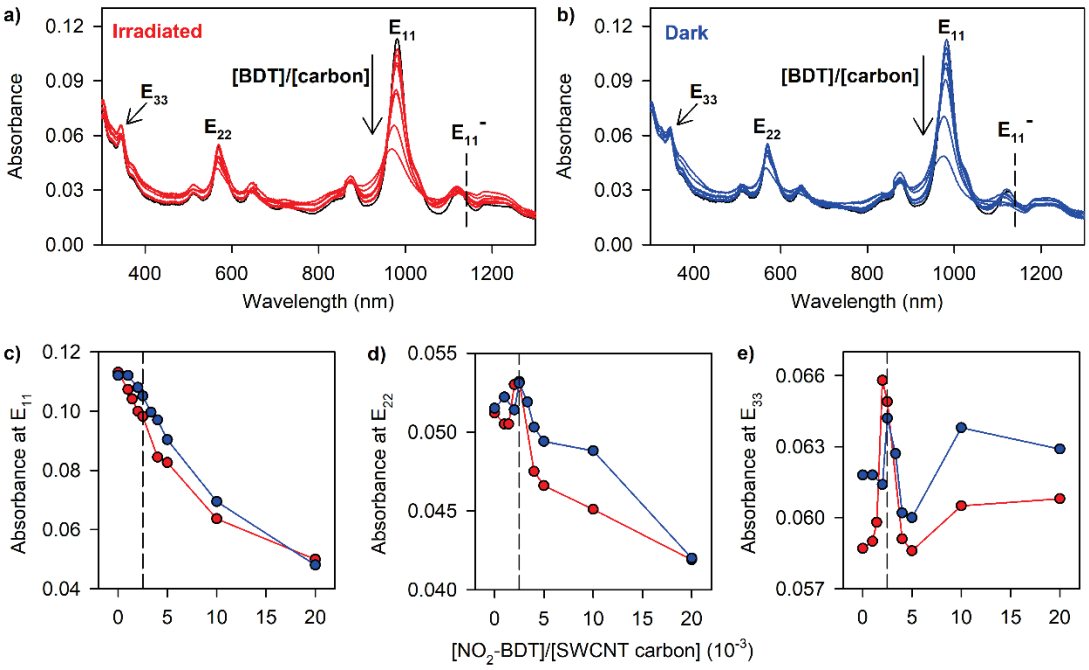

Figure 2-5. UV-vis-NIR optical absorption spectra of solutions of (6,5)-enriched SWCNTs and various amounts of NO_2-BDT. Solutions were either (a) irradiated with 565 nm light or (b) kept in the dark. Spectra were taken after the reaction completed. Peak absorbance values for single experiments at (c) E_{11}, (d) E_{22}, and (e) E_{33} are plotted versus the relative ratios of reactants. The molar ratio which produced the most intense defect PL is indicated by the vertical dashed lines in (c), (d), and (e) for reference.

In the absence of light, the conversion of diazonium to covalently bonded aryl groups was inefficient even with increasing relative concentrations of diazonium salt (Figure 2-3b), as the defect PL is never as bright as when irradiated. However, we found that we could drive covalent bond formation long after the defect PL stabilized in the dark control. Upon irradiation of a solution of SWCNT and NO_2-BDT which was aged

in dark for 6-weeks, there is a 2-fold increase in the intensity of defect PL (Figure 2-6). This may be due to the conversion of long-lived adsorbates into covalently bonding functional groups by light. This type of long-lived species may find applications in nanostructure lithography allowing for direct application of conventional photolithography tools to pattern chemical functionalities on carbon nanostructures. Ongoing studies are aimed at this long sought-after goal.

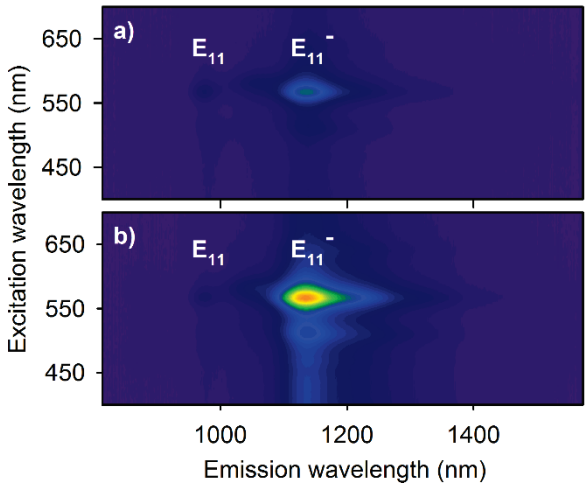

Figure 2-6. E_{22}-resonant light (565 nm) is used to drive functionalization of a 6-week aged sample (protected from light) of (6,5)-SWCNTs and NO_2-BDT. (a) When the aged sample is (b) irradiated for 4 h, bright defect PL at E_{11}^- is generated, whose position is consistent with that of covalent nitrobenzene defects.

2.3.2. Reaction Dependence on Photon Energy.

In order to evaluate possibility of a photo-induced electron transfer mechanism, we performed experiments using different irradiation energies. The defect PL intensities of solutions of reactants were measured (565 nm exc.) after irradiation with different photon energies. We calculated the apparent quantum efficiency, AQE, a

measure of the efficiency of the conversion of absorbed incident photons to covalent bonds by eq. (2-1).

$$AQE = \frac{I_{11-}(\lambda) - I_{11-}(dark)}{N} \quad (2\text{-}1)$$

in which $I_{11-}(\lambda)$ and $I_{11-}(dark)$ are the intensities of defect PL obtained after effecting reaction with either irradiation at wavelength, λ, or protection from light, respectively. N, the number of incident photons, normalizes the measurement for the different irradiation energies and was calculated based on the power of the light. The incident powers at 312 and 345 nm were extrapolated based on the output spectrum of the Xe arc lamp because these energies lie outside of the power meter's calibration. All samples were irradiated for the same length of time (see Experimental Methods). The resulting plot of AQE versus irradiation energy is overlaid with the optical absorption spectrum of the (6,5)-SWCNTs used in this study (Figure 2-7).

Notably, an increase in photon energy results in an increase in AQE. This suggests that the optically-driven reaction occurs, at least in part, by a photothermal energy transfer mechanism, as an increase in the number of photons drives the reaction. However, a closer examination reveals that upon varying the photon energy of the incident radiation, the AQE plot closely traces the absorption spectrum of unfunctionalized (6,5)-SWCNTs, with the maxima matching those of the SWCNT's E_{33} and E_{22} optical transitions. This suggests that the reaction has some degree of an electronic mechanism, in which the incident photons must be in resonance with the SWCNT lattice in order for the reaction to occur.

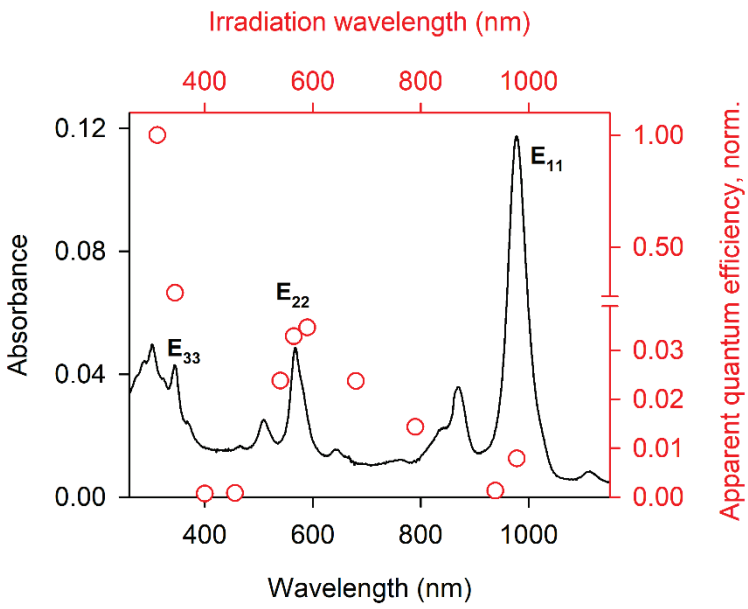

Figure 2-7. Functionalization of (6,5)-SWCNTs is promoted by SWCNT-resonant light. AQE (red open circles) as a function of irradiation wavelength is compared to the optical absorption spectrum of the unfunctionalized (6,5)-SWCNTs (black line). AQE values were normalized to the highest value for simplicity and obtained from single experiments.

In addition, when irradiated with light that is completely out of resonance with the SWCNT, for example 400, 456, and 790 nm, the reaction is nearly as inefficient as the dark control, as is evident from the corresponding PL emission spectra shown in Figure 2-8. The small enhancement at nonresonate wavelengths may be due to the significant absorption background, which results from a minute amount of aggregates, amorphous carbon, or metallic species in the solution,[65] which is a result of the method used to isolate the (6,5)-SWCNTs. A cleaner SWCNT solution or a thin film of SWCNTs may provide a better sample for understanding the energy transfer mechanism in the optically-driven reaction. These observations confirm that while a

photothermal mechanism does occur, there is some degree of an electronic, or photochemical mechanism involved.

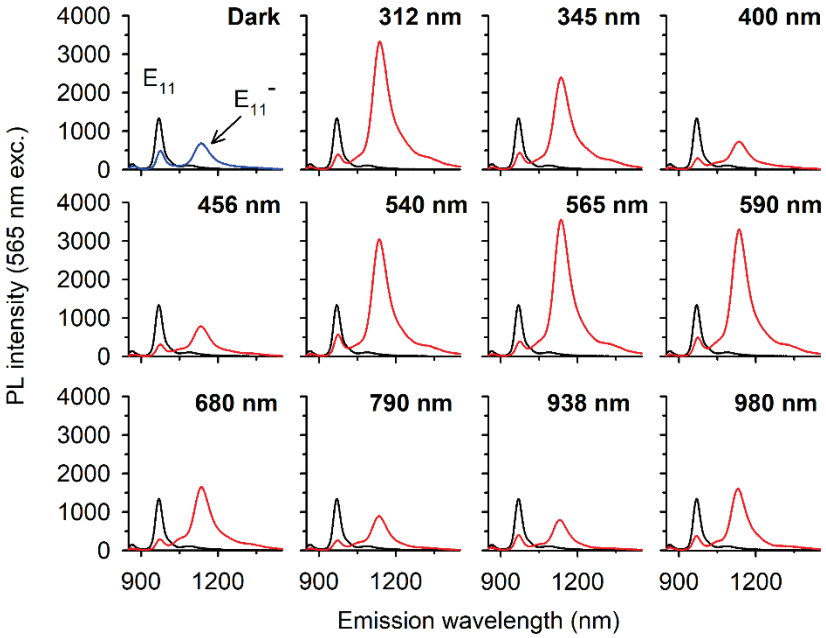

Figure 2-8. PL emission spectra (blue, red) of all samples used in wavelength dependence study. The condition of reaction (either dark or the wavelength or irradiation) is labeled on each plot. The emission spectrum of pristine (6,5)-SWCNT (black) is included in each figure for reference.

E_{11}-resonant light only minimally enhances the reaction efficiency versus the dark control, and it does so much less significantly than E_{22}- and E_{33}-resonant light. The ineffectiveness of the E_{11}-resonant light may be attributed to either (i) the very low output of our light source in this region (discussed later) or (ii) the inability for that energy to efficiently promote electrons to the conduction band to reduce the NO_2-BDT. The fluorescence lifetime of the first excited state (E_{11}) in (6,5)-SWCNT is 30 ps[66] or about 3000 times less than the fluorescence lifetime of small molecule polycyclic

aromatic hydrocarbons, such as pyrene and naphthalene.[67] Given this short lifetime, it is expected that the photochemical reactivity of SWCNT would be quite low.

An energy diagram containing the redox potentials of the reactants is presented in Figure 2-9. The redox potentials of both the nitroaryl radical (+0.05 V/SCE[68]) and the NO_2-BDT (+0.45 V/SCE[58]) are included for evaluation of the possibility of an electron transfer mechanism. Given the relatively low oxidation potential of the (6,5)-SWCNT valence band (VB; +0.541 V/SCE[69]), it is clear that the reactivity of semiconducting (6,5)-SWCNTs is poor towards diazonium. If photo-induced electron transfer were to occur, light would enhance the ability of the SWCNT to reduce the aryldiazonium cation to an aryl radical by raising its oxidation potential. We note that this mechanism is in contrast to the electrophilic addition of the aryl radical species onto SWCNTs,[58] which directly results in covalent bonding.

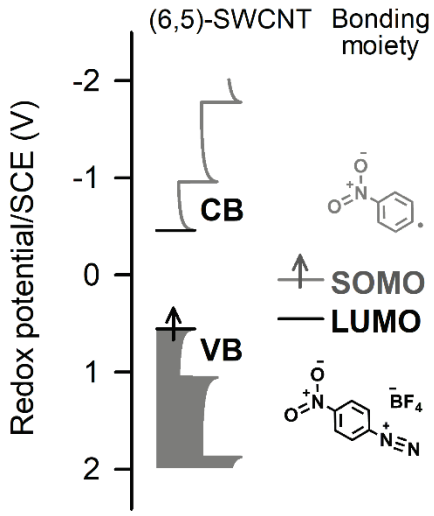

Figure 2-9. Energy level diagram of the (6,5)-SWCNT, NO_2-BDT, and nitroaryl radical. The diagram depicts the relative positions of the redox potentials of NO_2-BDT,[58] the nitroaryl radical,[68] as well as the valence (VB) and conduction (CB) bands of the (6,5)-SWCNT.[69]

2.3.3. A Kinetic Model for the Functionalization of Semiconducting SWCNTs by Aryldiazonium Salts.

As proposed by Usrey *et al*.,[64] the addition of aryl groups to SWCNTs by aryldiazonium salts, D, in our experiments could be described by a two-step mechanism. Usrey *et al*. modelled the functionalization of SWCNTs in this manner by a series of two first-order reactions, each with a distinct time constant. They reported that the functionalization of SWCNTs was characterized by a fast step, in which the aryldiazonium (or a long-lived intermediate thereof) noncovalently adsorbs to the SWCNT and partially dopes the surface, as evidenced by PL quenching. They found that a second, slower step occurs when the covalent bond is formed. They monitored the functionalization step via defect-induced Raman scattering. A similar two-step

mechanism was found to fit the optically- and thermally-driven reactions discussed in this work, despite the differences in systems. The differences include the type of SWCNTs used, which are chirality-enriched in our case, and that we use much lower concentrations of the aryldiazonium salt.

Eq. (2-2) outlines the first step in the reaction, the noncovalent physisorption (indicated by curved line) of the diazonium salt to the surface of the SWCNT.

$$\mathrm{SWCNT} + \mathrm{D} \overset{k_p}{\rightarrow} (\mathrm{SWCNT} \sim \mathrm{D}) \tag{2-2}$$

in which k_p is the rate constant for the physisorption of the diazonium to the SWCNT surface. This noncovalent interaction alters the electronic structure of the SWCNT and is spectroscopically observed by the rapid quenching of E_{11} PL.

The second step, covalent bonding (indicated by solid line) of the aryl group to the SWCNT, is described by eq. (2-3) when the low concentrations of by-products of the diazonium salts are ignored.

$$(\mathrm{SWCNT} \sim \mathrm{D}) \overset{k_c}{\rightarrow} (\mathrm{SWCNT} - \mathrm{D}) \tag{2-3}$$

in which k_c is the rate constant describing the covalent attachment of aryl groups. This step was monitored experimentally by following the evolution of the intensity of the defect PL.

The reaction outlined in eq. (2-3) proceeds via reduction of the aryldiazonium ion into an aryl radical, which may occur by either of two routes.[58] The first pathway occurs in the presence of a base of in neutral media (here, the aqueous solvent) to generate a diazonium anhydride (Figure 2-10a).[58] The anhydride readily forms in pH neutral media by reaction with the neutral solvent by the Gomberg–Bachmann reaction.[58] The diazoanhydride can decompose thermally by homolytic cleavage to

generate an aryl radical. The alternative pathway is single electron transfer from the SWCNT to the ion, which generates the radical (Figure 2-10b).[58] Given the neutral pH condition of our experiments, it is most likely that the aryl radical is formed via decomposition of the diazoanhydride in the experiments described in this work.

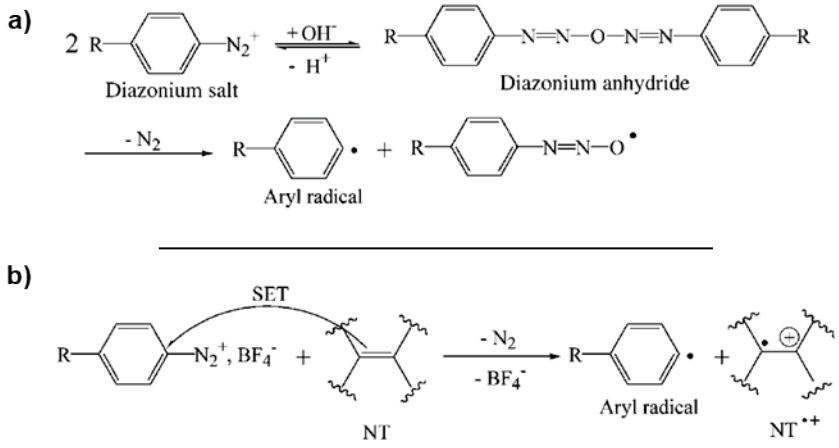

Figure 2-10. Routes for the generation of the reactive aryl radical from aryldiazonium salts. The aryl radical may be formed (a) indirectly via thermal decomposition of the diazonium anhydride or (b) directly via extraction of an electron from the SWCNT. SET stands for single electron transfer and NT stands for nanotube. Adapted and reprinted with permission from ref. 58.

A temperature- and irradiation power-dependent first order kinetic model was developed to describe the covalent modification of SWCNTs by aryldiazonium salts from eq. (2-4).

$$\frac{d[CNT-D]}{dt} = k_c[CNT - D] \quad (2\text{-}4)$$

The $[CNT - D]$ was measured by following the evolution of defect PL. By replacing $[CNT - D]$ with the intensity of defect PL, I_{11-}, eq. (2-5) is obtained.

$$\frac{d(I_{11-})}{dt} = k_c \times I_{11-} \quad (2\text{-}5)$$

in which t is time. By integrating eq. (2-5), eq. (2-6) is obtained.

$$I_{11-}(t) = I_{11-}(0) \times (1 - e^{-k_c t}) \quad (2\text{-}6)$$

It was observed that the reaction rate was highly dependent on temperature and the intensity of the light used to drive the reaction. In the absence of light, the covalent attachment of aryl groups to the SWCNT surface still occurred, but the defect PL is much less intense and took much longer to stabilize. This led us to adapt a kinetic model which accounts for the thermal and irradiation effects as outlined in eq. (2-7).

$$I_{11-}(t) = (A_{irrad} + A_{thermal})(1 - e^{-k_c t}) \quad (2\text{-}7)$$

in which A_{irrad} and $A_{thermal}$ are the unitless factors representing the irradiation and thermal contributions to the reaction. k_c is the rate constant describing the covalent bond formation. The irradiation factor considers 565 nm light only. The model may be expanded with further experimentation to account for different photon energies and the degree to which they resonate with the SWCNT chirality.

2.3.4. Application of the Kinetic Model to Power-Dependence Experiments.

Time-resolved PL spectroscopy studies reveal a two-step mechanism (Figure 2-11a-c). The noncovalent adsorption step is observed via the rapid quenching of the PL of the E_{11} state of the (6,5)-SWCNT. Within the first 0.25 h after the NO_2-BDT is added (at $t = 0$), no defect PL is detectable. The second covalent bonding step is observed via the slower exponential increase of the intensity of defect PL, which depends on the irradiation power density (and temperature, which will be addressed later). An increase in covalent functional degree, indicated by an increase in defect PL

intensity from E_{11}^{-}, is observed regardless of whether the solution is irradiated or protected from light. However, the defect PL is brighter and stabilizes faster with increasing power density.

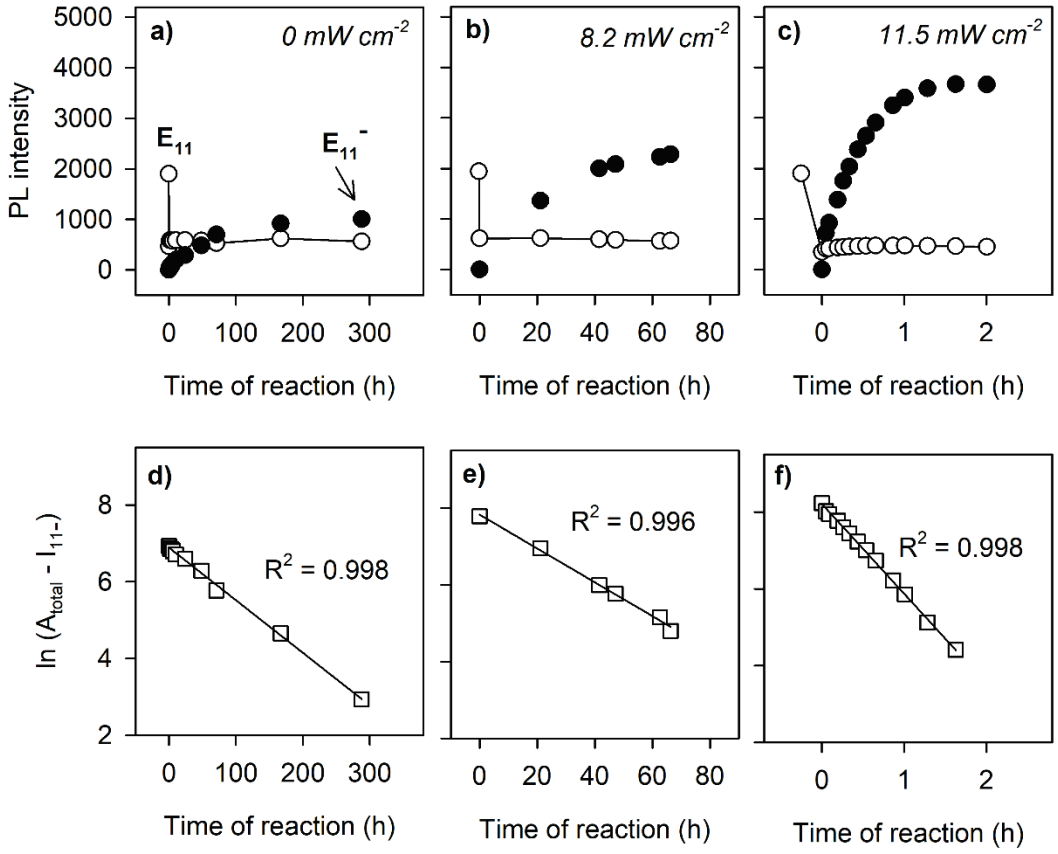

Figure 2-11. Kinetics of the functionalization of SWCNTs by aryldiazonium salts depends on irradiation power density. (a-c) Temporal evolutions of the E_{11} PL (open circles and black line to guide the eye) and E_{11}^{-} PL (filled circles) and (d-f) the E_{11}^{-} PL (open squares) fit using the pseudo first-order kinetic model. The coefficients of determination in (d-f) describe the quality of the linear regressions of the E_{11}^{-} data with the kinetic model applied (black line). The wavelengths of irradiation and excitation are 565 nm.

The data obtained from the power-dependence experiments was modelled using eq. (2-7). From this data, values for A_{irrad} and $A_{thermal}$ (at 21 °C) were calculated. Highly linear plots of $\ln(A_{total} - I_{11-})$ versus time were obtained (Figure 2-11d-f), in which A_{total} is the sum of the A_{irrad} and $A_{thermal}$. A plot of A_{total} versus the square of power density is highly linear (Figure 2-12).

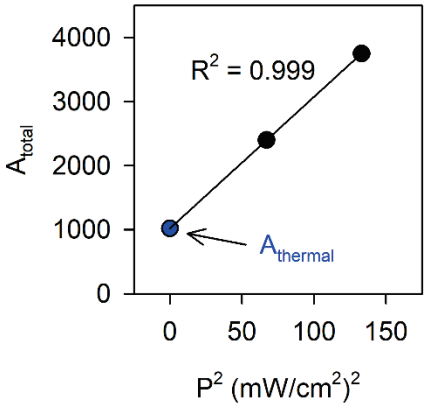

Figure 2-12. Determination of A_{irrad} and $A_{thermal}$ based on power dependence experiments at 21 °C. A_{total} is strongly correlated with the square of power density. $A_{thermal}$ is the data point where no irradiation is used (blue circle).

The $A_{thermal}$ at 21 °C was calculated using the dark control sample, in which $A_{irrad} = 0$, to be 1020. By subtracting this thermal contribution from the other power dependence data and plotting the resulting values of A_{irrad} (unitless) versus the square of the power density, eq. (2-8) was obtained.

$$A_{irrad} = (20.53 \pm 0.04)P^2 + (2 \pm 4) \quad (2\text{-}8)$$

in which P is irradiation power density of 565 nm light in units of mW cm^{-2}. Note that the value corresponding to the slope of the plot in Figure 2-11 has a unit of $(mW/cm^2)^{-}$

[2]. Table 2-1 summarizes the kinetic parameters obtained from the linear regressions of the experimental data with the kinetic model applied.

Table 2-1. Kinetic parameters obtained from power density experiments. Values were determined from the linear regressions of the data fit to the first-order model. All experiments were performed at 21 °C and 565 nm light was used. $t_{1/2}$ is the half-life and τ is the time constant.

Power density (mW cm^{-2})	**A_{irrad}**	**$A_{thermal}$**	**k_c (h^{-1})**	**$t_{1/2}$ (h)**	**τ (h)**	**R^2**
0	0	1021	0.014 ± 0.000	49.5 ± 0.0	71.4 ± 0.0	0.998
8.2	1380	1021	0.044 ± 0.001	15.8 ± 0.4	22.7 ± 0.5	0.999
11.5	2730	1021	2.34 ± 0.03	0.300 ± 0.004	0.4 ± 0.01	0.997

Notably, the A_{irrad} values are larger than that of $A_{thermal}$ at 21 °C, suggesting that even at relatively low power densities irradiation plays a significant role in the reaction. The reaction rate constants and completeness of the reaction differ substantially between samples irradiated and protected from light.

However, the rate constants do not scale linearly with the power density (Figure 2-12). We acknowledge that there is only a limited amount of data available from this study; however, it appears that there is a power density threshold above which the light has a more positive effect on the rate constant for covalent bonding. It is expected that by using a more intense radiation source, the efficiency and rate of reaction may be further improved. The completeness of the reaction, as measured by the final intensity of defect PL, appears to be more directly related to the power density than the rate constants (Figure 2-13). Defect PL is more than five-times brighter when irradiated at

the highest power density studied here than when protected from light, and it scales more linearly (R^2 = 0.96) with the power density than does k_c. Based on this relationship, it is possible that the poor efficiency of the reaction in the case of E_{11}-resonate irradiation (Figure 2-7) may be due to the low output of our light source in that range, which could lie below the power threshold for optically-driven functionalization.

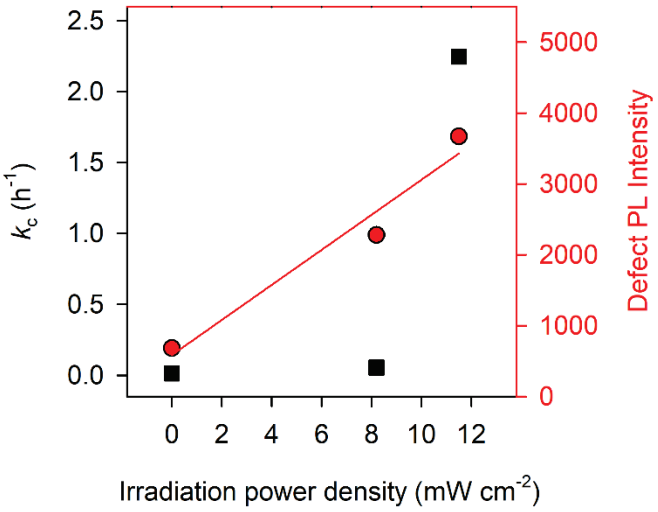

Figure 2-13. Reaction kinetics dependence of irradiation power density. The rate constant for covalent functionalization, k_c (black squares), has a positive relationship with irradiation power density. The final intensity of defect PL (red circles) has a linear relationship with power density (R^2 = 0.96). The frequency of the PL measurements was minimized in the case of the dark control, in order to give a more representative value for the thermally-controlled reaction.

2.3.5. The Kinetic Model Applied to Temperature-Dependence Experiments.

In the case of the temperature-dependent experiments, the temporal evolutions of E_{11}^- were normalized to their maximum (final) intensities because the PL was measured at the temperature of the reaction. Both I_{11} (the intensity of the E_{11} PL) and I_{11-} vary considerably with temperature in the case of SWCNTs. Furthermore, the ratio of these intensities, I_{11-}/I_{11}, varies with defect density.[50] Consequently, as the defect density evolves throughout the course of the reaction, any correction factor for the PL is constantly evolving as well. Further experimentation that results in quantification of this phenomenon may lead to more definitive results. However, by normalizing the defect PL to its final intensity in each case, the component of the temporal evolutions that addresses the relative rate constants and shapes of the evolutions is isolated. The completeness of the reaction, as measured by final intensity of defect PL, is not described by this model.

First, the thermal contribution to the reaction, $A_{thermal}$, was isolated by modelling the kinetics of the reaction at different temperatures in the absence of irradiation, where $A_{irrad} = 0$. The normalized temporal evolutions of defect PL were well-modelled by the pseudo first-order kinetic model (Figure 2-14a).

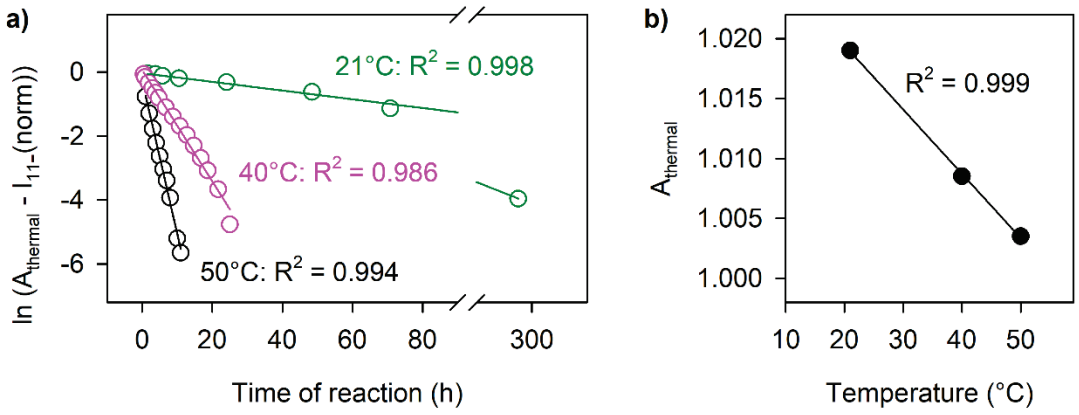

Figure 2-14. Determination of $A_{thermal}$ from normalized data. (a) Evolutions of normalized defect PL fit well with the kinetic model. (b) $A_{thermal}$ is negatively correlated with temperature. Linear regressions are indicated by solid lines.

A plot of the $A_{thermal}$ values versus temperature is linear (Figure 2-14b) and is modelled by eq. (2-9).

$$A_{thermal} = C_{thermal}\left((-5.37 \pm 0.13)T \times 10^{-4} + (1.030 \pm 0.001)\right) \quad (2\text{-}9)$$

in which T is the temperature of the solution in degrees Celsius. $C_{thermal}$ is the correction factor for PL intensity due to temperature. This equation predicts the shape of temporal evolutions of defect PL in the absence of light, accounting for the thermal contribution to the covalent functionalization of SWCNTs by aryldiazonium salts; however, it does not account for the differences in the final intensity of defect PL.

A_{irrad} was calculated by a similar treatment using the normalized data from power density experiments (Figure 2-15). Using the dark control, in which $A_{irrad} = 0$, $A_{thermal}$ at 21 °C was isolated. This value was subtracted from A_{total} for each power density to obtain A_{irrad} at each power density.

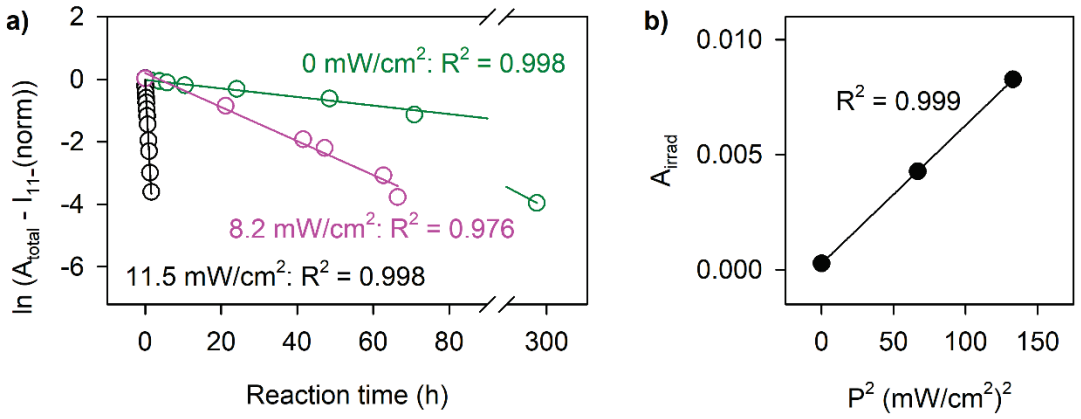

Figure 2-15. Determination of A_{irrad} from normalized data. (a) Evolutions of normalized defect PL fit well with the kinetic model. A_{total} is the sum of A_{irrad} and $A_{thermal}$. (b) A_{irrad} is positively correlated with the square of power density.

A_{irrad} is linearly correlated with the square of power density. The linear regression of A_{irrad} with the square of power density is given by eq. (2-10).

$$A_{irrad} = C_{irrad}\left((6.02 \pm 0.02)P^2 \times 10^{-5} + (2.7 \pm 0.1) \times 10^{-4}\right) \quad (2\text{-}10)$$

in which P is the irradiation power of 565 nm light in units of mW cm^{-2}. The correction factor C_{irrad} accounts for the intensity difference in defect PL. Notably, A_{irrad} is positively correlated with power density, while $A_{thermal}$ is negatively correlated with temperature.

2.3.6. Arrhenius Behavior in the Presence and Absence of Light.

In order to better evaluate the role of the irradiation, specifically the degree to which it (i) induces photothermal decomposition of the long-lived intermediate or (ii) drives electron transfer from the SWCNT to the adsorbate, we studied the Arrhenius behavior of the reaction. The model described by eqs. (2-8), (2-9), and (2-10) was

applied to temporal evolutions of defect PL (which were not normalized) in both the absence and presence of the SWCNT-resonate irradiation (565 nm).

The thermally-controlled reaction was monitored spectroscopically in the absence of irradiation at 21, 40, and 50 °C (Figure 2-16). The first order kinetic model represents the data well as evidenced by the linear relationships seen in Figure 2-16.

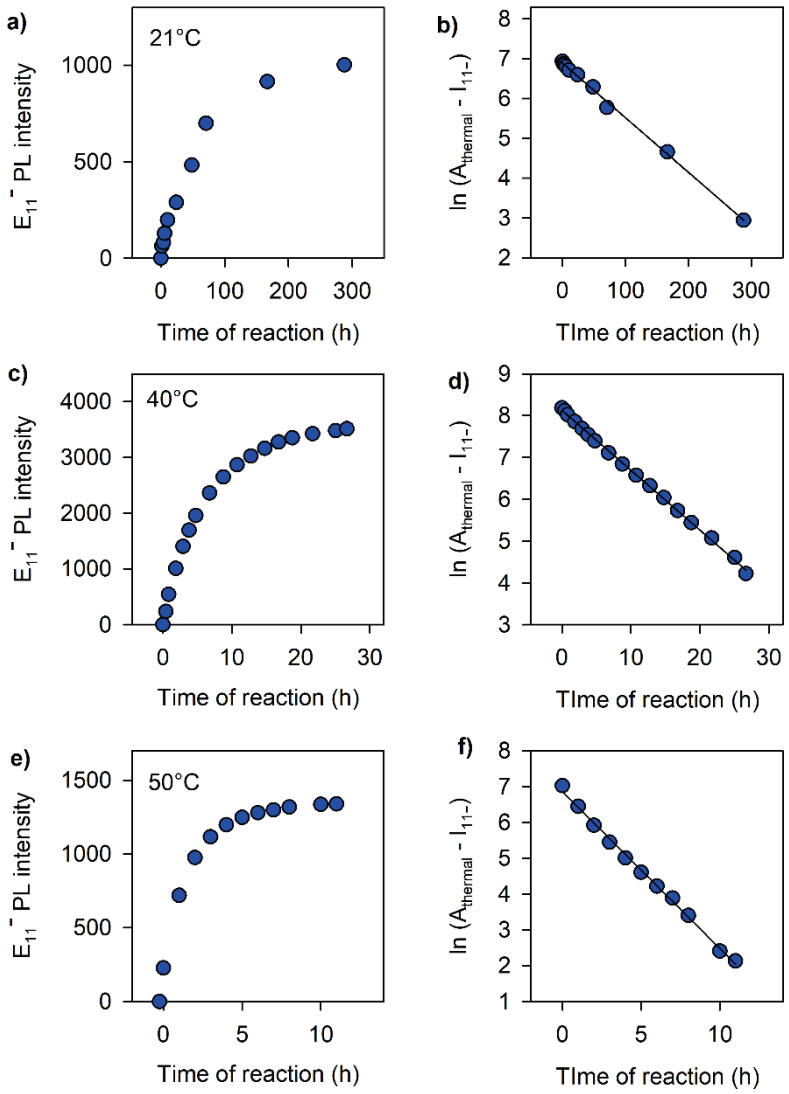

Figure 2-16. The thermally-controlled reaction data applied to the proposed order kinetic model. (a, c, e) Temporal evolutions of defect PL (b, d, f) fit well when modelled by the first-order model (linear regressions are shown by solid lines).

The optically-induced reaction was monitored spectroscopically at 21, 30, 40, and 50 °C (Figure 2-17). Throughout the range of temperatures tested, the defect PL stabilizes faster when irradiated than when protected from light.

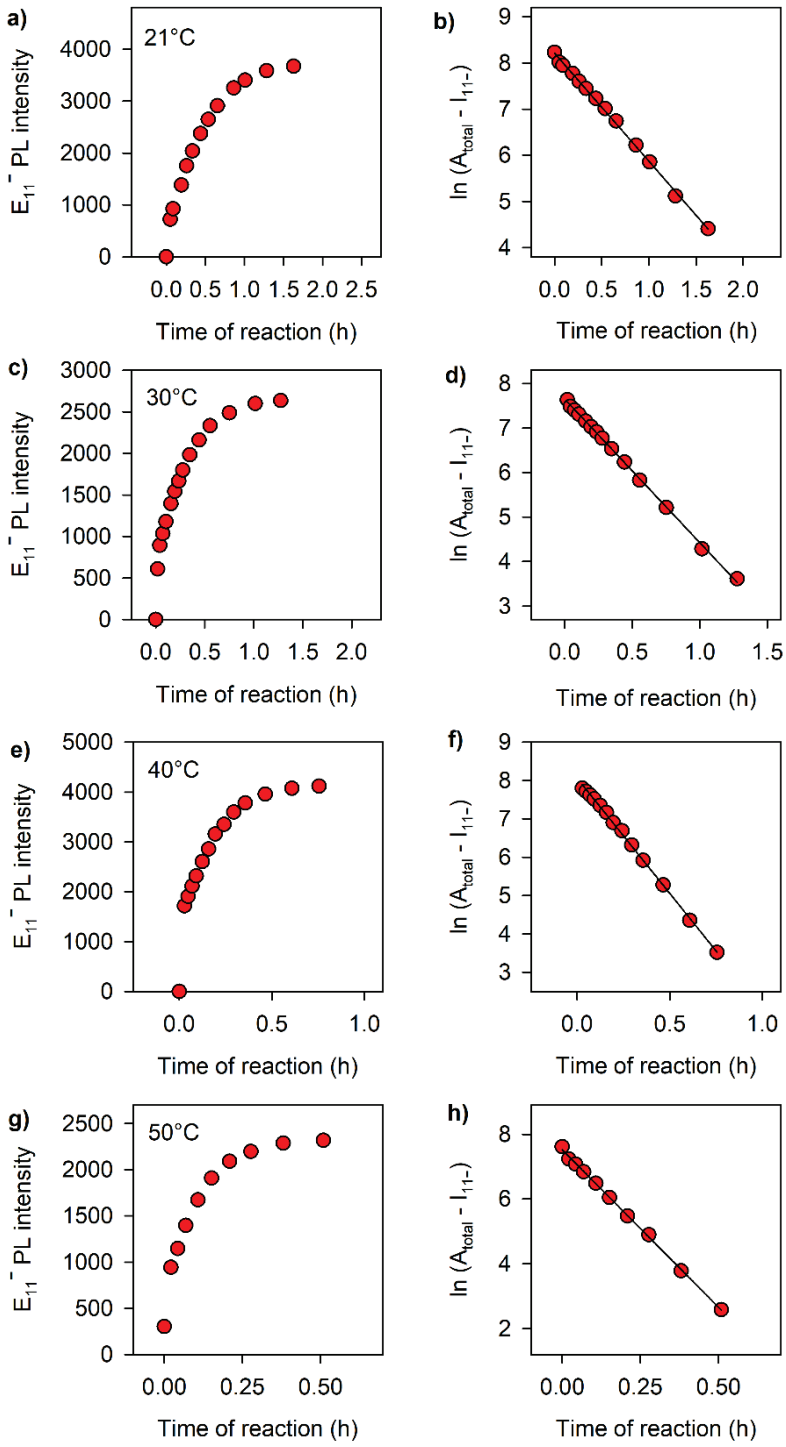

Figure 2-17. The optically-driven reaction data applied to the proposed kinetic model. (a, c, e, g) Temporal evolutions of the intensity of defect PL (b, d, f) fit well when modelled by the first-order model (linear regressions are shown by solid lines).

The kinetic parameters obtained from fitting the PL data from dark control experiments to the first order kinetic model are tabulated in Table 2-2 and reveal that the model represents the data well ($R^2 > 0.99$).

Table 2-2. Kinetic parameters for the thermally-driven reaction obtained by fitting to the proposed model.

T (°C)	$A_{thermal}$	$C_{thermal}$	k_c (h^{-1})	$t_{1/2}$ (h)	τ (h)	R^2
21	1020	1001	0.014 ± 0.000	49.50 ± 0	71.43 ± 0	0.998
40	3850	3817	0.143 ± 0.005	4.8 ± 0.2	7.0 ± 0.2	0.999
50	1343	1339	0.437 ± 0.008	1.59 ± 0.03	2.29 ± 0.04	0.997

The kinetic parameters obtained from fitting the irradiated temperature-dependent PL data to the pseudo-first order model are tabulated in Table 2-3. Because of the temperature-dependent PL effect, the values for A_{irrad} and $A_{thermal}$ could not be isolated from each other as explained earlier. Despite this, the reaction rate constants were extracted for analysis of the Arrhenius behavior.

Table 2-3. Kinetic parameters for the optically-driven reaction obtained by fitting to the proposed model.

T (°C)	$A_{thermal} + A_{irrad}$	k_c (h^{-1})	$t_{1/2}$ (h)	τ (h)	R^2
21	3750	2.34 ± 0.03	0.296 ± 0.004	0.427 ± 0.005	0.998
30	2670	3.23 ± 0.03	0.215 ± 0.002	0.310 ± 0.003	0.999
40	4150	6.00 ± 0.06	0.116 ± 0.001	0.167 ± 0.002	0.999
50	2330	9.7 ± 0.1	0.071 ± 0.001	0.103 ± 0.001	0.999

The Arrhenius equation was applied to derive the apparent activation energies, E_a, for the thermally-driven (dark control) and optically-driven (irradiated) reactions by eq. (2-11).

$$\ln k_c = \ln A - \frac{E_a}{RT} \tag{2-11}$$

in which A is the pre-exponential factor, R is the gas constant (8.314 J K^{-1} mol^{-1}), and T is temperature. Linear regressions of the data reveal that the reaction displays Arrhenius behavior both in the presence and absence of irradiation (Figure 2-18). In fact, the removal of the data point at 30 °C from the irradiated data results in an R^2 of 1.00 for the irradiated reaction.

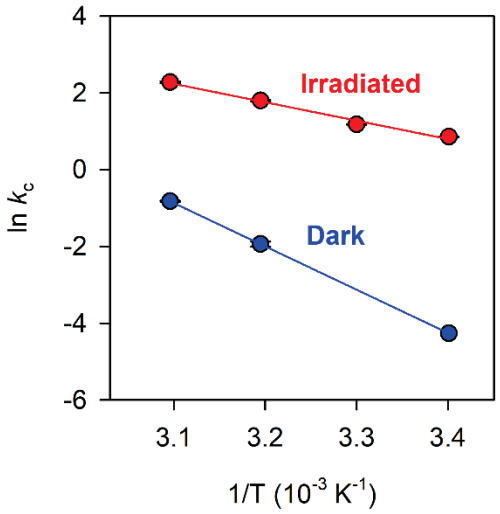

Figure 2-18. Arrhenius plot for the optically- and thermally-driven reactions. While both reactions exhibit Arrhenius behavior, a significant decrease, ~54 kJ mol^{-1}, in the apparent E_a upon irradiation is observed for the optically-driven reaction. Error bars reflect the uncertainty in calculation of k_c.

Furthermore, irradiation significantly reduces the apparent E_a by 57%, from (93.8 ± 0.1) kJ mol^{-1} to (39.9 ± 3.1) kJ mol^{-1} (Table 2-4). In the case of a typical photochemically-driven reaction, light provides the activation energy. However, the significant reduction of the apparent activation energy observed here, ~54 kJ mol^{-1} (0.56 eV), does not correspond to the energy of the irradiation used to drive the reaction, 565 nm (2.19 eV). This mismatch may reflect the presence of two competing mechanisms, electronic and photothermal, as well as the inefficient photochemical activity of SWCNTs discussed earlier.

Table 2-4. Arrhenius behavior of optically- and thermally-driven reactions. *A* is the pre-exponential factor.

Condition	**E_a, apparent (kJ mol^{-1})**	***A* (h^{-1})**	**R^2**
Irradiated	39.9 ± 3.1	(2.7 ± 0.2) x 10^7	0.988
Dark	93.8 ± 0.1	(6.23 ± 0.01) x 10^{14}	1.000

2.4. Conclusions

In summary, it was demonstrated that functionalization of semiconducting SWCNTs using aryldiazonium salts can be significantly accelerated through optical excitation of the carbon nanotubes. This light-driven reaction leads to over 5-times more efficient functionalization, as indicated by the defect PL brightness. The chemistry's wavelength dependence suggests that the reaction mechanism has both photothermal and electronic components. The optical and thermal components were accounted for in a first-order kinetic model which fit the experimental data well, despite limitations from the temperature-dependent effects of SWCNT PL. Temperature-

dependent studies revealed that both the optically- and thermally-driven reactions have Arrhenius behavior. A 57% reduction of the apparent E_a in the presence of SWCNT-resonate light is attributed to both electronic and photothermal mechanisms. The use of a molecule with a higher barrier to reactivity with SWCNTs may result in better resolution, especially the light-dark resolution. Further studies, including those of *in situ* single nanotube reactions may provide more insight about the competing mechanisms. Ultimately, this optically-driven functionalization method may allow for chemical targeting of a specific chirality within a SWCNT mixture, a long sought after goal,[56] and optical lithography of low dimensional carbon materials.

Chapter 3: Chirality-Selective Functionalization of Semiconducting Carbon Nanotubes with a Reactivity-Switchable Molecule

Adapted from: L. R. Powell, M. Kim, and Y. Wang. Journal of the American Chemical Society, 2017, 139, 12533-12540.

L.R.P designed and performed experiments. M.K. performed molecular modelling calculations. L.R.P. and Y.W. wrote the manuscript with input from all authors.

3.1 Introduction

Single-walled carbon nanotubes (SWCNTs) are molecular cylinders of sp^2 carbon that can take the form of many different structures known as chiralities.[70] In a typical synthetic mixture, approximately two-thirds of the chiralities are semiconductors and the remainder is made up of metals. Chirality-selective chemistry has long been sought after as the key to sorting by chirality,[56] on-chip passivation,[71] and nanotube lithography.[56] For semiconducting SWCNT-based optoelectronic and biomedical devices, even the presence of a few metallic SWCNTs can dramatically hinder their performance.[72-73] Chirality selective chemistry may provide a chemical route to selectively block conductive channels in nanotube arrays directly on-chip.[71] The selective chemistry would also add a new layer of chemical functionality to SWCNTs for improving resolution between difficult-to-separate SWCNT chiralities.[62, 74-76]

Strano *et al*.[56] first reported that metallic SWCNTs can react with aryldiazonium salts to near exclusion of the semiconducting chiralities. This selectivity

for metallics arises from the abundant available electron density of metallic SWCNTs as opposed to the semiconductors. The metal-semiconductor selectivity can be improved by tuning the relative redox potential of the bonding moiety against that of the SWCNT,[77] or by tuning the reaction conditions.[78-79] For example, the addition of electron-donating groups to the aryldiazonium bonding moiety lowers the electron affinity of the diazonium salts, suppressing their reaction with semiconducting SWCNTs and consequently improves type selectivity.[58] Recently, Darchy *et al.*[77] achieved a record 50-fold improvement in metal-semiconductor selectivity by using a diazoether compound, which has a significantly higher oxidation potential than aryldiazonium salts. These advances highlight the significant efforts in developing selective covalent chemistry for SWCNTs; however, the selectivity has generally been limited to metals *vs*. semiconductors. Achieving chemical selectivity at the chirality level has remained a significant challenge. Among semiconductors, smaller diameter chiralities with larger bandgaps are more reactive toward aryldiazonium salts.[56, 80-81]

Although extensive covalent functionalization can significantly disrupt the optical[38] and transport characteristics of SWCNTs, controlled chemical modification of SWCNTs can be minimally disruptive to transport properties[54] and impart new functionality by creating molecularly tunable fluorescent quantum defects.[9, 43] These chemically implanted quantum defects trap mobile excitons, allowing them to relax radiatively via a new emission state, E_{11}^{-}, significantly brightening the near-infrared (NIR) photoluminescence (PL) of SWCNTs.[9] The defect PL originating from this state is highly tunable, in both intensity and energy, by varying the chemical nature of the defect group.[9, 43] This allows the defect PL to be used as a sensitive quantitative

indicator of functional degree that can be used to monitor the surface chemistry of SWCNTs *in situ*.[63]

Herein, we show that it is possible to isolate covalent bonding within a mixture of chiralities to that of a chirality which is otherwise less reactive, achieving unprecedented chiral selectivity. We overcome the inherent trends in SWCNT reactivity by using a stereoisomer of a diazoether compound and directing the reaction to the target SWCNT in two ways. First, we control the thermodynamic barrier to isomerization (conventionally defined as the isomerization energy) of an inactive diastereoisomer to its reactive conformation by tuning the pH of the environment. Second, we select the target SWCNT chirality for functionalization by exciting the nanostructure at one of its van Hove transitions.[63, 82] As an illustration of this concept, we synthesized a diazoether isomer, (*E*)-3-*O*-*p*-nitrobenzenediazoascorbic acid (*p*-NO_2-DZE), and tuned its thermodynamic barrier isomerization to its reactive conformation (Figure 3-1). Ultimately, we show that this diazoether chemistry can be used in conjunction with our optical selection technique to isolate chemistry to a single SWCNT chirality within a mixture of semiconducting species. Particularly, we demonstrated preferential functionalization of (7,3)-SWCNT over the more reactive (6,5)-SWCNT. This on-demand reactivity switching is exploited to achieve chirality-selective functionalization within a mixture of structurally similar semiconducting SWCNTs.

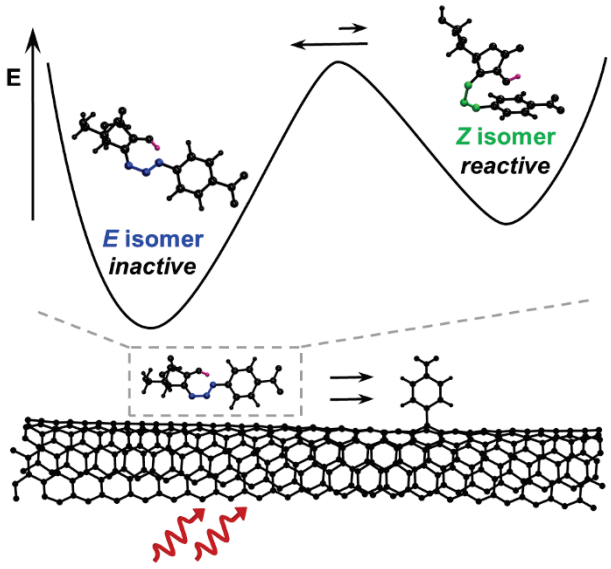

Figure 3-1. On-demand switching of diazoether reactivity toward a SWCNT generates a covalently bonded aryl functional group. Localized isomerization of the inert *E*-isomer of 3-*O*-*p*-nitrobenzenediazoascorbic acid to the reactive *Z*-isomer is achieved by tuning of the thermodynamic barrier to isomerization with pH and is driven by resonant optical excitation of the SWCNT substrate. Isomerization, from *E* to *Z*, results in covalent attachment of a nitrobenzene functional group to the sp^2-hybridized carbon lattice, creating a fluorescent quantum defect that fluoresces in the NIR.

3.2 Experimental Methods

3.2.1. Preparation of Chirality-Enriched SWCNT Suspensions.

(6,5)-SWCNT enriched samples were separated from HiPco materials (batch no. 194.3, Rice University) by gel chromatography[62] using a Sephacryl S-200 HR column (GE Healthcare). The sorted SWCNTs were individually suspended by 1% wt./v sodium dodecyl sulfate (SDS, Sigma-Aldrich, 99%) in 99.8% deuterium oxide (D_2O, Cambridge Isotopes, Inc.). The absorbance of the (6,5)-SWCNT solution was

adjusted to 0.12 (1 cm optical path length) at E_{11}, corresponding to a carbon concentration of approximately 0.66 mg L^{-1}.

(7,3)-SWCNT enriched samples were isolated from CoMoCAT SWCNTs (SG65i, lot no. SG65i-L39, Southwest Nanotechnologies, Inc.) by aqueous two-phase extraction[75] using single-stranded DNA oligomers with sequence $TCT(CTC)_2TCT$ (purified by standard desalting, Integrated DNA Technologies). After extraction of the (7,3)-SWCNT, the DNA was precipitated by the addition of sodium thiocyanate (98%, Sigma Aldrich) and then removed after purification. The remaining SWCNTs were suspended in 1% wt./v SDS in D_2O.

3.2.2. pH-Dependent Activation Energies for *Z*-to-*E* Isomerization of 3-*O*-*p*-nitrobenzenediazoascorbic acid.

Temperature and pH-dependent UV-visible absorption spectroscopy permits observation of isomerization for calculation of the activation energy for isomerization of the diazoether compound. Darchy *et al.*[77] described the synthesis of diazoether isomers as a two-step series reaction as shown in eq. (3-1).

$$Dz + Asc \overset{k_f}{\rightarrow} Z \overset{k_i}{\rightarrow} E \tag{3-1}$$

in which Dz is the aryldiazonium salt, Asc is the ascorbate, Z is the *Z*-isomer, and E is the *E*-isomer. The rate constant for formation of the *Z*-isomer of the diazoether is described by k_f, and k_i is the rate constant for isomerization from the *Z*-isomer to the thermodynamically stable *E*-isomer. By integrating the expression given by eq. (3-1) in the main text and rearranging, the expression given by eq. (3-2) is obtained, which

relates the disappearance of the *Z*-isomer to the rate of isomerization over time for a given set of conditions (temperature, pH).

$$ln[Z]_t = ln[Z]_0 - k_i t \quad (3\text{-}2)$$

in which $[Z]_0$ and $[Z]_t$ are the concentrations of the *Z*-isomer at times 0 and t, respectively. The isomerization study was completed within the limits of Beer's Law (where absorbance < 1.0), so that absorbance (A) was used to calculate $[Z]$. To account for the spectral overlap of the two isomers, we calculated a correction factor. We assumed that (i) *Z*-to-*E* isomerization is complete (100% of *Z* isomerizes to *E*) and (ii) only *Z*-isomers exist at t = 60 s and only *E*-isomers exist at t = 2500 s. The wavelengths of maximum absorbance of the *Z*- and *E*-isomers are 290 nm and 356 nm, respectively. Application of Beer's law and assumption (i) corresponds to the relation given by eq. (3-3).

$$\frac{A_i(290)}{\varepsilon_{290}(Z)l} = \frac{A_f(356)}{\varepsilon_{356}(E)l} \quad (3\text{-}3)$$

in which $A_i(290)$ is the initial absorbance (at 60 s) measured at 290 nm, and $A_f(356)$ is the final absorbance (at 2500 s) measured at 356 nm. $\varepsilon_{290}(Z)$ and $\varepsilon_{356}(E)$ are the molar absorptivities of the *Z*- and *E*-isomers corresponding to their wavelengths of maximum absorbance, 290 nm and 356 nm, respectively. l is the optical path length. From application of assumption (ii), expressions given by eq. (3-4) and eq. (3-5) were obtained which describe the concentrations of the *Z*- and *E*-isomers, $[Z]_i$ and $[E]_f$, at t = 60 s and t = 2500 s, respectively.

$$[Z]_i = \frac{A_i(290)}{\varepsilon_{290}(Z)l} = \frac{A_i(356)}{\varepsilon_{356}(Z)l} \quad (3\text{-}4)$$

$$[E]_f = \frac{A_f(290)}{\varepsilon_{356}(E)l} = \frac{A_f(356)}{\varepsilon_{290}(E)l} \quad (3\text{-}5)$$

in which $A_i(290)$ is the initial absorbance (at 60 s) measured at 290 nm, and $A_f(356)$ is the final absorbance (at 2500 s) measured at 356 nm. $\varepsilon_{356}(Z)$ and $\varepsilon_{290}(E)$ are the molar absorptivities of the *Z*- and *E*-isomers corresponding to their nonresonate wavelengths, 356 nm and 290 nm, respectively. Solving the system of equations, including eq. (3-3), (3-4), and (3-5), results in an expression that describes the disappearance of the *Z*-isomer with time by a first-order kinetic model.

In order to observe the isomerization kinetics by UV-visible absorption spectroscopy, 50 μM aqueous solutions of 3-*O*-*p*-nitrobenzenediazoascorbic acid were prepared in dilute aqueous solutions of phosphoric acid (H_3PO_4, 85%, JT Baker) or sodium hydroxide (NaOH, 99.99%, Sigma Aldrich) using equimolar amounts of the reactants (aryldiazonium salt and ascorbic acid) as outlined previously. Absorption measurements were taken at various time intervals (Figure 3-2) with stirring using a Perkin Elmer Lambda 35 UV-vis spectrophotometer equipped with a photomultiplier tube detector in a quartz cuvette (1 cm optical path length). The temperature of the solution was controlled and monitored with a Peltier system (Perkin Elmer PTP-6).

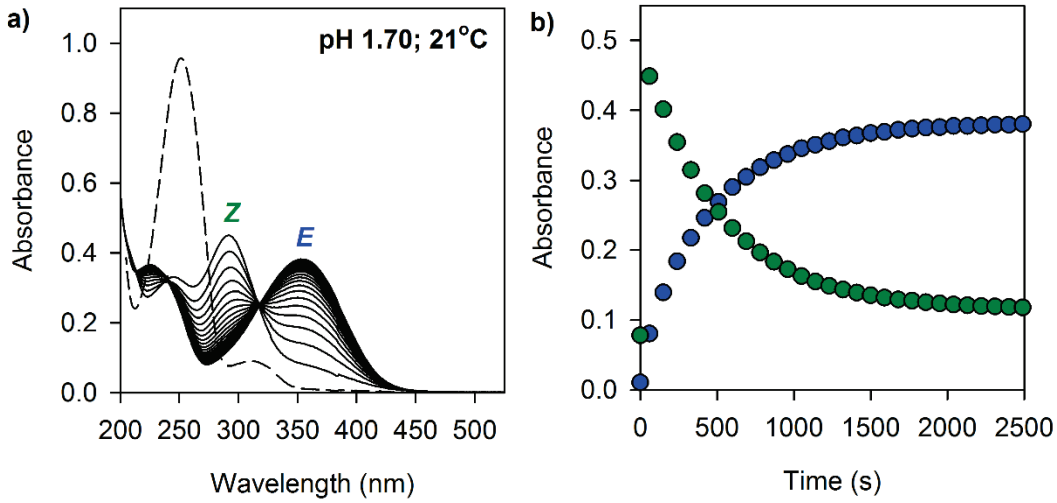

Figure 3-2. Real-time monitoring of the isomerization of diazoether by UV-visible absorption spectroscopy. (a) Absorption spectra (1 cm path length) of a 50 μM solution of diazoether (solid lines) in aqueous phosphoric acid at 21 °C and pH 1.70. The sum of the absorption spectra corresponding to the reactants in shown for comparison (dashed line). (b) Absorbance at 290 nm (*Z*-isomer, green) and 356 nm (*E*-isomer, blue) is monitored versus time.

3.2.3. Synthesis of *Z*- and *E*-Isomers of 3-*O*-*p*-nitrobenzenediazoascorbic acid in Aqueous Media for Reaction with SWCNTs.

Because the *Z*-diazoether is a kinetic product of the *O*-coupling, it is only generated during the coupling of the diazonium salt and ascorbic acid and quickly isomerizes to the *E*-isomer. In order to synthesize this *Z*-isomer, we followed the an amended version of the *in situ* method proposed by Darchy *et al*.[77] in aqueous solution. To a 50 μM aqueous (pH adjusted with H_3PO_4 or NaOH) solution of L-ascorbic acid, an equimolar amount of *p*-nitrobenzenediazonium tetrafluoroborate (synthesized) was added with stirring. For reaction with SWCNTs, the solution was either immediately used (for *Z*-isomer) or incubated for 1 h at room temperature to insure complete

isomerization to the *E*-isomer). The diazoether isomer prepared in this manner were used for the experiment including the *Z*-isomer only. In the case of this experiment, a small aliquot of the aqueous isomer solution was added to 1 mL of (6,5)-SWCNTs ([*p*-NO_2-DZE] : [SWCNT carbon] = 1:550) in a small glass vial (covered in aluminum foil) and protected from light. The solution was stirred for 5 h and then the contents were transferred to a quartz cuvette for PL measurements

3.2.4. Synthesis of 3-*O*-*p*-nitrobenzenediazoascorbic acid.

3-*O*-*p*-nitrobenzenediazoascorbic acid was isolated using a modified procedure from Doyle *et al*.[83] First, *p*-nitrobenzenediazonium tetrafluoroborate was synthesized as previously described[63] from *p*-nitroaniline (99%, Sigma Aldrich) and nitrous acid (48 wt.% tetrafluoroboric acid solution in water, Sigma Aldrich; sodium nitrite, 97%, Sigma Aldrich). 1.17 g (5.00 mmol) of *p*-nitrobenzenediazonium tetrafluoroborate was dissolved in 25 mL of degassed acetonitrile (99.9%, Acros Organics) and then diluted with 15 mL of Nanopure^{TM} water (Barnstead NANOpure DIamond Life Science UV/UF ultrapure water system, Thermo Scientific, Model D11931). 0.881 g (5.00 mmol) of L-ascorbic acid (99%, Sigma Aldrich) was added to the diazonium solution which immediately turned a darker yellow color. The solution was bubbled with argon at room temperature for 30 min. This aqueous solution was extracted with two 20 mL aliquots of diethyl ether (anhydrous, BHT stabilized, Fisher Scientific). The ether solutions were dried over magnesium sulfate (anhydrous, 99%, JT Baker) until the solution was clear, and the solvent was removed at reduced pressure. A yellow solid precipitated and it was washed with dichloromethane (99.5%, Sigma Aldrich) by vacuum filtration. This crude product was recrystallized from 2-butanone (99%, Sigma

Aldrich) with dichloromethane at room temperature which yielded a pale yellow solid. Samples were stored under argon at 0 °C. The structure was confirmed by ^{1}H-nuclear magnetic resonance spectroscopy (^{1}H-NMR; Figure 3-3 and Table 3-1).

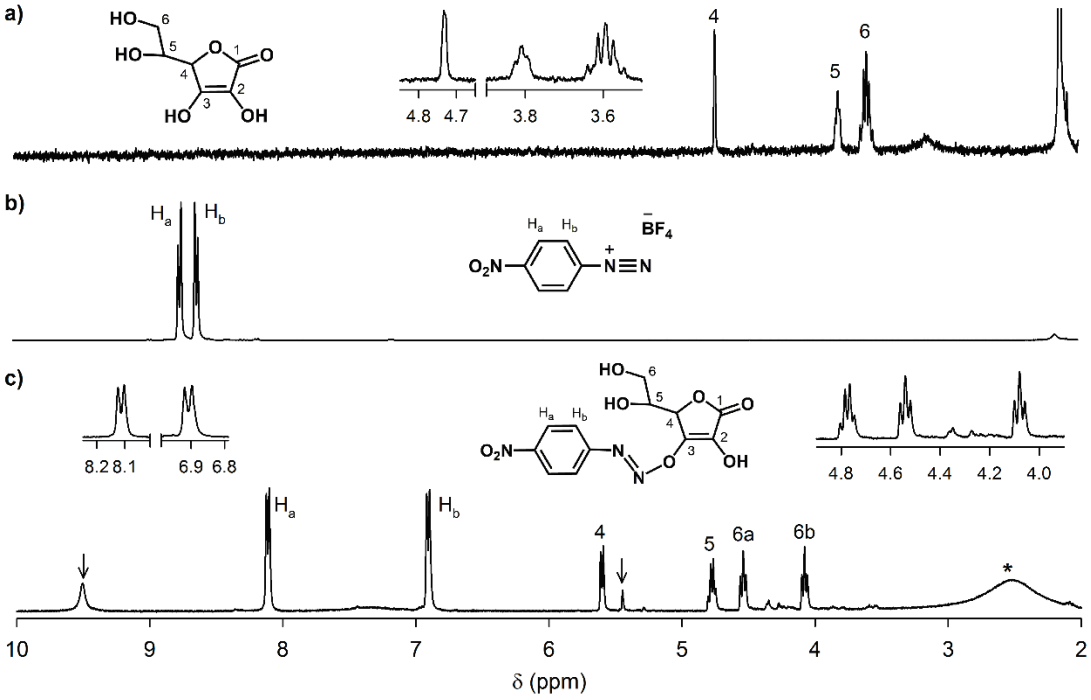

Figure 3-3. ^{1}H-NMR (400 MHz) spectra of reactants and isolated diazoether. ^{1}H-NMR spectra of (a) L-ascorbic acid (Sigma Aldrich, low solubility), (b) *p*-nitrobenzenediazonium tetrafluoroborate (synthesized), and (c) 3-*O*-*p*-nitrobenzenediazoascorbic acid (synthesized) in acetonitrile-d_3. Singlet peaks at 9.7 ppm and 7.5 ppm disappear with the addition of D_2O, suggesting that they result from coupling to the alcohol groups of ascorbic acid. The peak denoted by an asterisk indicates that there is a small amount of water in the isolated solid.

The *E*-diazoether compound synthesized by this method was used for all experiments shown reported in this work which make use of the *E*-isomer. For experiments involving the Z-isomer (the kinetic product), the method outlined in secton

3.2.3. was used. The diazoether was prepared for NMR by dissolving ~1 mg of a solid in 0.5 mL of acetonitrile-D3 (99.8%, Cambridge Isotope Laboratories) in a 5 mm diameter NMR tube (NORELL, 507HP). The analysis was performed on a Bruker DRX-400 high resolution spectrometer. The spectrum was analyzed and coupling constants were calculated with MestReNova software (v9).

Table 3-1. ^{1}H-NMR (400 MHz) peak assignments for isolated 3-*O*-*p*-nitrobezenediazoascorbic acid. Chemical shifts, splitting patterns, coupling constants, and peak integration values are reported for the diazoether in acetonitrile-D3. Proton assignments correspond to those labelled in Figure 3-3.

Proton assignment	**Chemical shift, δ (ppm)**	**Multiplicity**	***J* (Hz)**	**Integration**
H6a	4.08	dd	8.5	1H
H6b	4.54	dd	8.3	1H
H5	4.78	q	7.9	1H
H4	5.60	d	7.7	1H
aryl-H_b	6.91	d	9.0	2H
aryl-H_a	8.11	d	9.0	2H

3.2.5. Optically-Activated Functionalization of SWCNTs with 3-*O*-*p*-nitrobenzenediazoascorbic acid.

An aliquot of 50 μM 3-*O*-*p*-nitrobenzenediazoascorbic acid in D_2O was added to a suspension of chirality-enriched SWCNT in a 1 cm quartz cuvette, which was stirred and protected from light at 21 °C ([*p*-NO_2-DZE] : [SWCNT carbon] = 1:550). The temperature of the solution was maintained throughout the experiment using a

circulating water bath (FL-1027, Horiba Jobin Yvon and Fisher Scientific Isotemp 3016D). The addition of the ascorbate diazoether solution amounted to less than a 0.3% increase in volume, which avoided significantly changing the SWCNT concentration. Any pH adjustment was completed before addition of the diazoether by the addition of aliquots of 50 μM H_3PO_4 or 50 μM NaOH in D_2O. [H^+] was monitored with a pH meter (Accumet AB15 pH/mV/temperature meter) and corresponding electrode (Accumet gel-filled pencil-thin pH electrode) which was calibrated against buffer solutions. The capped solution was stirred for 20 min with protection from light before being continuously irradiated with the monochromator-selected (10 nm bandpass; 565 nm or 505 nm as noted in the text) light from a 450 W Xenon arc lamp (Ushio) for 5 h. The power density was measured with an optical power meter (Newport 1916-C) and silicon detector (Newport 918-SL-OD3). The reactions were protected from ambient light throughout the extent of the experiment and the reaction was evaluated spectroscopically by defect PL.

3.2.6. Thermal Effects on Functionalization of SWCNTs with 3-*O*-*p*-nitrobenzenediazoascorbic acid.

The pH of a suspension of (6,5)-SWCNTs was adjusted by the addition of aliquots of 50 μM NaOH or 50 μM H_3PO_4 and measured with a pH meter and electrode (Accumet pH/ATC electrode). Next, a circulating water bath was used to control the temperature of the solution within a capped 1 cm quartz cuvette throughout the reaction (either 21 °C or 70 °C). The solution temperature was measured with a LabQuest 2 module and temperature sensor (Vernier). Then, an aliquot of 50 μM 3-*O*-*p*-nitrobenzenediazoascorbic acid in D_2O was added to the SWCNT suspension ([*p*-NO_2-

DZE] : [SWCNT carbon] = 1:550) with stirring and protection from light. After 5 h, the reaction was characterized spectroscopically (pH adjusted back to 7.5 and the solution was cooled to 21°C).

3.2.7. Spectroscopic Characterization of Covalent Functionalization.

Fluorescence spectra and excitation-emission maps were collected on a HORIBA Jobin Yvon Nanolog Spectrofluorometer equipped with a 450 W Xenon arc lamp and a calibrated multichannel InGaAs array detector in a 1 cm quartz bi-mirrored cuvette. Care was taken to avoid pH-dependent effects on PL by taking all reported PL measurements at neutral pH (~7.5) by adjusting the pH of solutions with small volumes of 50 μM NaOH or H_3PO_4 solutions in D_2O (Figure 3-4). Measurements were taken after 5 h of reaction. The reported PL intensities are peak intensities (not integrated areas) unless otherwise noted. UV-vis-NIR absorption spectra were measured in the same way using a PerkinElmer Lambda 1050 UV-vis-NIR spectrophotometer equipped with a photomultiplier tube and a broadband InGaAs detector.

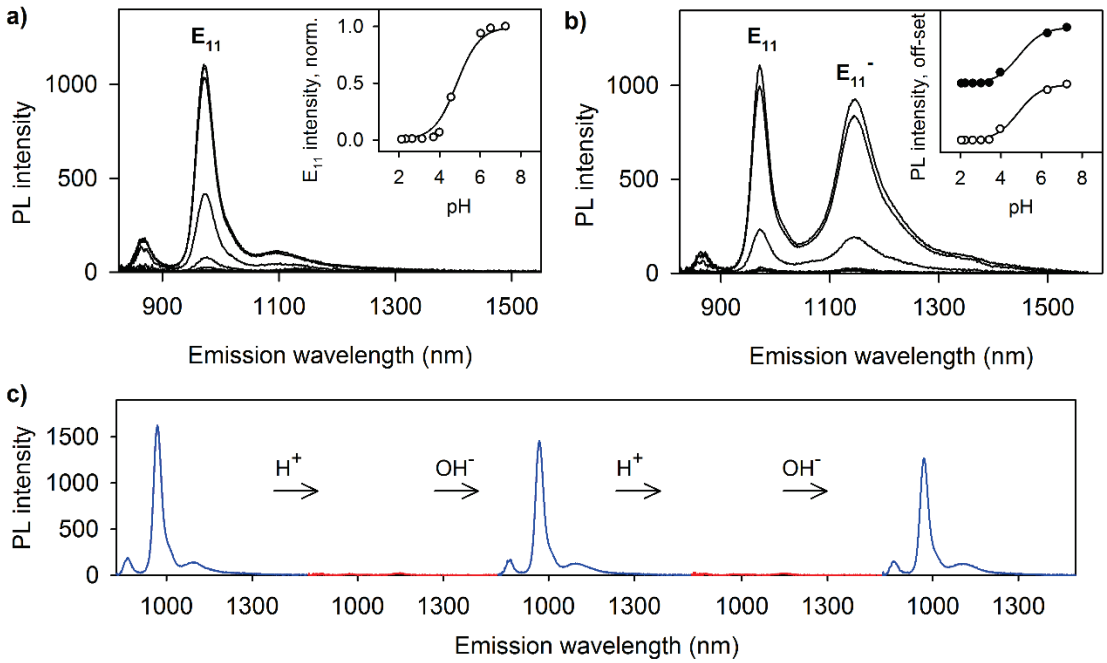

Figure 3-4. Reversibility of acid-induced PL quenching. PL emission spectra (black lines; 565 nm exc.) of both (a) unfunctionalized (6,5)-SWCNT and (b) 3,5-dinitrobenzene-functionalized (6,5)-SWCNT (1% SDS in D_2O) is quenched upon titration with aqueous H_3PO_4. The PL intenisties of both E_{11} (open circles) and E_{11}^- (filled circles) are quenched with decreasing pH. (c) The acid-induced PL quenching is readily recovered upon addition of NaOH. Consecutive additions of phosphoric acid (H^+) and NaOH to unfunctionalized (6,5)-SWCNTs (leftmost spectra, blue) demonstrate that the recovery of PL features, with ~20 % loss in intensity of E_{11} after the 2 acid-base cycles shown here, likely due to the generation of water and salts from the acid-base reactions.

3.2.8. Chirality-Selective Functionalization within a Mixture of (6,5)- and (7,3)-SWCNTs.

To create a well-defined model system, we prepared chirality-enriched solutions of (6,5)- and (7,3)-SWCNTs suspended in SDS and dissolved in D_2O, as

previously described. We then mixed equal amounts of each solution together, using their absorbance at E_{11} as an indicator (Figure 3-5).

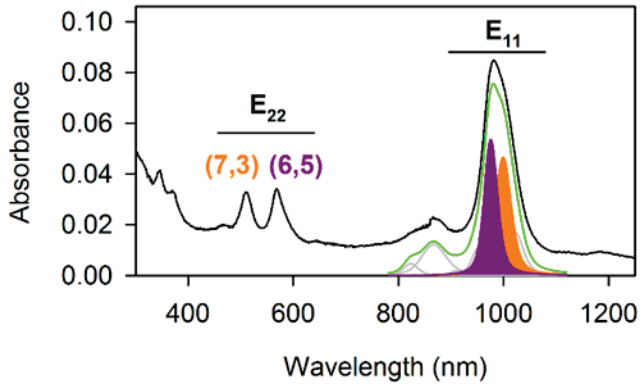

Figure 3-5. Absorbance spectrum of the binary SWCNT mixture used in this study. The absorption spectrum of the mixture enriched in the (7,3)- and (6,5)-SWCNT chiralities reveals well-resolved E_{22} peaks at 505 nm and 565 nm, respectively. E_{11} peaks are deconvolved by spectral fitting with baseline adjustment.

The pH of the SWCNT suspension was adjusted to 3.8 with H_3PO_4 in D_2O. From this solution, we made three 1 mL samples to which an aliquot of 3-*O*-*p*-nitrobenzenediazoascorbic acid in D_2O was added to achieve a molar ratio of 1:500 [*p*-NO_2-DZE]:[SWCNT carbon]). One of the samples was protected from light for 4 h, while the other two were either irradiated with 505 nm (E_{22} of (7,3)-SWCNT) or 565 nm (E_{22} of (6,5)-SWCNT) light for the same time period. The intensity of the light was approximately the same (9.9 mW cm^{-2} *vs*. 9.5 mW cm^{-2} for 505 nm and 565 nm, respectively) for each irradiated sample. Then the samples were titrated with NaOH to pH 7.4 for the PL measurements.

3.2.9. Computational Methodology.

Geometry optimization and frequency calculations were performed for the *E*- and *Z*-isomers of 3-*O*-*p*-nitrobenzenediazoascorbic acid at either protonation state of the O-2 atom (where the total charge of the molecule, q, is 0 and -1), using density functional theory (DFT) at the B3LYP/ 6-31G+(d,p) level of theory as implemented in the Gaussian 09 software package.[84] Solvent effects were included by creating a solute cavity via a set of overlapping spheres in the framework of the polarizable continuum model using the integral equation formalism variant (IEFPCM).[85] Water ($\varepsilon = 78.3553$) was chosen as the solvent media. By normal mode analysis, only real (positive) vibrational frequency values were obtained for all isomers (*E* and *Z*) in both protonation states (q = 0 and q = -1), demonstrating that the optimized geometries (Figure 3-6) correspond to the minima on the potential energy surface. The *E*-isomers had N-O bond lengths of 1.39 and 1.41 Å in the cases of protonation and deprotonation, respectively. However, we found that the optimized geometries of the *Z*-isomer have extended N-O bond lengths (2.45 Å and 2.37 Å in the case of the protonated and deprotonated structures, respectively) corresponding to two non-covalently bonded species, ascorbate and *p*-nitrobenzenediazonium, as opposed to the covalently bonded *Z*-isomer.

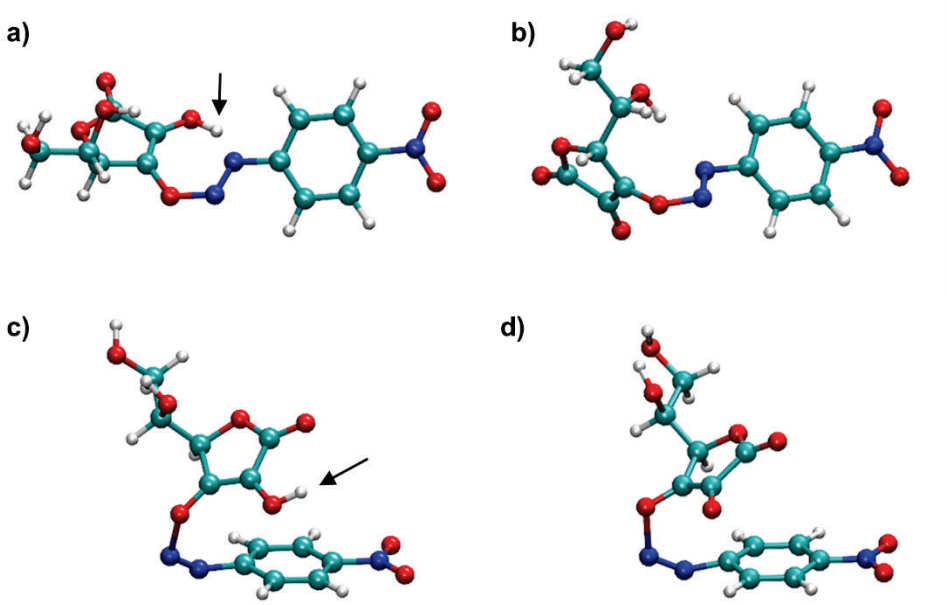

Figure 3-6. Optimized molecular structures of 3-*O*-*p*-nitrobenzenediazoascorbic acid. The optimized geometries of (a) protonated *E*-, (b) deprotonated *E*-, (c) protonated *Z*-, and (d) deprotonated *Z*-isomers were calculated using DFT at the B3LYP/6-31G+(d,p) level of theory. The black and gray arrows denote the O-2 atom and the protons at the O-2 atom, respectively. Each element is color-coded: white for hydrogen, red for oxygen, cyan for carbon, and blue for nitrogen.

In order to find the saddle point, we fixed the N-O bond distance, decreasing its length from the initially determined value to 1.4 Å (0.100 Å and 0.050 Å step size in the cases of protonation and deprotonation, respectively), while allowing all the internally redundant coordinates to relax, using the same functional and basis set (Figure 3-7).

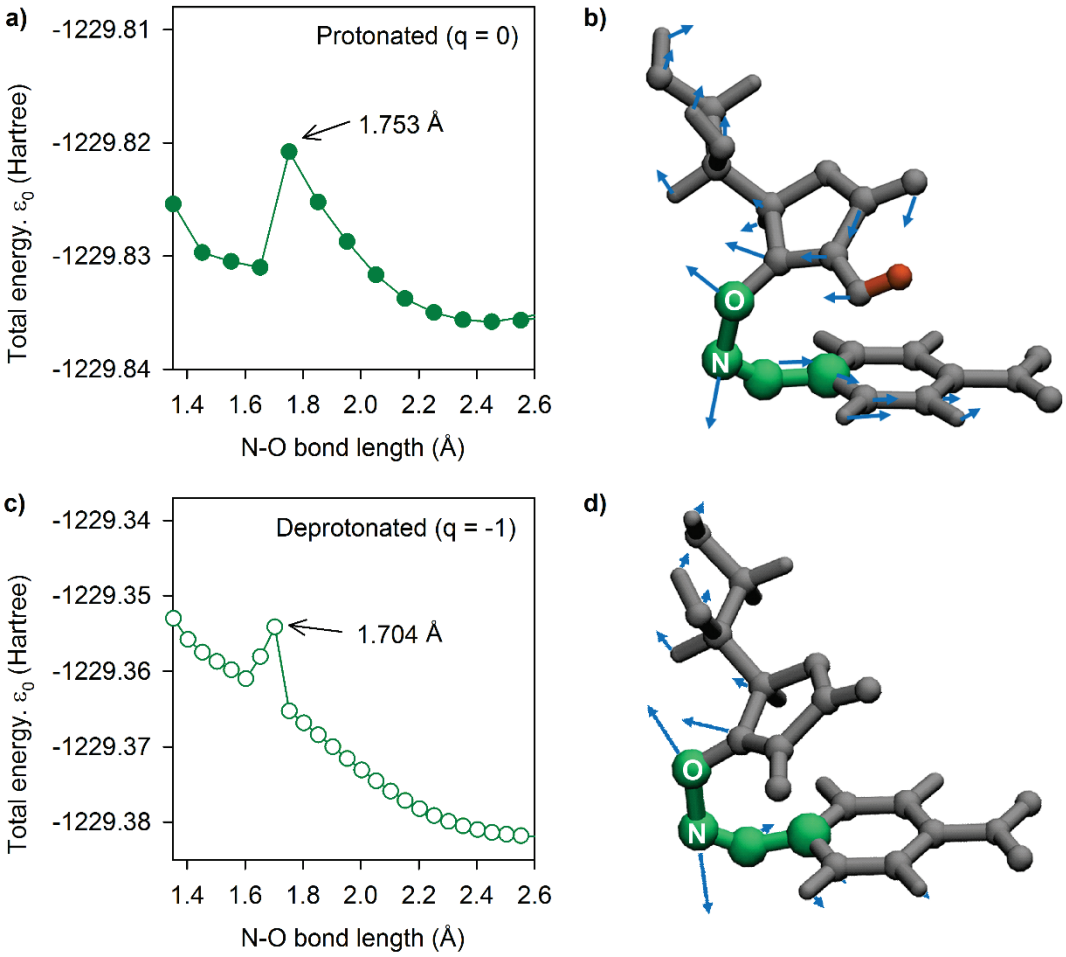

Figure 3-7. Geometry scan of the *Z*-isomer of 3-*O*-*p*-nitrobenzenediazoascorbic acid as a function of the N-O bond length. The geometries of the *Z*-isomer were scanned about the transition state by varying the N-O bond length from ~2.6 Å to 1.4 Å. In both the cases of (a) protonation and (c) deprotonation at O-2, the total energy of the isomer reached a maximum at ~1.7 Å. The geometry at this critical point was optimized further to find the local energy minimum. Vibrational normal mode vectors (black arrows) at the imaginary (negative) vibration frequency of the geometry optimized *Z*-isomer when either (b) protonated or (d) deprotonated at the O-2 atom are presented.

We found that at ~1.7 Å, the total energy of the molecule reached a maximum, beyond which the geometry minimized to the predicted sandwich-like *Z*-isomer. A constrained optimization of the geometry at this critical bond length was performed by

applying tight convergence criteria to the calculation, resulting in N-O bonds lengths of 1.73 and 1.70 in the cases of protonation and deprotonation, respectively for the *Z*-isomers. The frequency analysis revealed one imaginary (negative) vibrational frequency. The imaginary frequency is attributed to the stretching of the N-O bond, suggesting that this bond is only weakly covalent resulting in the instability of the *Z*-isomer geometry. We calculated the thermodynamic values for the *E*-to-*Z* isomerization using the geometries of the *Z*-isomers calculated in this manner. The equilibrium constants at 21 °C and 70 °C were calculated using these calculated thermochemical values and the van 't Hoff equation.

The thermodynamic barrier to isomerization for the diazoether isomers, ΔG^{o}_{iso}, at either protonation state was computed by eq. (3-6).

$$\Delta G^{o}_{iso} = (\varepsilon_0 + C_{Gibbs})_Z - (\varepsilon_0 + C_{Gibbs})_E \quad (3\text{-}6)$$

in which ε_0 is the electronic energy and C_{Gibbs} is a correction factor for Gibbs energy due to the internal energy. The $(\varepsilon_0 + C_{Gibbs})$ values are directly obtained from ground state frequency calculations. Similarly, the enthalpy of the isomerization was derived using the corresponding correction factor.

3.3 Results and Discussion

3.3.1. Two Isomers with Distinct Reactivity for Semiconducting SWCNTs.

We synthesized a pair of 3-*O*-*p*-nitrobenzenediazoascorbic acid (*p*-NO_2-DZE) isomers by coupling an aryldiazonium salt to ascorbate (Figure 3-8a). First isolated by Doyle *et al*. in 1989,[83] the *E*-isomer of this ascorbate diazoether compound is stabilized

in comparison to other *O*-coupling derivatives of aryldiazonium by its pseudo-ring structure.[86-88]

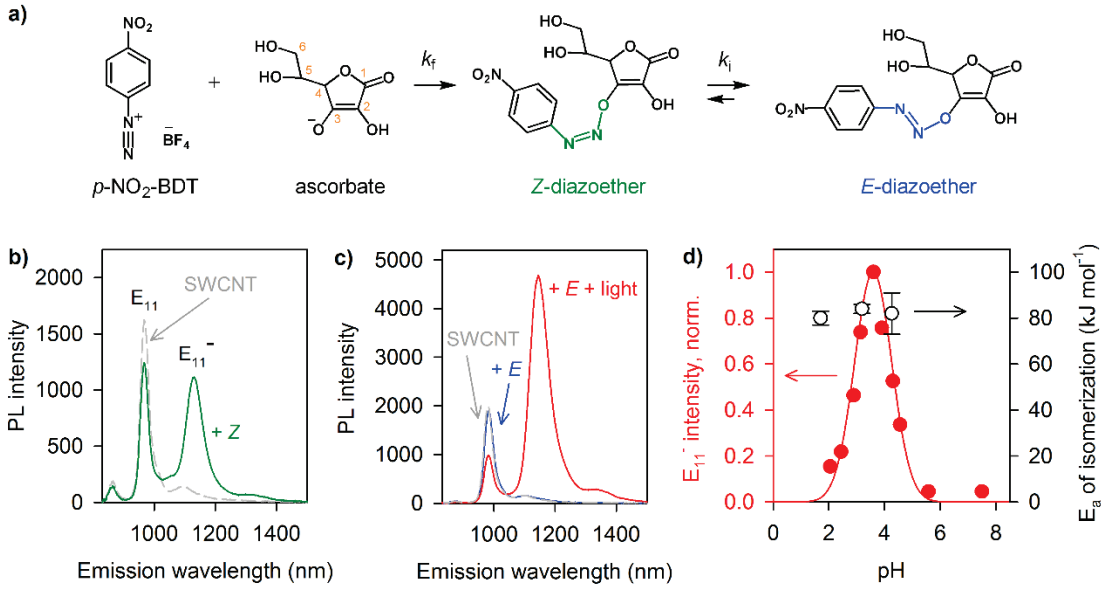

Figure 3-8. Diazoether stereoisomers exhibit distinct pH-dependent reactivity toward semiconducting SWCNTs. (a) Schematic showing the *O*-coupling reaction between ascorbate and *p*-nitrobenzenediazonium tetrafluoroborate (*p*-NO_2-BDT) to synthesize the diazoether isomers. The atoms on ascorbate are numbered for clarity. (b) The Z-isomer reacts readily with (6,5)-SWCNTs (pH 6.4, green), as determined by monitoring the evolution of the defect PL (E_{11}^-) at 1141 nm (λ_{ex} = 565 nm). (c) In contrast, the *E*-isomer is inert with SWCNT (blue) unless activated by SWCNT-resonant irradiation (λ_{ex} = 565 nm, pH 3.8, red). (d) The optical reactivity of the *E*-isomer can be tuned with pH (red filled circles) as determined by the PL intensity of the E_{11}^- state. The PL intensities of E_{11}^- for each experiment were normalized to that of the highest value for comparison. All PL measurements were taken at pH 7.5, regardless of the pH condition during irradiation. The activation energy for *Z*-to-*E* isomerization (E_a, of isomerization, open circles) does not vary significantly with pH as determined by pH- and temperature-dependent kinetic experiments.

In order to determine the reactivity of the two *p*-NO_2-DZE isomers with semiconducting SWCNTs, we added an aliquot of an aqueous solution containing either the *Z*- or *E*-diazoether to a suspension of HiPco SWCNTs that had been enriched in the (6,5) chirality by gel chromatography and monitored the reaction via PL spectroscopy. The chirality enrichment of the SWCNT suspension results in a well-defined system for clear observation of the PL from both the intrinsic (E_{11}) and defect (E_{11}^-) excitonic emission states that allowed us to monitor the reaction progress. The results from spectroscopic monitoring of the reaction show that the *Z*-isomer readily reacts with (6,5)-SWCNT to introduce covalently bonded *p*-nitroaryl functional groups to the carbon surface (Figure 3-8b), which is in contrast to a previous report where the reactivity of the *Z*-isomer was not observed with semiconducting SWCNTs.[77] Upon reaction with the *Z*-isomer, defect PL from the E_{11}^- state (1141 nm) was observed, redshifted from that of the E_{11} exciton emission (980 nm). Conversely, when a similar experiment is performed using the *E*-isomer, defect PL was not observed (Figure 3-8c).

3.3.2. Light-Activated Chemistry on Semiconducting SWCNTs with the *E*-Diazoether.

Despite the *E*-isomer's apparent inactivity within the limits of our sensitive spectral technique, we found that it could be activated by optically exciting the SWCNT within a particular pH range. After the reactants were irradiated with 565 nm light for 5 h (pH 3.8, 21 °C), we observed strong defect PL. Notably, while the wavelength of incident light (565 nm) resonates with the E_{22} excitonic transition of (6,5)-SWCNT, it does not resonate with the diazoether compound as is evident from the optical absorption spectra of the reactants. We also note that care was taken to avoid pH-

dependent PL effects in this work by taking PL measurements at the same and approximately neutral pH. The optical selection technique suggests reaction specificity can be obtained, localized to a certain chirality via the resonant excitation, as discussed in our previous work with diazonium salts.[63] Monitoring the temporal evolution of the defect PL was complicated by the quenching effect of the acid-base reaction products necessary for consecutive PL measurements. For this reason, extensive kinetic studies were not completed, but we do show that defect PL evolves with time in Figure 3-9 in the case of the photo-activated reaction of (6,5)-SWCNT with the *E*-isomer of the diazoether at pH 3.69.

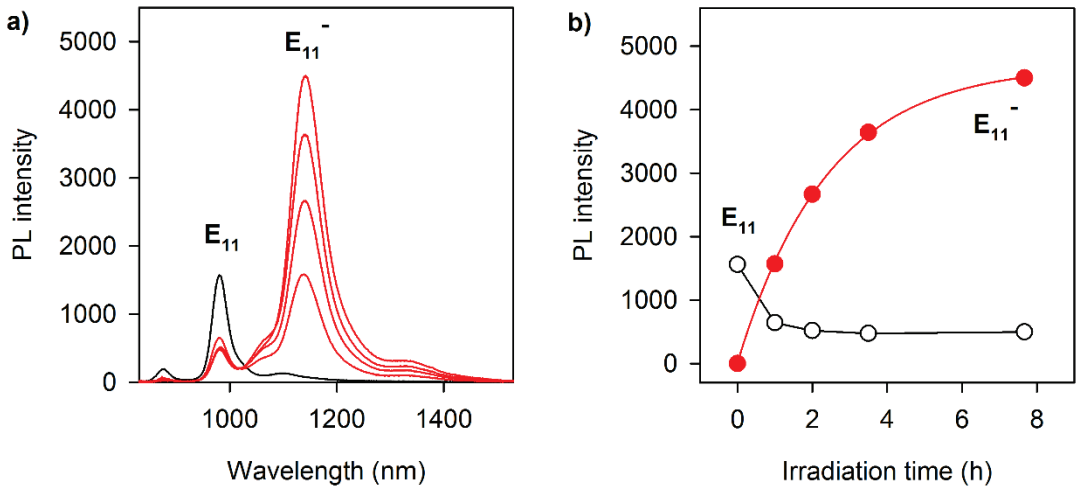

Figure 3-9. Evolution of defect PL with time in the case of photo-induced functionalization of (6,5)-SWCNT with the *E*-diazoether. (a) PL spectra (excitation = 565 nm) and (b) temporal evolution of intrinsic (E_{11}) and defect (E_{11}^-) PL of (6,5)-SWCNTs functionalized by the *E*-diazoether at pH 3.69. To combat the quenching effect of the acid-base reaction products in consecutive PL measurements, each data point represents an independent sample which was irradiated for the time indicated in (b) before the pH was increased to 7.5 for spectral measurement.

We explored the reaction's dependence on pH and found that the reaction maximizes at pH 3.8 about a narrow range (Figure 3-8d). In order to understand the origin of this pH-dependence, we investigated the energetic barriers associated with *Z*-to-*E* isomerization. We experimentally determined the activation energy for isomerization (E_a) by monitoring the coupling reaction in aqueous solution *in situ* by UV-visible absorption spectroscopy. These measurements revealed the isomerization of the *Z*-isomer of *p*-NO_2-DZE (λ_{max} = 290 nm) to the thermodynamically stable *E*-isomer (λ_{max} = 360 nm). We monitored spectra changes associated with the isomerization at temperatures ranging from 12 °C to 27 °C and pHs spanning the *E*-isomer's reactivity window, from 1.70 to 4.26.

We used a first-order kinetic model to describe the *Z*-to-*E* isomerization and found that the activation energy for isomerization did not vary significantly with pH within the reactivity range of the *E*-isomer (Figure 3-8d). While the reaction proceeds via two steps, the rate constants of which are given by k_f, and k_i, we observed that the formation of the *Z*-isomer (first coupling step) is much faster than the isomerization step, such that $k_f >> k_i$, suggesting that isomerization is the rate-limiting step so that it can be described independently. We note that while Darchy *et al.*[77] also models the isomerization step using a similar first order model, we derived a different equation which takes into account the spectral overlap between the two isomers and expanded the study to uncover the pH dependence of the activation energy. The related rate expression for the isomerization step is given by eq. (3-7).

$$\frac{d[Z]}{dt} = -k_i\,[Z] \tag{3-7}$$

in which $[Z]$ is the concentration of the *Z*-isomer and t is time. The concentration of the *Z*-isomer at time t is given by eq. (3-8), which accounts for the spectral overlap of the two isomer's absorbance peaks.

$$ln[Z]_t = ln(3.259A_t(Z) - A_t(E)) + C \quad (3\text{-}8)$$

in which C is a constant. By plotting $ln[Z]_t$ versus time, we obtained highly linear relationships (Figure 3-10). The rate constants for *Z*-to-*E* isomerization were inferred from the linear regressions of these plots. We applied Arrhenius theory, eq. (3-9), to determine the activation energy for isomerization, activation energy at various pH, $E_a(pH)$.

$$\ln k_i = -\frac{E_a(pH)}{R}\left(\frac{1}{T}\right) + \ln A \quad (3\text{-}9)$$

in which R is the gas constant, T is temperature and A is the pre-exponential factor.

From plots of $\ln k_i$ versus T^{-1}, we extracted $E_a(pH)$ from the slopes of the linear regressions. We experimentally determined this barrier to be a deep energetic trap for the *E*-isomer, (80 ± 3) kJ mol^{-1} at pH 1.70, which is in accord with a previous report.[77] We studied the pH dependence of this barrier and found that while the isomerization rate constants varied considerably with pH and temperature, the activation energy itself was stable despite the change in reactivity of the *E*-isomer within this range. We did not expand our kinetic study beyond pH 4.26 because isomerization occurred too quickly to reliably monitor at elevated temperatures, which resulted in significant uncertainty in the calculated energy values. Isomerization from the *E*-to-*Z* isomer was not observed experimentally, possibly reflecting a significantly larger activation energy for this process.

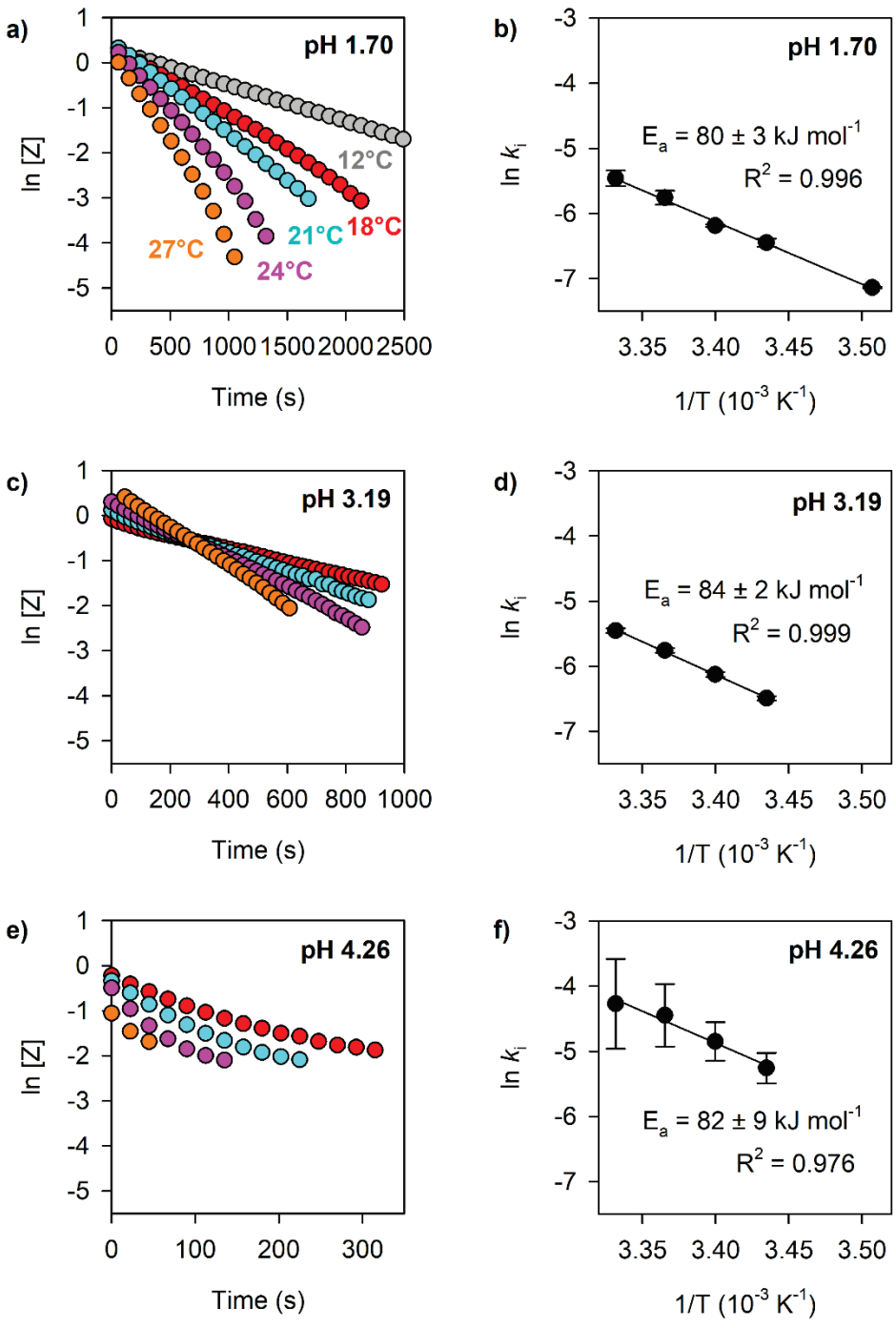

Figure 3-10. Activation energy for isomerization from the *Z*-isomer to the *E*-isomer of 3-*O*-*p*-nitrobenzenediazoascorbic acid by Arrhenius theory. (a, c, e) First-order plots of the temperature- and pH-dependent isomerization. (b, d, f) By application of the Arrhenius equation, the activation energy for isomerization (E_a) does not appear to vary significantly with pH.

3.3.3. Switchable Reactivity of the *E*-Diazoether with pH.

The photo-induced reaction could be switched on and off by alternating the pH of the solution. In Figures 3-11, we demonstrate this high level of control by switching the pH of the reaction between 3.8 and 7.4 (*i.e.*, the reactive and inactive reaction regimes, respectively) and observed a corresponding pattern in the evolution of defect PL when the sample was irradiated, revealing the responsive nature of the thermodynamic barrier to isomerization.

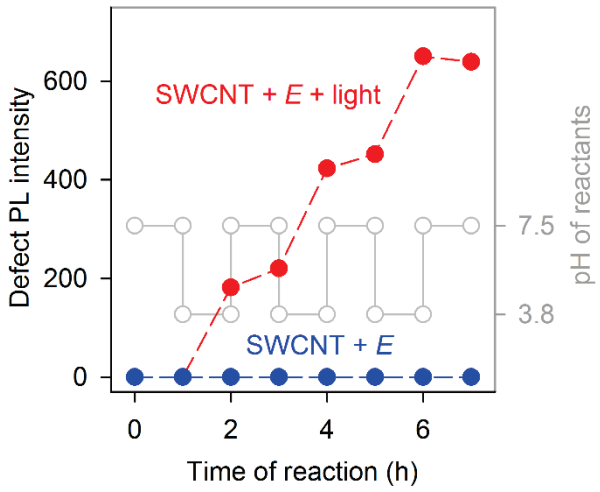

Figure 3-11. The stable *E*-diazoether can be activated via light and pH to functionalize SWCNTs. Step-wise reactivity of the *E*-isomer with (6,5)-SWCNTs was achieved with irradiation (565 nm, red) and pH switching (grey) as compared to the dark control (blue). All PL measurements were obtained at pH 7.5 regardless of the pH condition during each reaction interval.

Interestingly, even as we changed the $[H^+]$, we did not detect any defect PL when the sample was protected from light, which indicated the importance of the resonant optical excitation of the nanostructure for the reaction to occur (Figure 3-12).

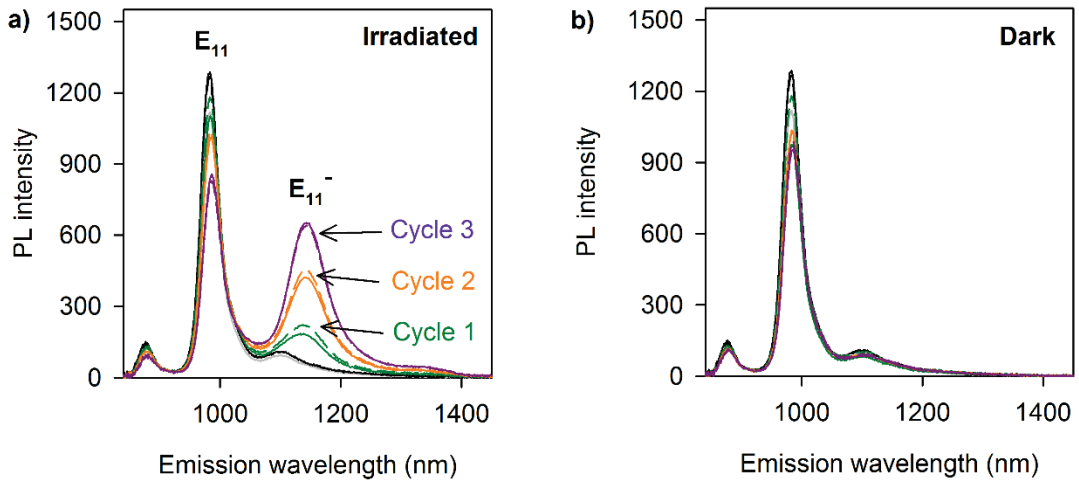

Figure 3-12. Switchable reactivity of diazoethers. PL spectra (ex = 565 nm) showing the (a) step-wise increase in defect PL when samples are irradiated with 565 nm light (~ 8 mW cm^{-2}) versus (b) inactivity when samples are protected from light despite varying the pH between 3.8 and 7.5 at each cycle. Solid and dashed lines indicate spectra taken prior to and immediately after each 1 h cycle (at pH 3.8), respectively. All measurements were taken at pH 7.5 and 21 °C.

3.3.4. Thermal Effects on Functionalization of SWCNTs by the *E*-Diazoether.

In order to better understand whether the role of irradiation on the reaction of SWCNT with the *E*-isomer of diazoether is to simply induce a bulk heating effect rather than a localized, chirality specific one, we explored the pH dependence upon heating (Figures 3-13 and 3-14).

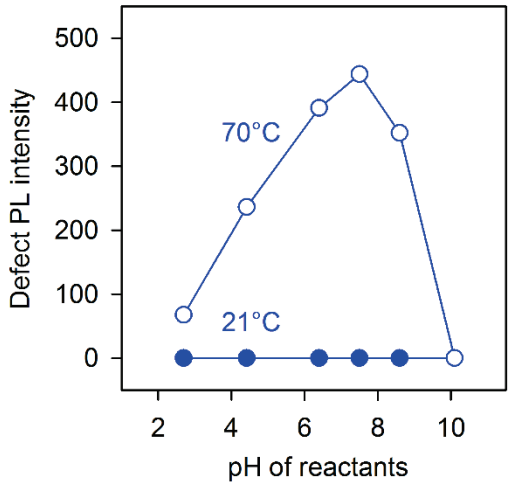

Figure 3-13. pH dependence of the thermal reaction of (6,5)-SWCNTs with the *E*-diazoether. The dependence of defect PL on solution pH for suspensions of (6,5)-SWCNT reacted with the *E*-diazoether and were protected from light at either 21 °C (filled circles) or 70 °C (open circles). The pH-dependence is significantly broadened compared to that of the photo-controlled reaction maximum.

Solutions of (6,5)-SWCNT and the *E*-isomer at different $[H^+]$ were reacted at either 21 °C or 70 °C with protection from light throughout reaction. Their PL was measured after adjusting the pH to 7.5 and cooling the solution down to 21 °C. Interestingly, no defect PL was observed when the reaction was maintained at 21 °C. Upon heating to 70 °C, the pH dependence broadened significantly, in comparison to the photo-controlled reaction, and maximized at a pH of ~7.5.

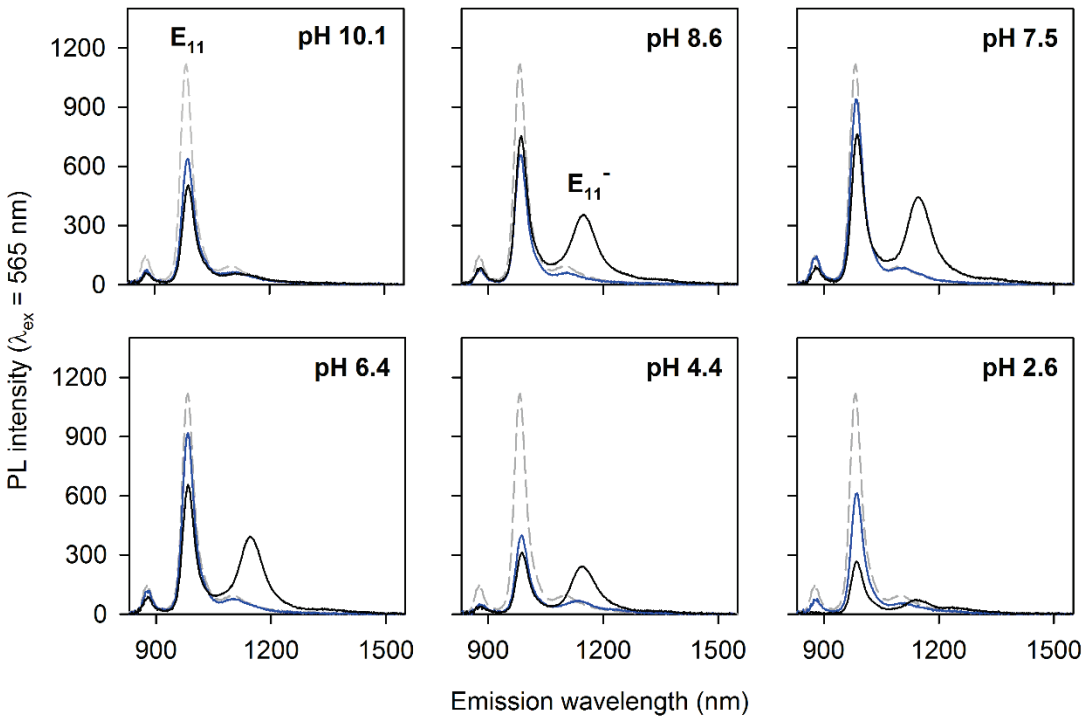

Figure 3-14. Thermally-accelerated functionalization of (6,5)-SWCNTs with the *E*-diazoether. PL emission spectra (565 nm exc.) of (6,5)-SWCNTs that were reacted with the *E*-diazoether at either 21 °C (blue) or 70 °C (black). PL emission spectrum of unfunctionalized (6,5)-SWCNTs (grey, dashed) is shown for reference.

The observed pH dependence of the *E*-isomer's reactivity may reflect the pH-dependence of isomerization energy from the inactive *E*-isomer to the reactive *Z*-isomer. The *E*-isomer of *p*-NO_2-DZE is stabilized in a pseudo-ring structure via hydrogen bonding between the N_α and the proton at the O-2 atom,[86] the pK_a of which is 10.2, as shown in Figure 3-15.[83]

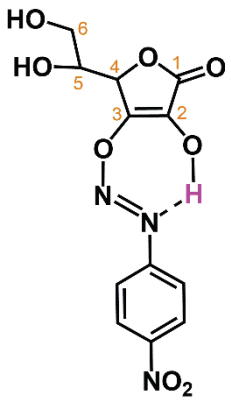

Figure 3-15. *E*-diazoether geometry. The *E*-isomer of the ascorbate diazoether is stabilized by H-bonding to form a pseudo-ring structure.

The *Z*-isomer of this particular diazoether consists of a sandwich-like structure with an extended N-O bond.[77] This thermodynamically unstable structure is prone to cleavage (as evidenced by its reactivity with SWCNT shown here) or quickly isomerizes to the more stable *E*-isomer. While the activation energy for isomerization does not vary significantly with pH as previously discussed, the stability of the *E*-isomer, versus that of *Z*-isomer, may be reflected in the thermodynamic barrier to isomerization. Furthermore, because the stabilizing pseudo ring structure of the *E*-isomer is dependent on hydrogen bonding, it is hypothesized that its stability may be tuned with H^+, which is utilized to control its reactivity as explored in this work.

3.3.5. Thermodynamic Barrier to Isomerization from *E*-to-*Z*.

Density functional theory (DFT) calculations revealed that the thermodynamic barrier to isomerization, Gibbs free energy (ΔG°_{iso}), from *E* to *Z* is dependent on the protonation state of the O-2 atom (Figure 3-16).

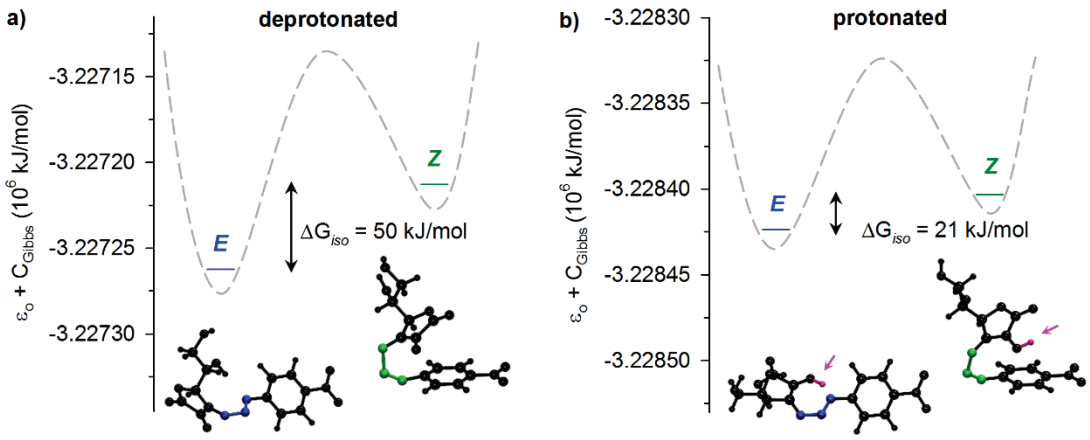

Figure 3-16. Calculated Gibbs free energies of isomerization. The magnitude of the thermodynamic barrier to isomerization (ΔG_{iso}, conventionally defined as the isomerization energy) is dependent on whether the O-2 atom of the diazoether is (a) deprotonated or (b) protonated. Energies were calculated using DFT at the B3LYP/6-31G+(d,p) level of theory. The y-axes are the sum of the electronic energy (ε_o) and the correction factor for Gibbs free energy (C_{Gibbs}) and have the same magnitude (see Materials and Methods). The pink arrows in (b) denote the protons. Calculated values are indicated by solid lines, and dashed lines show putative isomerization through the transition state, whose peak height was obtained from experiment).

We performed geometry optimization and frequency calculations of the isomers to obtain the isomers' ground state energies under different protonation states (Table 3-2). We found that protonation of the O-2 atom reduced the ΔG°_{iso} by 58%, from 50 kJ mol^{-1} to 21 kJ mol^{-1}. This explains the strong pH dependence observed from our optical excitation experiments performed at 21 °C, where the reaction was most efficient at low pH, maximizing at pH 3.8, where the O-2 atom is protonated.

Table 3-2. Calculated thermochemical values of *E*-to-*Z* isomerization of 3-*O*-*p*-nitrobenzenediazoascorbic acid at either protonation state of O-2. Gibbs free energies, enthalpies, and entropies of *E*-to-*Z* isomerization were obtained from thermochemical calculations using the DFT method at the B3LYP/6-31G+(d,p) level of theory. K_{eq} is the equilibrium constant corresponding to [*Z*-isomer]:[*E*-isomer].

	Protonated (q = 0)	**Deprotonated (q = -1)**
ΔH_{iso} (kJ mol^{-1})	16	42
ΔG_{iso} (kJ mol^{-1})	21	50
ΔS_{iso} (J $mol^{-1} \cdot K^{-1}$)	-15	-25
K_{eq} at 21 °C	2.3 x 10^{-4}	1.6 x 10^{-9}
K_{eq} at 70 °C	5.9 x 10^{-4}	2.0 x 10^{-8}

We also calculated the enthalpy (ΔH°) and entropy (ΔS°) of isomerization under the two protonation states to better understand the effect of heating on the reaction's pH dependence. Experimentally, we observed significant broadening of the reaction's pH dependence at 70 °C (*vs.* 21 °C). The van 't Hoff plots have negative slopes (Figure 3-17), confirming that the *E*-to-*Z* isomerization is thermodynamically unfavorable for both high and low pHs. However, in their deprotonated states, the isomerization from *E*-to-*Z* is more sensitively dependent on temperature. Furthermore, the calculated equilibrium constant of isomerization, K_{eq}, increases more significantly with temperature when deprotonated, which coincides with a 2.4-fold increase in the slopes of the van't Hoff plots upon deprotonation. These experimental observations are in good agreement with the values derived from the computation. The strong temperature dependence suggests that optically-induced local heating[89] plays an

important role in triggering the reaction by thermally switching the physically absorbed *E*-diazoether to the reactive *Z*-isomer.

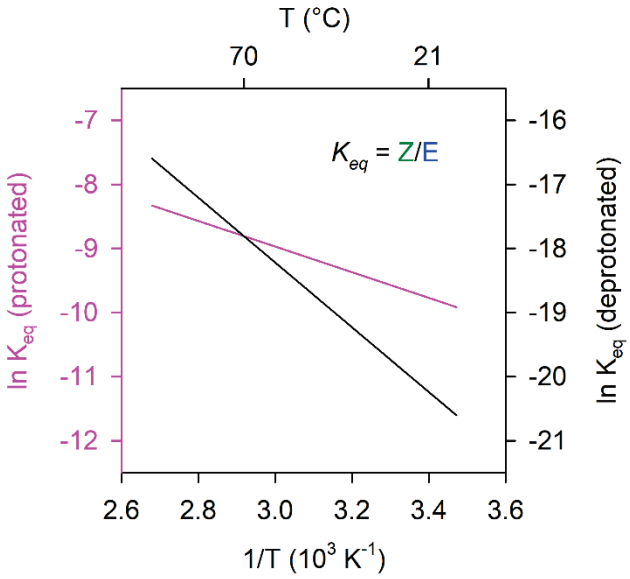

Figure 3-17. Van 't hoff plots generated from DFT frequency calculations of the geometry-optimized isomers based on protonation state at O-2. K_{eq} is the equilibrium constant for isomerization, [*Z*-isomer]:[*E*-isomer]. Note the steeper slope in case of deprotonation at O-2, indicating a more significant dependence on temperature.

3.3.6. Chirality-Selectivity in a Binary Mixture of SWCNT Chiralities.

We further exploited the observed photo-activated and pH-dependent reactivity for chirality selective covalent functionalization of semiconducting SWCNTs (Figures 3-18 and 3-19). As a demonstration, we irradiated suspensions enriched in the (6,5)- and (7,3)-SWCNT chiralities using light that resonated with only one of the structures. We aimed to drive covalent bonding of the *E*-isomer on the surface of this target chirality and to locally switch its reactivity via chirality-specific photoexcitation. We chose a system consisting of the (6,5)- and (7,3)-SWCNT chiralities for this experiment

because their E_{22} optical transitions are well-resolved (505 nm *vs.* 565 nm for (7,3) and (6,5), respectively), allowing for unambiguous illustration of the high optical selectivity of the reaction.

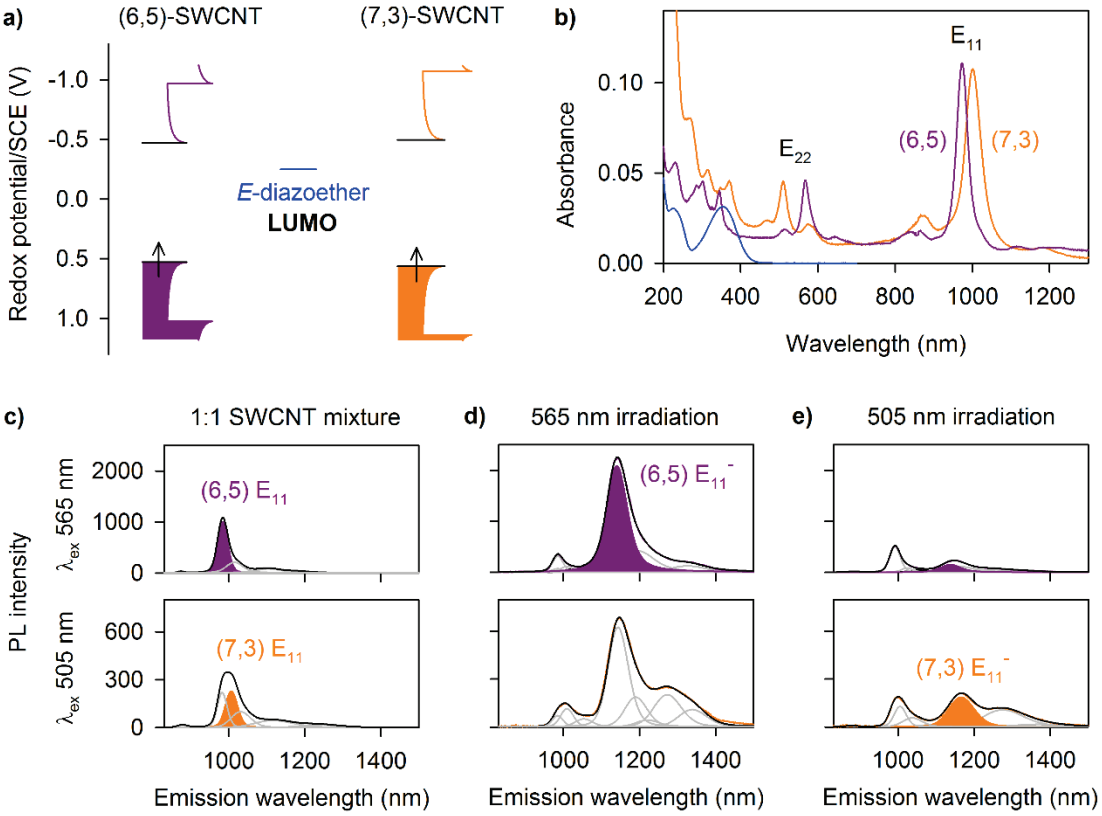

Figure 3-18. Chirality selective functionalization of SWCNTs within a mixture using the *E*-diazoether. (a) Redox potentials (black lines) of the (6,5)-SWCNT,[69] (7-3)-SWCNT, and the *E*-diazoether.[77] The redox potential of the (7,3)-SWCNT was deduced based on the relative band gap energy. (b) Absorption spectra of SDS-suspended (6,5)- and (7,3)-SWCNTs in D_2O. The E_{22} peaks of these two chiralities are sufficiently separated so that they can be optically excited exclusive of each other and the *E*-diazoether (blue line, 50 µM aqueous solution, x 1/12 for clarity). Resonant PL emission spectra resulting from excitation at 565 nm (top) and 505 nm (bottom) of each sample, which is either (c) the unfunctionalized mixture or irradiated with (d) 565 nm or (e) 505 nm light.

We note that relative SWCNT reactivity is correlated with diameter (0.706 nm *vs.* 0.757 nm, for (7,3) and (6,5), respectively),[90] E_{11} optical frequency (990 nm *vs.* 976 nm, for (7,3) and (6,5), respectively),[81] and redox potentials. Specifically, (7,3)-SWCNT is less reactive with aryldiazonium salts than (6,5)-SWCNT.

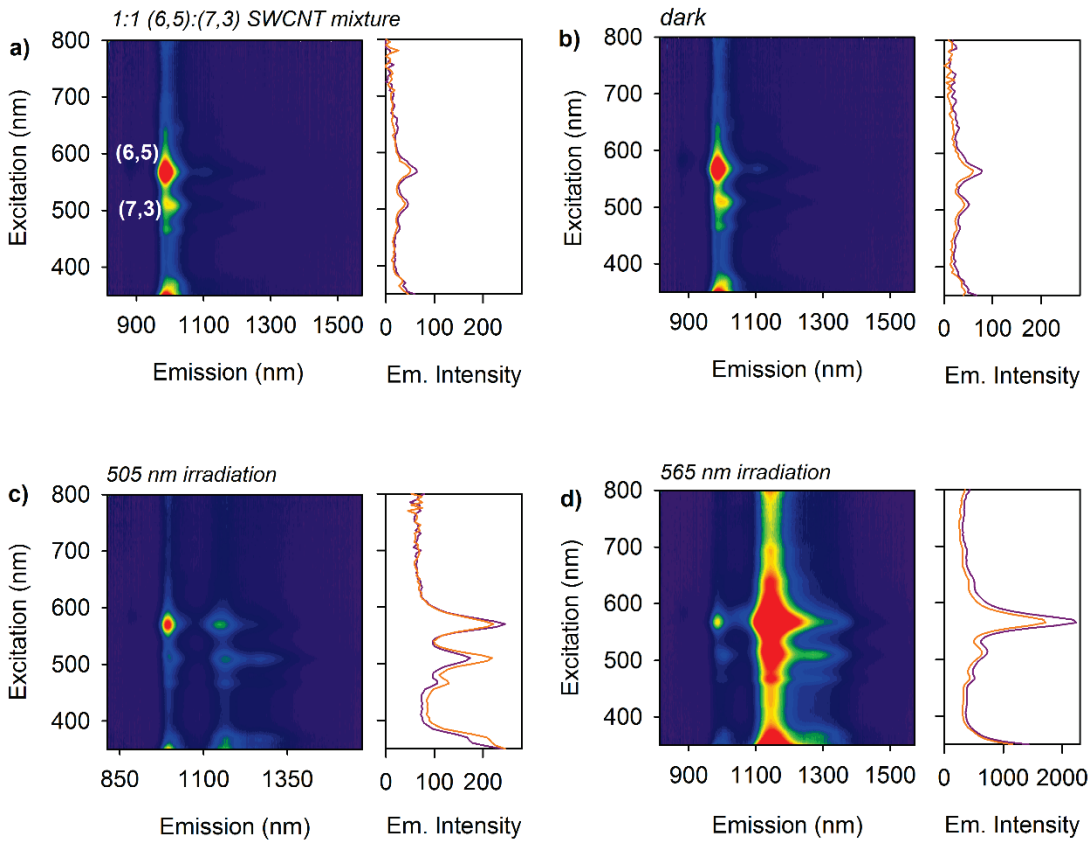

Figure 3-19. PL excitation-emission maps of 1:1 (7,3):(6,5)-SWCNTs from the chirality-selective functionalization study. PL excitation-emission maps and PL excitation spectra showing the origin of the defect PL for both chiralities (1141 nm and 1165 nm for (6,5) and (7,3) in purple and orange, respectively) of the 1:1 (7,3):(6,5) suspensions of SWCNTs (a) before reaction, (b) after reaction in the dark, and after irradiation with (c) 505 and (d) 565 nm light.

Surprisingly, we observed that the less reactive (7,3)-SWCNT is selectively functionalized *vs*. the more reactive (6,5)-SWCNT using this chemistry and (7,3)-resonate photoexcitation, as suggested by the integrated intensity of the defect PL (Tables 3-3 and 3-4).

Table 3-3. Selectivity resulting from wavelength-dependent functionalization within a mixture of SWCNT chiralities. Integrated peak areas from spectral fitting are tabulated for samples either protected from light or irradiated for 4 h.

	E_{11} integrated area		**Defect PL (E_{11}^-) integrated area**		**E_{11}^-/E_{11}**	
Condition	**(7,3)**	**(6,5)**	**(7,3)**	**(6,5)**	**(7,3)**	**(6,5)**
Pristine control	11.90	45.73	0	0	0	0
Dark control	12.75	46.76	0	0	0	0
505 nm Irradiation	6.67	23.38	15.05	11.30	2.26	0.75
565 nm Irradiation	6.31	14.78	0	156.85	0	24.87

When irradiated with light that resonates with the more reactive (6,5) chirality (565 nm), the reaction was limited exclusively to the (6,5) chirality. In fact, no emission from the (7,3) defect state (1165 nm) was detected, indicating that covalent functionalization of the (7,3)-SWCNT did not occur (within the limits of detection of the spectrofluorometer, which corresponds to less than 0.01% of the carbon atoms bonded to a functional group). Conversely, when irradiated with light that resonates the (7,3) species, we successfully drove functionalization of this less reactive chirality. In

this case, the defect PL from the (6,5) chirality was only ~7.2% of that detected in the 565 nm irradiation experiment.

Table 3-4. Spectral fitting data for the principle PL peaks resulting from chirality-selective functionalization experiment. Data with an asterisk (*) corresponds to non-resonate SWCNT species that appears in the spectra. For example, within the unfunctionalized mixture, excitation at 505 nm results in not only emission of the (7,3) chirality but also (6,5) E_{11}.

	505 nm excitation		**565 nm excitation**	
Condition	**Peak Position (eV)**	**FWHM (meV)**	**Peak position (eV)**	**FWHM (meV)**
Control (pristine)	1.26* 1.24	41* 52	1.26	41
Dark	1.26* 1.24	41* 52	1.26	41
505 nm irradiation	1.26 1.24 1.08	 52 67	1.25 1.09 1.06	41 63 72
565 nm irradiation	1.26 1.23 1.08*	42 49 60	1.26 1.09	41 61

It is also important to note that when the binary mixture was protected from light, no defect PL was detected (Figure 3-20). This indicates that the diazoether chemistry is much more controllable than the light-driven diazonium reaction previously reported by us[63] and oxidation by Star *et al.*[91]

We note that our experimental method, namely the measurement of the defect PL, is associated with some uncertainty in absolute quantification of chirality

selectivity. While the relative PL quantum yield (QY) of the first optical transition (E_{11}) for (6,5)-SWCNTs is higher than that of (7,3)-SWCNTs,[92] the PL QY of defect PL is not yet quantitatively correlated with the degree of functionalization. Characterization by other spectral methods was impeded by their potential to induce functionalization from the intense incident light (*e.g.*, Raman scattering) and the extremely low functional degree of the SWCNT, which lies below the limit of detection of readily available methods.[9]

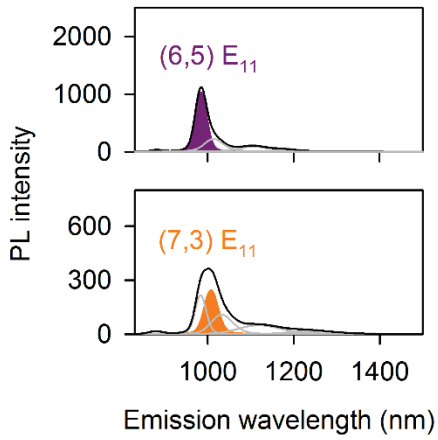

Figure 3-20. PL emission spectra of the dark control with peaks fitted from the chirality-selective functionalization study. Deconvolved PL emission spectra of the 1:1 (7,3):(6,5) mixture that was reacted the *E*-diazoether in the dark shows no defect PL (λ_{ex} = 565 nm). Spectra were obtained from excitation at 565 nm (top) and 505 nm (bottom).

The PL excitation spectra (Figure 3-21) may serve as a guide on the extent of selectivity possible when resonantly exciting a specific chirality in a mixture. However, the selectivity of the reaction is so high that it can be driven to promote functionalization of the less reactive chirality over the more reactive species.

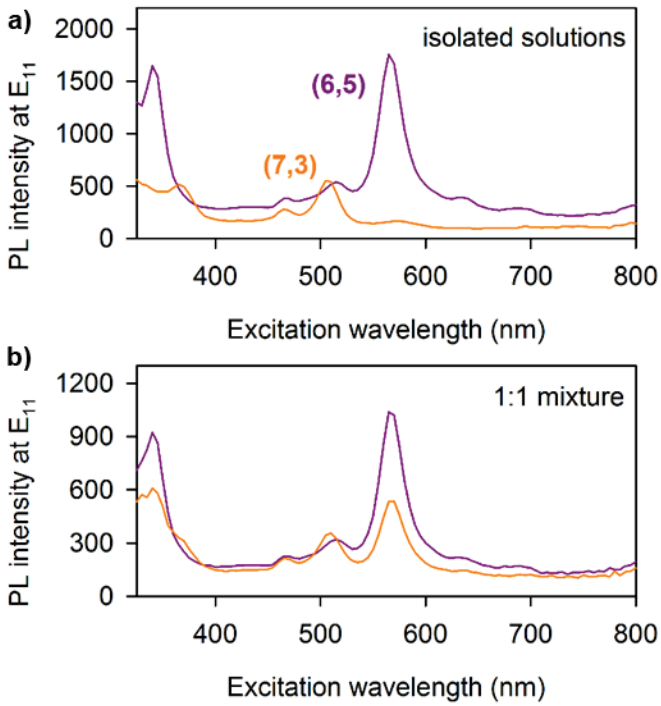

Figure 3-21. Characterization of the binary SWCNT chirality mixture. PL excitation spectra of both the (a) isolated solutions of each (6,5) and (7,3) and (b) the 1:1 mixture of the two chiralities. Purple and orange lines are the PL intensities at 976 nm and 990 nm, the position of the (6,5) and (7,3) E_{11} states, respectively.

The high selectivity of the optically-driven diazoether chemistry arises from the fact that the *E*-diazoether, is trapped deeply in a non-reactive molecular conformation until destabilized by H^+ and triggered optical excitation of the SWCNT substrate to switch its molecular conformation to that of the reactive *Z*-diazoether. This triggered reactivity is significantly more selective than the widely used diazonium salts either with[63] or without optical excitation,[56] as well as the reactive *Z*-diazoether.[77] Our experimental results show that without light and H^+, the reaction can be completely suppressed at room temperature within the limits of our sensitive spectral technique.

3.4 Conclusions

We show that the *E*-diazoether, a molecule that is inert with SWCNT, can be controllably switched to the reactive form by resonant optical excitation of the nanotube substrate and controlling pH. Kinetics studies and DFT calculations reveal a deep energetic trap for the *E*-diazoether whose thermodynamic barrier to isomerization into the reactive *Z*-form can be modulated by pH. Optical excitation of the SWCNTs then drives the reaction selectively to those specific nanotube structures that resonate with the light, by thermally switching the physically absorbed *E*-diazoether to the reactive isomer due to optically-induced local heating, as suggested by the temperature dependence of the reaction. This triggered reactivity serves as the foundation for covalent modification of semiconducting SWCNTs at the chirality-selective level. We experimentally illustrate this chiral selectivity by driving the covalent functionalization of (7,3)-SWCNT in the presence of (6,5)-SWCNT, a structurally similar semiconductor that is intrinsically more reactive. This type of on-demand selectivity may find applications in nanotube sorting, on-chip passivation, and nanoscale lithography.

Chapter 4: Quantum Defects Channel Excitons to New Emissive Sites of Single-Walled Carbon Nanotubes at Ultrahigh Concentrations

Adapted from a manuscript by L. R. Powell,† Y. Piao,† A. Ng, Z. Peng, B. Meany, C. Wang, and Y. Wang.

L.R.P., Y.P., A.N., C.W., Z.P, and B.M. performed experiments. L.R.P. and Y.W. wrote the manuscript with input from all authors. † indicates equal contribution.

4.1. Introduction

Semiconducting single-walled carbon nanotubes (SWCNTs) have been proposed for applications such as fluorescent inks in which they should be present at high concentrations. Researchers have developed effective methods for dispersing SWCNTs in aqueous solutions at high concentrations for use as efficient near-infrared emitters.[93] However, application of nanotube photoluminescence (PL) at high concentrations is challenging due to self-quenching, which is particularly significant in the case of SWCNTs. When left unaddressed, self-quenching leads to significant distortions in spectral analysis.[94] This phenomenon adversely affects the resolution, sensitivity, and reliability of PL from SWCNTs at high concentrations,[95] especially when quantitative measurements are required. Because of this limitation, concentrations of SWCNTs are typically kept within the micro-molar range to prevent self-quenching effects; however, this is not a practical solution in all cases.

While quenching of SWCNT PL in solution may occur due to a variety of both radiative and nonradiative energy transfer mechanisms as well as interactions of

SWCNTs with the environment, in this work we specifically address collisional self-quenching of PL that becomes significant at high concentrations.[96] The increased collisions at high concentrations cause the excitation energy to be transferred to neighboring nanotubes. In the case of SWCNTs, this self-quenching is particularly substantial because of the small Stokes shift (~10 meV) between the emissive state, E_{11}, and the corresponding absorption peak[18] (Figure 4-1a, c). Because of the significant overlap of the two states, energy transfer occurs efficiently between SWCNTs.

In this work we present a strategy to bypass self-quenching by channeling the excitons to a new emissive state that is chemically introduced into the SWCNTs. As a proof of concept, we chemically modify (6,5)-SWCNTs with *p*-nitroaryl functional groups to generate (6,5)-SWCNT-$C_6H_4NO_2$ through aryldiazonium chemistry. The nitroaryl functional group introduces a quantum defect that produces a new emissive state, E_{11}^-, which is distinctly different from the semiconductor host.[9] This new state is not only significantly brighter than the nanotube's intrinsic PL state, E_{11}, but it lies considerably red-shifted (190 meV) from that of the absorption state (Figure 4-1b, d).

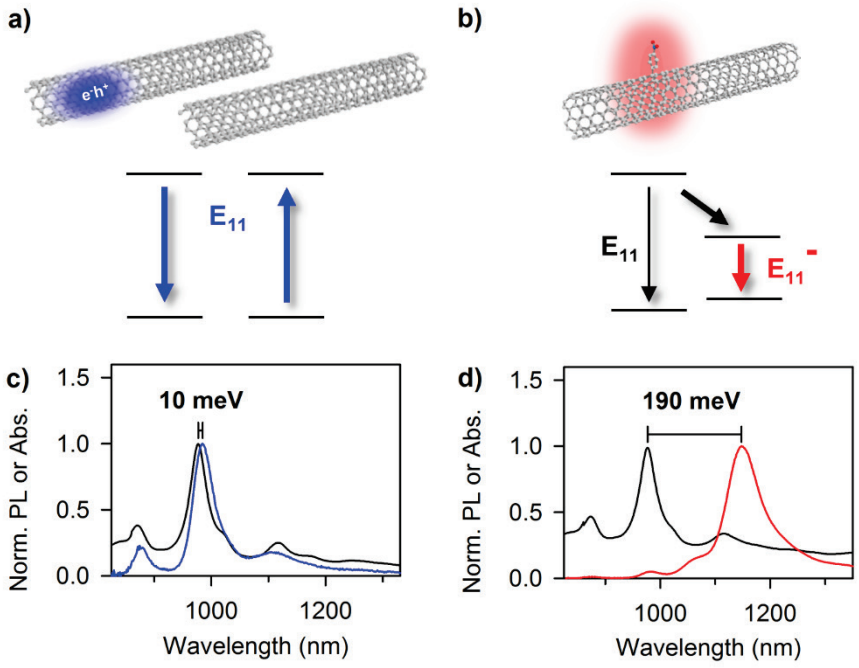

Figure 4-1. Fluorescent quantum defects open a new emission outlet, E_{11}^- in solutions of concentrated SWCNTs. (a, b) Schematics and energy level diagrams illustrate the distinct electronic systems present in solutions of (a) (6,5)-SWCNTs and (b) (6,5)-SWCNT-$C_6H_4NO_2$s. (c, d) Normalized absorbance (black line) and PL emission (λ_{ex} = 565 nm) of (c) (6,5)-SWCNTs and (b) (6,5)-SWCNT-$C_6H_4NO_2$s highlight the dramatic differences in the Stokes shifts of the two emission routes.

4.2. Experimental Methods

4.2.1. Preparation of Chirality-Enriched SWCNT Suspensions.

The SWCNTs were individually suspended by 1% wt./v sodium dodecyl sulfate (SDS, Sigma-Aldrich, 99%) in 99.8% D_2O (Cambridge Isotopes, Inc.). (6,5)-SWCNTs were separated from HiPco materials (batch no. 194.3, Rice University) by gel chromatography using a Sephacryl S-200 HR column (GE Healthcare) and a previously described method.[62] The sorted SWCNTs were then repeatedly loaded onto a single gel

column to concentrate them as much as possible. The concentration was monitored by UV-visible-NIR absorption spectroscopy throughout as will be described in section 4.2.3.

4.2.2. Synthesis of *p*-nitroaryl Modified (6,5)-SWCNTs.

p-nitrobenzenediazonium tetrafluoroborate was synthesized by a method as previously described.[9] Briefly, the diazonium salt (Dz) was synthesized from its complementary aniline (*p*-nitroaniline, 99%, Sigma Aldrich) and nitrous acid (48 wt.% tetrafluoroboric acid solution in water, Sigma Aldrich; sodium nitrite, 97%, Sigma Aldrich). The salt was stored at 0 °C until use. To effect the reaction, an aliquot of the freshly prepared solution of Dz in D_2O was added to a suspension of (6,5)-SWCNTs so that molar ratio of reactants, [Dz]:[SWCNT carbon], was 1:5000. The solution was stirred for 10 days in the dark and monitored using fluorescence excitation-emission maps and UV-visible-NIR absorption spectra. Functionalization was completed at the highest SWCNT concentration available, $(27 \pm 1) \times 10^{13}$ tube mL^{-1} to generate a stock solution that was subsequently diluted for measurements.

4.2.3. Spectroscopic Characterization of SWCNT Suspensions.

Fluorescence emission spectra and excitation-emission maps were collected on a HORIBA Jobin Yvon Nanolog Spectrometer equipped with a 450 W Xenon arc lamp and a multichannel InGaAs array detector. 10 nm and 20 nm slit widths were used for excitation and emission monochromators, respectively. UV-vis-NIR optical absorption spectra were measured using a PerkinElmer Lambda 1050 UV-vis-NIR

spectrophotometer equipped with a photomultiplier tube and a broadband InGaAs detector.

4.2.4. Spectral Fitting of PL and Absorption Spectra.

PL emission and UV-vis-NIR optical absorption spectra were fitted with Voigt functions using PeakFit software v4.12. No baseline was used for PL emission spectra from solutions. In the case of fitting absorption spectra, the background was removed (for E_{11}, between 780 and 1078 nm and for E_{22}, between 536 and 625 nm) as shown in Figure 4-2.

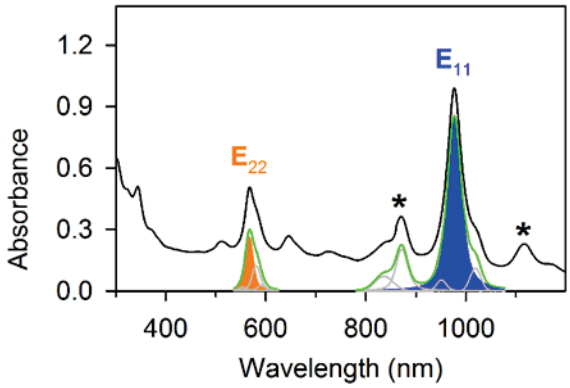

Figure 4-2. The UV-visible-NIR absorption spectrum of (6,5)-SWCNT at the highest concentration used in this study. Absorption spectrum of the $(27 \pm 1) \times 10^{13}$ tube mL^{-1} stock solution of (6,5)-SWCNTs that was subsequently diluted for further studies (black line). The baseline was adjusted and the resultant spectrum (green line) was fit using Voigt functions to obtain the integrated peak area of E_{11} (blue) and amplitude of E_{22} (orange). Other notable components in the solution, the (6,4) and (7,6) chiralities, are indicated by asterisks.

4.2.5. Calculation of the Concentration of the Stock Solution of (6,5)-SWCNTs.

The convolved integrated area of E_{11} (Figure 4-2) obtained from the UV-visible-NIR absorption spectrum of the most concentrated stock solution of (6,5)-SWCNT was used to calculate the concentration of the stock solution. Specifically, the concentration was calculated from the relation outlined in eq. (4-1) given by the work of Streit *et al*.[97]

$$\rho = \frac{2.303A(\bar{\nu})}{l\sigma(\bar{\nu})} \tag{4-1}$$

in which ρ is the number density of carbon atoms, $A(\bar{\nu})$ is the integral of the E_{11} peak (fitted versus frequency in cm^{-1}), l is the optical path length (1 cm), and $\sigma(\bar{\nu})$ is the integral of the absorption cross section, 9.24×10^{-15} cm C^{-1} for (6,5)-SWCNT.[97] Streit *et al*.[97] estimate the uncertainty of this method to be ± 4% so we used this error value throughout this work for each of our calculated concentration values.

4.2.6. Preparation of Films of (6,5)-SWCNTs.

SWCNT films were fabricated using a previously described method by Ng *et al.*[98] in which a solution of SWCNTs were filtered over nitrocellulose membranes (25 nm pore size; Millipore VSWP). The films were used for PL imaging as-prepared and transferred to silicon substrates for atomic force microscopy (AFM) imaging.

4.2.7. Atomic Force Microscopy Imaging.

Silicon substrates were prepared by immersion in a piranha solution for 45 min at 90 °C followed by copious washing with Nanopure™ water before drying with

argon. The substrates were immersed in a 2% (3-aminopropyl) triethoxysilane (APTES)/ethanol solution for 20 min to form a self-assembled monolayer of alkyl amines on the silicon surface. The substrates were then rinsed consecutively with ethanol and Nanopure^{TM} water, and then dried with argon. In the case of determining distributions of SWCNT length, samples were prepared by drop-casting a solution of known concentration of (6,5)-SWCNTs or (6,5)-SWCNT-$C_6H_4NO_2$s onto the surface-modified substrates, followed by heating at 250 °C for 30 min in air. The films were transferred to silicon substrates with pressure in a vise at 110 °C for 1 h as previously described.[98] The filter membrane was removed by an acetone vapor bath (150 °C for 12 h).

Images were obtained using a Veeco Multimode AFM with a Nanoscope III controller, in tapping mode using an Au-coated Si tapping probe. Individual tubes (N = 200 tubes) were counted and measured using the Nanoscope Version 5.3 software (Figure 4-3). The first moment, $\langle L \rangle$ and cube root of the third moment, $\langle L^3 \rangle^{1/3}$, of the length distribution of (6,5)-SWCNTs are 346 and 410 nm, respectively.

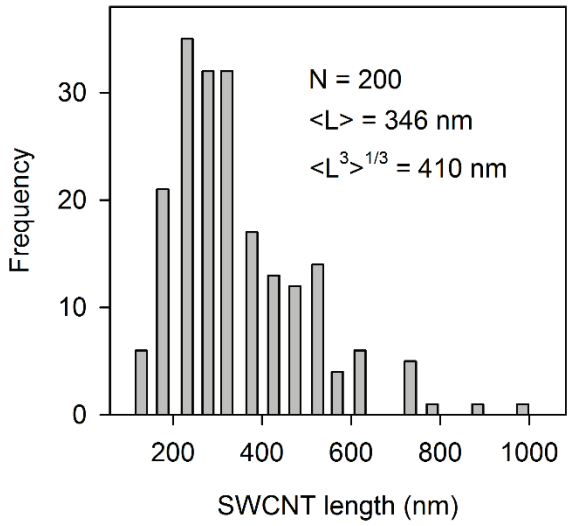

Figure 4-3. Length distribution of (6,5)-SWCNTs determined by atomic force microscopy. 200 individual SWCNTs were measured.

4.3. Results and Discussion

4.3.1. Defining the Dilute and Semi-Dilute Regimes for SWCNT Solutions.

Duggal *et al.*[99] described the concentration boundary below which surfactant-wrapped SWCNTs are able to rotate freely. SWCNTs that are monodispersed in water behave as Brownian rigid rods, due to their high aspect ratio. The Debye equation describes the rotational diffusion of an ensemble of Brownian rigid rods. The equation can be related to the length of the rods, in this case the length of the SWCNTs, to define the boundaries defining the dilute and semi-dilute conditions. Here, the critical concentration, c^*, is defined as the boundary between the dilute and semi-dilute regimes (Figure 4-4). At concentrations above c^*, it is expected that interactions between SWCNTs become significant as they are no longer able to freely rotate in

solution. Duggal *et al.*[99] describe the transition between these two regimes by eq. (4-2).

$$c^* = 2/\langle L^3 \rangle \tag{4-2}$$

in which $\langle L^3 \rangle$ is the third moment of the length distribution of the SWCNTs in solution. In statistics, the third moment describes a distribution's skewness, or asymmetry about the mean. In the case of SWCNTs, $\langle L^3 \rangle$ is related to the volume occupied by a freely rotating SWCNT in solution.

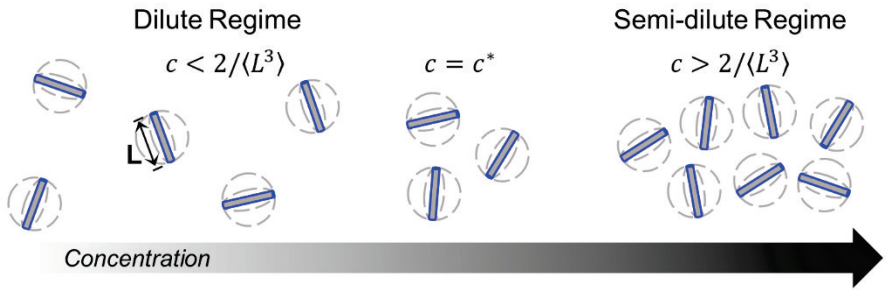

Figure 4-4. The theoretically-predicted limit for collisional self-quenching. Interactions between neighboring SWCNTs are predicted by equations related to the concentration of the solutions of SWCNTs, ranging from the dilute regime where collisions are rare to the semi-dilute regime where interactions become significant. L is the length of the SWCNT.

We used this equation to approximate the boundary beyond which we expect to observe PL self-quenching of the native PL state, E_{11}, due to collisions. We determined the cube root of the third moment, $\langle L^3 \rangle^{1/3}$, of the (6,5)-SWCNTs in our solution to be 410 nm by AFM. By applying the value for $\langle L^3 \rangle$ to eq. (4-2), the c^*, which defines the boundary between the dilute and semi-dilute regimes, was calculated to be (2.8 ± 0.1) × 10^{13} tubes mL^{-1}.

We performed a concentration dependent spectroscopic study, measuring the PL and absorbance of both the chemically modified and unmodified (6,5)-SWCNTs in order to understand how PL from the two emissive states, E_{11} and E_{11}^{-}, evolves as a function of SWCNT concentration. Several sequential dilutions of both the stock solutions of (6,5)-SWCNTs and (6,5)-SWCNT-$C_6H_4NO_2$s were made, spanning the range of the predicted dilute and semi-dilute regimes.

PL measurements reveal distinct trends in each of the two systems (Figure 4-5). In the case of the unmodified (6,5)-SWCNTs, the PL from the native PL state, E_{11} (980 nm), is positively correlated with the SWCNT concentration up to ~ $(2.7 \pm 0.1) \times 10^{13}$ tubes mL^{-1}, which is in good agreement with the predicted c^*, $(2.8 \pm 0.1) \times 10^{13}$ tubes mL^{-1}. Beyond this concentration, PL self-quenching is observed as PL becomes negatively correlated with concentration. In contrast, the defect PL is positively correlated with SWCNT concentration well beyond the dilute regime.

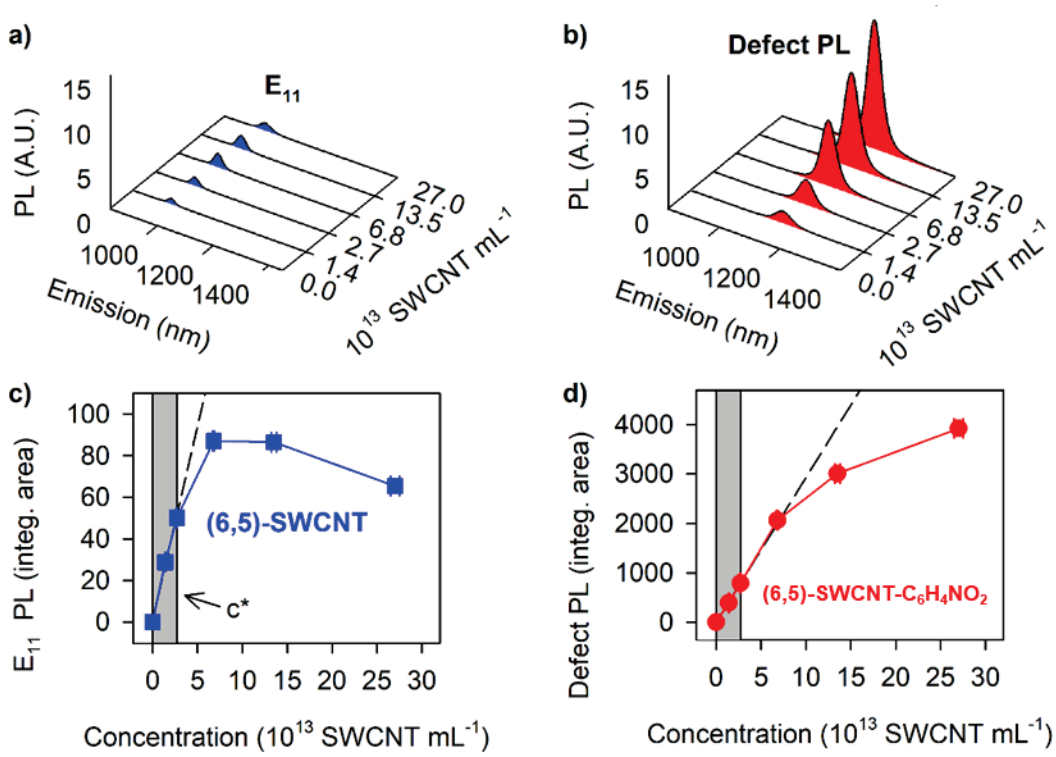

Figure 4-5. The introduction of fluorescent quantum defects pushes the collisional self-quenching limit beyond the theoretically-predicted boundary. Isolated peaks resulting from fitting the PL spectra (λ_{ex} = 565 nm) of (a) unmodified (6,5)-SWCNTs and (b) (6,5)-SWCNT-$C_6H_4NO_2$s show the dramatic difference in trends between PL from E_{11} and defect PL with concentration. (c) PL from the native PL state maintains with concentration within the dilute regime (shaded) but is quenched at higher concentrations. (d) In contrast, defect PL remains positively correlated with the SWCNT concentration throughout the range tested. The dashed black lines in (c) and (d) are provided to guide the eye. The shaded region is the theoretically-predicted dilute region.

The PL from E_{11} in the case of the NO_2-(6,5)-SWCNTs is even more significantly affected (Figure 4-6), possibly due to the shuttling of E_{11} excitons to defect sites.

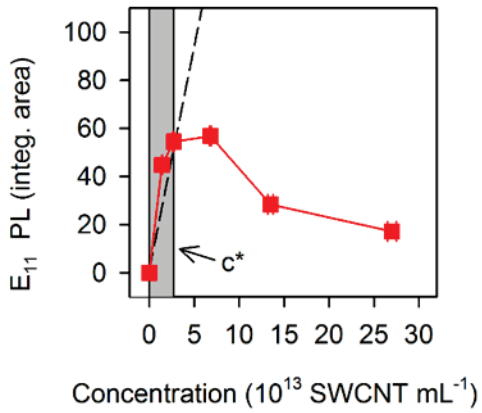

Figure 4-6. PL from E_{11} of the (6,5)-SWCNT-$C_6H_4NO_2$s is rapidly quenched beyond the dilute limit, c*. The dashed line is provided to guide the eye. The shaded region is the theoretically-predicted dilute region.

Further analysis of the PL emission spectra reveals that not only is the PL from E_{11} quenched, but that the peak is also significantly broadened (Table 4-1). We found that the full width at half maximum (FWHM) of PL from E_{11} of the (6,5)-SWCNTs increased by 62%, from 37 to 60 meV, within the range of concentrations tested. This spectral broadening effect is an evidence of strong electronic interactions among SWCNTs at high concentrations. Interestingly, this peak broadening was not observed in the case of the chemically-modified (6,5)-SWCNT-$C_6H_4NO_2$s for either PL state. The lack of broadening suggests that the electronic coupling between neighboring nanotubes is effectively minimized due to the presence of quantum defects which trap the excitons and prevent collisional quenching.

Furthermore, we did not observe any shifts in the emission spectra in our concentration dependent study. The absence of spectral shift suggests that inner filter effects,[96] which would have caused shifts, do not contribute significantly to the concentration dependent effects in E_{11}^-.

Table 4-1 Spectral characteristics of (6,5)-SWCNTs and (6,5)-SWCNT-$C_6H_4NO_2$s. The φ_{rel} was calculated by eq. (4-3). PL peak areas were obtained by spectral fitting.

SWCNT conc. (10^{13} tubes mL^{-1})	**(6,5)-SWCNT**			**(6,5)-SWCNT-$C_6H_4NO_2$**						**φ_{rel}**
	E_{11} (nm)	**FWHM (meV)**	**E_{11} Area**	**E_{11} (nm)**	**FWHM (meV)**	**E_{11} Area**	**E_{11}^- (nm)**	**FWHM (meV)**	**E_{11}^- Area**	
1.40 ± 0.06	980	37	28.8	980	36	44.8	1141	59	392	3.4
2.7 ± 0.1	980	41	50.1	980	35	54.4	1141	56	792	4.0
6.8 ± 0.3	980	45	87.1	980	34	56.8	1141	55	2064	5.9
13.5 ± 0.5	980	48	86.5	980	37	28.4	1141	56	3008	8.7
27 ± 1	980	60	65.4	980	33	17.2	1141	53	3902	34

Upon functionalization, the concentrated solution of (6,5)-SWCNTs exhibits a decrease in absorption (18% loss at E_{11}) and there is no significant peak broadening (Figure 4-7). In direct contrast to the PL study, the absorbance at E_{22} and E_{11} maintains linearity with SWCNT concentration throughout the range tested. This observation is consistent with the fact that the aryl groups are sparse resulting in a low absorbance in the defect state, E_{11}^-, even for highly concentrated SWCNT solutions.

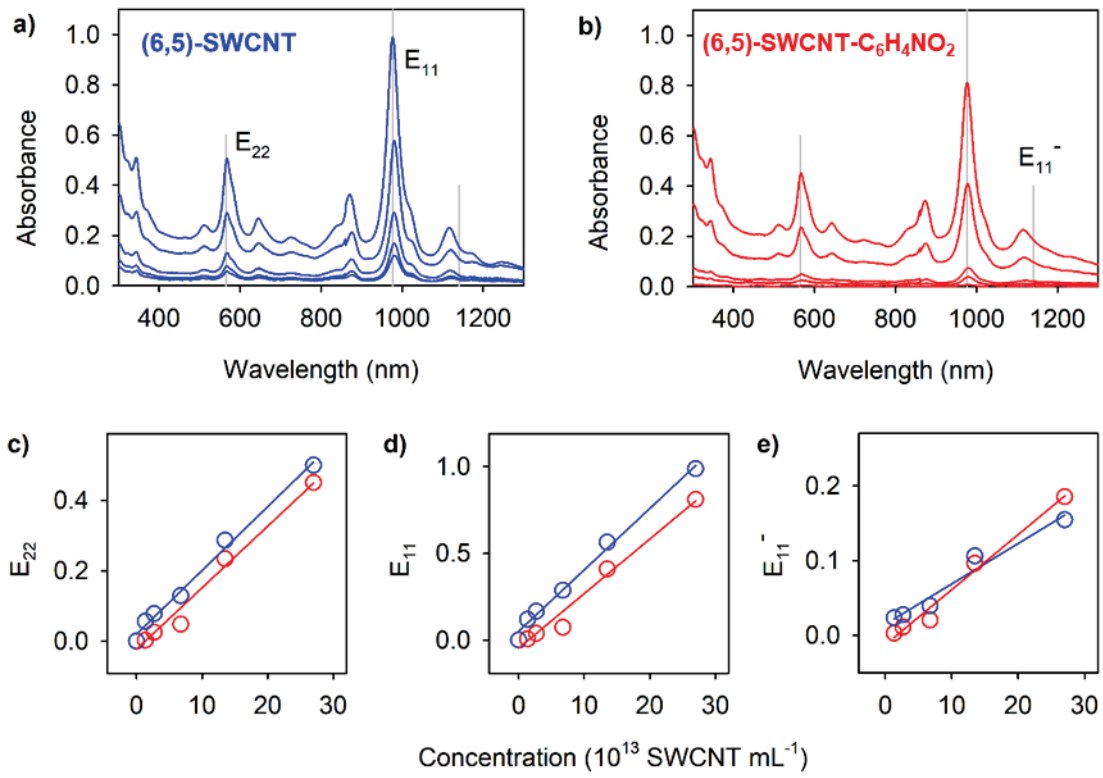

Figure 4-7. Absorption spectra of unmodified and covalently functionalized (6,5)-SWCNTs at various concentrations. Absorption spectra of (a) (6,5)-SWCNT (blue) and (b) (6,5)-SWCNT-$C_6H_4NO_2$ (red) at various tube concentrations do not show concentration-dependence peak shifts. The peak absorbance at (c) E_{22}, (d) E_{11}, and at (e) E_{11}^- is plotted versus SWCNT concentration and are linearly correlated with SWCNT concentration (solid lines are linear regressions). The peak amplitude data was obtained by spectral fitting in the case of E_{11} and E_{22}. Note that the concentration of the defects is extremely low so the E_{11}^- absorption peak is not distinguishable from that of the spectra. The grey lines in (a) and (b) show the positions of the notable absorbance peaks.

4.3.2. PL Brightness of Chemically-Modified SWCNTs at High Concentrations.

PL brightness is an important property for quantum emitters. Understanding how the defect PL evolves with concentration is vital for obtaining bright emission for real life applications. The PL brightness of the two systems, (6,5)-SWCNT-$C_6H_4NO_2$ and (6,5)-SWCNTs was compared by calculating the relative efficiency of converting an absorbed photon to observed emission, φ_{rel}, using eq. (4-3).

$$\varphi_{rel} = C \times \frac{A_{E11-}}{A_{E11}} \tag{4-3}$$

in which A_{E11-} and A_{E11} are the integrated areas of the PL peaks at E_{11}^- for the functionalized system and E_{11} of the unfunctionalized system, respectively. C takes into account the difference in the absorption cross-sections between the unmodified (6,5)-SWCNTs and the (6,5)-SWCNT-$C_6H_4NO_2$s and is given by eq. (4-4).

$$C = OD_{E22}(p)/OD_{E22}(d) \tag{4-4}$$

in which $OD_{E22}(p)$ and $OD_{E22}(d)$ are equal to the amplitudes of the absorption peaks at E_{22} (565 nm) for the unmodified (6,5)-SWCNTs and chemically modified (6,5)-SWCNT-$C_6H_4NO_2$s, respectively.

The φ_{rel} maintains a positive trend with SWCNT concentration throughout the range tested (Figure 4-8). In fact, defect PL from the most concentrated solution measured, $(27 \pm 1) \times 10^{13}$ SWCNT mL^{-1}, is 34-times brighter than the native E_{11} exciton at the same concentration. The PL enhancement becomes most significant at high tube concentrations, meaning that the functionalized SWCNTs are still efficient emitters even at high concentration.

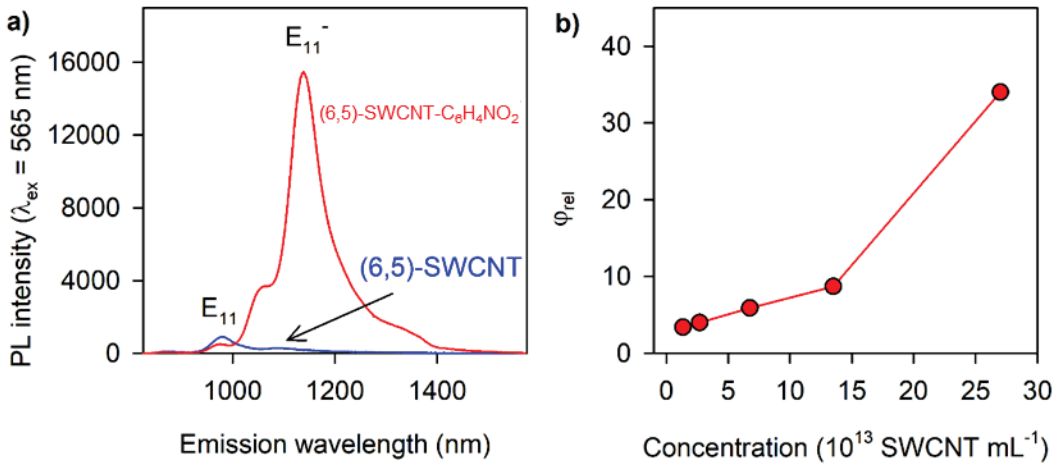

Figure 4-8. PL in concentrated solutions of quantum defect-tailored SWCNTs. (a) PL emission spectra of the stock solutions, (27 ± 1) x 10^{13} tubes mL^{-1}, of (6,5)-SWCNTs (blue) and (6,5)-SWCNT-$C_6H_4NO_2$s (red). (b) Due to the quenching of E_{11} PL at high concentrations, φ_{rel} increases substantially with nanotube concentrations throughout the range tested.

4.3.3. A SWCNT Film as a Limiting Case of Highly Concentrated Systems.

To probe the effectiveness of our strategy in the concentration limit, we measured the PL from films of the (6,5)-SWCNT-$C_6H_4NO_2$s. Strong interactions between SWCNTs dramatically quench E_{11} PL in solution.[100] Despite this, we found that defect PL is more resistant to self-quenching than PL from E_{11} even in dense films (Figure 4-9). Notably, upon doubling the film density, from 0.18 to 0.36 μg of C cm^{-2}, emission from E_{11} is nearly completely lost. In contrast, defect PL retains 80% of its integral peak area. Interestingly, both peaks suffer from considerable red shifts in this densely packed system, but the emission from the E_{11}^- state shifts more, 20 meV versus 12 meV, despite the defect state's smaller absorbance cross section. These shifts may

be the result of inner filter effects, which cause selective absorption of the high energy regions of emission spectra, shifting emission wavelengths[94] in the case of the films.

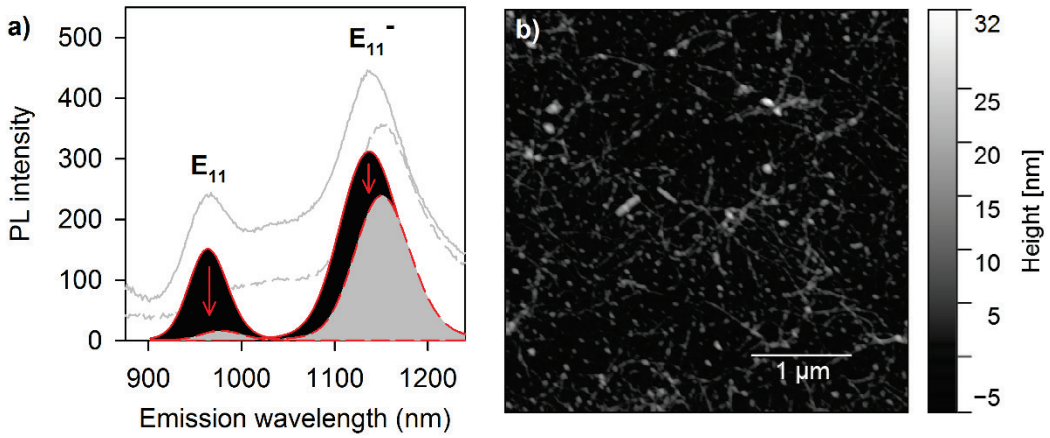

Figure 4-9. Defect PL from a film of (6,5)-SWCNT-$C_6H_4NO_2$s is more resistant to self-quenching than the PL from E_{11}. (a) When the film density is doubled from 0.18 to 0.36 µg of C cm^{-2} (solid and dashed grey lines, respectively), defect PL retains more of its initial emission peak area than does E_{11} (λ_{ex} = 565 nm). The deconvolved peak areas are shaded black and grey for the low and high concentrations, respectively. (b) An AFM image of the 0.18 µg of C cm^{-2} film on silicon shows clearly resolved SWCNTs are in a densely packed, concentrated system.

4.3.4. Chemical Modification of SWCNTs Introduces a New Emission Route to Bypass Self-Quenching.

The results presented here support the idea that sparse defects on nanostructures channel excitons to localized emission centers that can emit photons for which the bulk carbon lattice is transparent. Unmodified SWCNTs, lacking such emission outlets, emit primarily from E_{11}. The PL from this state is readily quenched by neighboring SWCNTs at high concentrations, due to the nearly complete spectral overlap with

absorption at this position (10 meV Stokes shift). In the case of the functionalized system the sparse defects are the sites for emission of photons that are 190 meV red-shifted from that of the E_{11} exciton. This considerable increase in the Stokes shift of the system nearly eliminates spectral overlap with the strong E_{11} absorption band. Because the aryl defects are at low densities on the carbon lattice, the E_{11}^- state does not have a significant absorption cross-section, making the carbon lattice nearly transparent to defect PL.

4.4 Conclusions

It was demonstrated that defect PL can reduce self-quenching in highly concentrated systems of SWCNTs modified with low densities of covalent defects. The critical concentration at which SWCNTs collide with each other, was calculated by a nanotube rotational diffusion model[99] to be $(2.8 \pm 0.1) \times 10^{13}$ tubes mL^{-1}. This value is in good agreement with our measurements from the concentration dependent study of the native E_{11} PL from unmodified (6,5)-SWCNTs. Through the introduction of aryl groups onto the SWCNTs, we extended the onset of self-quenching two-fold via the red-shifted emission from the defect-induced PL state. At the highest concentration tested, the (6,5)-SWCNT-$C_6H_4NO_2$ are still 34-times brighter than the unmodified SWCNTs. We explored the self-quenching in a highly dense system, a film of (6,5)-SWCNT-$C_6H_4NO_2$s and found that defect PL is still more efficient than that of the native exciton. We attribute these observations to the energy mismatch of defect PL with the absorbance of the bulk lattice. Our study demonstrates that defect PL can be

used to dramatically improve the optical performance of SWCNTs at high concentrations.

Chapter 5: Summary and Outlook

5.1. Summary

This dissertation addressed issues fundamental to the precise creation of fluorescent quantum defects, which were introduced in Chapter I. In the Chapter II, it was demonstrated that light could be used to drive covalent modification of single-walled carbon nanotubes (SWCNTs) using aryldiazonium salts. Wavelength-dependent studies revealed that the reaction could be driven with light that resonates with the SWCNT chirality, as opposed to the spontaneous reactions of the aryldiazonium salts. This finding led to development of a method for chirality selective functionalization of SWCNTs by optically selecting them within a mixture, as discussed in Chapter III.

Chirality-selectivity was made possible by applying the optical selection technique to a derivative of an aryldiazonium salt, a diazoether, which is in an unreactive state with semiconducting SWCNTs until being triggered by light excitation of the nanotube. The conformational isomers of the diazoether, which have distinct reactivity for semiconducting SWCNTs, were synthesized. It was found that the thermodynamic barrier of isomerization from the inactive *E*-isomer of diazoether to the reactive *Z*-isomer could be tuned with pH. This finding was confirmed with density functional theory calculations of the thermodynamic barrier to isomerization from the *E*-to-*Z* conformations. The reactivity could even be switched on and off at will (within the limit of our sensitive spectroscopic detection technique) by tuning the pH of the

solution. Careful tuning of reaction conditions led to functionalization of an otherwise less reactive SWCNT chirality, (7,3) versus (6,5).

In Chapter IV, it was demonstrated that the quenching of PL in highly concentrated solutions of SWCNTs could be bypassed by chemically introducing a new emission route, fluorescent quantum defects. The phenomenon was extended from solutions of SWCNTs to thin films of SWCNTs, paving the way for future work on spatially-patterning fluorescent quantum defects on thin films of SWCNT.

5.2. Outlook for Fluorescent Quantum Defects.

5.2.1. Generation of a New Class of Nanomaterials.

An entirely new class of nanomaterials may be synthesized by the incorporation of fluorescent quantum defects into different SWCNT chiralities.[43] The addition of different functional groups to the same SWCNT chirality results in an array of molecules, each with unique optical and electronic properties. However, the number of chemistries that have been used for creating these defects remains small. Application of other well-studied organic reactions to SWCNTs and the optically-driven technique will generate materials with new functionality, not only chemically but also optically and electronically. Many of the applications envisioned for this new class of materials will require fine control of doping densities, even to the point of introducing solitary dopants on individual SWCNTs.[54] This may be another route to spin-coupled optics,[10, 101] and non-classical light sources[102] among others applications. In this dissertation, an optical technique to drive functionalization and a chemistry which has a large barrier to reaction with semiconducting SWCNTs. Using this optical technique as a model, the

method may be expanded to other chemistries to generate even more unique molecularly tunable fluorescent quantum defects.[43]

5.2.2. The Geometry of Functional Groups at a Fluorescent Quantum Defect.

While it has been observed that the defect PL originates from localized sites on SWCNTs,[40] the specific geometry and arrangement of functional groups at these bright sites is not well-understood. In fact, depending on the chemistry, it has been reported that defects can exist as solitary functional sites[54] or even propagate to form banded structures.[103] Furthermore, it would be interesting to clarify the effect that the optical excitation technique has on the geometry of the resulting defects.

The use of high resolution hyperspectral imaging may make it possible to uncover the atomic arrangement of fluorescent quantum defects on SWCNTs. This technique may even permit observation of the covalent bonding reactions *in situ*. Understanding how defects assemble and revealing the relative geometry of the defects is key for understanding the fundamental physics behind fluorescent quantum defects.

5.2.3. Patterns of Spatially-Resolved Fluorescent Quantum Defects on Thin Films of SWCNTs.

When coupled with the optical selection technique, the diazoether chemistry results in unprecedented structural selectivity in functionalization among different SWNCT chiralities within a solution. However, the spatial selectivity of this chemistry on a thin film of SWCNTs has not been explored. Various functional groups could be patterned onto thin films of SWCNTs using light to precisely drive their covalent attachment. These patterns of fluorescent quantum defects could be used for generating

a multiplex of sensors on a small device. It is expected that with fine-tuning, the technique could be used to pattern a single defect on a SWCNT, the ideal fluorescent quantum defect for further studies.

Bibliography

1. Tilley, R. J. D., *Principles and applications of chemical defects*. Stanley Thomas: Gloucestershire, England, 1998.

2. William, D.; Callister, J.; Rethwisch, D. G., *Materials science and engineering: An introduction*. 8 ed.; Wiley: 2010.

3. Hiramatsu, H.; Ueda, K.; Ohta, H.; Hirano, M.; Kamiya, T.; Hosono, H., *Thin Solid Films* **2003,** *445*, 304-308.

4. Smithsonian. The History of the Hope Diamond. https://www.si.edu/spotlight/hope-diamond (accessed February 21, 2017).

5. Collins, P. G., *Defects and disorder in carbon nanotubes*. 2010.

6. Schubert, E. F., *Doping in III-V semiconductors*. 1st ed.; Cambridge University Press: Cambridge, 1993.

7. Voiry, D.; Goswami, A.; Kappera, R.; SilvaCecilia de Carvalho Castro, e.; Kaplan, D.; Fujita, T.; Chen, M.; Asefa, T.; Chhowalla, M., *Nat. Chem.* **2015,** *7*, 45-49.

8. Ghosh, S.; Bachilo, S. M.; Simonette, R. A.; Beckingham, K. M.; Weisman, R. B., *Science* **2010,** *330*, 1656-1659.

9. Piao, Y.; Meany, B.; Powell, L. R.; Valley, N.; Kwon, H.; Schatz, G. C.; Wang, Y., *Nat. Chem.* **2013,** *5*, 840-845.

10. Kurtsiefer, C.; Mayer, S.; Zarda, P.; Weinfurter, H., *Phys. Rev. Lett.* **2000,** *85*, 290-293.

11. Iijima, S., *Nature* **1991,** *354*, 56-8.

12. Bethune, D. S.; Kiang, C. H.; deVries, M. S.; Gorman, G.; Savoy, R.; Vazquez, J.; Beyers, R., *Nature* **1993,** *363*, 605-7.

13. Iijima, S.; Ichihashi, T., *Nature* **1993,** *363*, 603-5.

14. Qian, D.; Wagner, G. J.; Liu, W. K.; Yu, M. F.; Ruoff, R. S., *Appl. Mech. Rev.* **2002,** *55*, 495-532.

15. De Volder, M. F. L.; Tawfick, S. H.; Baughman, R. H.; Hart, A. J., *Science* **2013,** *339*, 535-539.

16. Riggs, J. E.; Guo, Z.; Carroll, D. L.; Sun, Y.-P., *J. Am. Chem. Soc.* **2000,** *122*, 5879-5880.

17. Pop, E.; Mann, D.; Wang, Q.; Goodson, K.; Dai, H., *Nano Lett.* **2006,** *6*, 96-100.

18. Weisman, R. B., Optical spectroscopy of single-walled carbon nanotubes. In *Contemporary Concepts of Condensed Matter Science*, Saito, S.; Zettl, A., Eds. Elsevier: 2008; Vol. Volume 3, pp 109-133.

19. Avouris, P.; Freitag, M.; Perebeinos, V., *Nat. Photonics* **2008,** *2*, 341-350.

20. Zheng, L. X.; O'Connell, M. J.; Doorn, S. K.; Liao, X. Z.; Zhao, Y. H.; Akhadov, E. A.; Hoffbauer, M. A.; Roop, B. J.; Jia, Q. X.; Dye, R. C.; Peterson, D. E.; Huang, S. M.; Liu, J.; Zhu, Y. T., *Nat. Mater.* **2004,** *3*, 673-676.

21. Seol;, G.; Yoon, Y.; Fodor, J. K.; Guo, J.; Matsudaira, A.; Kienle, D.; Liang, G.; Klimeck, G.; Lundstrom, M.; Saeed, A. I. *CNTbands*, 2014.

22. Scholes, G. D.; Rumbles, G., *Nat. Mater.* **2006,** *5*, 683-696.

23. Wang, F.; Dukovic, G.; Brus, L. E.; Heinz, T. F., *Science* **2005,** *308*, 838-841.

24. Frenkel, J., *Phys. Rev.* **1931,** *37*, 17-44.

25. Yang, L.; Anantram, M. P.; Han, J.; Lu, J. P., *Phys. Rev. B* **1999,** *60*, 13874-13878.

26. O'Connell, M. J.; Bachilo, S. H.; Huffman, C. B.; Moore, V. C.; Strano, M. S.; Haroz, E. H.; Rialon, K. L.; Boul, P. J.; Noon, W. H.; Kittrell, C.; Ma, J.; Hauge, R. H.; Weisman, R. B.; Smalley, R. E., *Science* **2002,** *297*, 593-596.

27. Hagen, A.; Steiner, M.; Raschke, M. B.; Lienau, C.; Hertel, T.; Qian, H.; Meixner, A. J.; Hartschuh, A., *Phys. Rev. Lett.* **2005,** *95*.

28. Crochet, J.; Clemens, M.; Hertel, T., *J. Am. Chem. Soc.* **2007,** *129*, 8058-8059.

29. Shaver, J.; Kono, J.; Portugall, O.; Krstiċ, V.; Rikken, G. L. J. A.; Miyauchi, Y.; Maruyama, S.; Perebeinos, V., *Nano Lett.* **2007,** *7*, 1851-1855.

30. Scholes, G. D.; Tretiak, S.; McDonald, T. J.; Metzger, W. K.; Engtrakul, C.; Rumbles, G.; Heben, M. J., *J. Phys. Chem. C* **2007,** *111*, 11139-11149.

31. Lee, A. J.; Wang, X.; Carlson, L. J.; Smyder, J. A.; Loesch, B.; Tu, X.; Zheng, M.; Krauss, T. D., *Nano Lett.* **2011,** *11*, 1636-1640.

32. Hong, G.; Lee, J. C.; Robinson, J. T.; Raaz, U.; Xie, L.; Huang, N. F.; Cooke, J. P.; Dai, H., *Nat. Med.* **2012,** *18*, 1841-1846.

33. Welsher, K.; Sherlock, S. P.; Dai, H., *Proc. Natl. Acad. Sci. U. S. A.* **2011,** *108*, 8943-8948.

34. Heller, D. A.; Baik, S.; Eurell, T. E.; Strano, M. S., *Adv. Mater.* **2005,** *17*, 2793-2799.

35. Barone, P. W.; Baik, S.; Heller, D. A.; Strano, M. S., *Nat. Mater.* **2005,** *4*, 86-92.

36. Hata, K.; Futaba, D. N.; Mizuno, K.; Namai, T.; Yumura, M.; Iijima, S., *Science* **2004,** *306*, 1362-1364.

37. Nikolaev, P.; Bronikowski, M. J.; Bradley, R. K.; Rohmund, F.; Colbert, D. T.; Smith, K. A.; Smalley, R. E., *Chem. Phys. Lett.* **1999,** *313*, 91-97.

38. Cognet, L.; Tsyboulski, D. A.; Rocha, J.-D. R.; Doyle, C. D.; Tour, J. M.; Weisman, R. B., *Science* **2007,** *316*, 1465-1468.

39. Crochet, J. J.; Duque, J. G.; Werner, J. H.; Doorn, S. K., *Nat. Nanotechnol.* **2012,** *7*, 126-132.

40. Hartmann, N. F.; Yalcin, S. E.; Adamska, L.; Haroz, E. H.; Ma, X.; Tretiak, S.; Htoon, H.; Doorn, S. K., *Nanoscale* **2015,** *7*, 20521-20530.

41. Ramirez, J.; Mayo, M. L.; Kilina, S.; Tretiak, S., *Chem. Phys.* **2013,** *413*, 89-101.

42. Brozena, A. H.; Leeds, J. D.; Zhang, Y.; Fourkas, J. T.; Wang, Y., *ACS Nano* **2014,** *8*, 4239-4247.

43. Kwon, H.; Furmanchuk, A.; Kim, M.; Meany, B.; Guo, Y.; Schatz, G. C.; Wang, Y., *J. Am. Chem. Soc.* **2016,** *138*, 6878-6885.

44. Miyauchi, Y.; Iwamura, M.; Mouri, S.; Kawazoe, T.; Ohtsu, M.; Matsuda, K., *Nat. Photon.* **2013,** *7*, 715-719.

45. Barbieri, A.; Bandini, E.; Monti, F.; Praveen, V. K.; Armaroli, N., *Top. Curr. Chem.* **2016,** *374*, 47.

46. Hartmann, N. F.; Velizhanin, K. A.; Haroz, E. H.; Kim, M.; Ma, X.; Wang, Y.; Htoon, H.; Doorn, S. K., *ACS Nano* **2016,** *10*, 8355-8365.

47. Iwamura, M.; Akizuki, N.; Miyauchi, Y.; Mouri, S.; Shaver, J.; Gao, Z.; Cognet, L.; Lounis, B.; Matsuda, K., *ACS Nano* **2014,** *8*, 11254-11260.

48. Akizuki, N.; Aota, S.; Mouri, S.; Matsuda, K.; Miyauchi, Y., *Nat. Commun.* **2015,** *6*, 2-6.

49. Shiraishi, T.; Juhász, G.; Shiraki, T.; Akizuki, N.; Miyauchi, Y.; Matsuda, K.; Nakashima, N., *J. Phys. Chem C.* **2016,** *120*, 15632-15639.

50. Kim, M.; Adamska, L.; Hartmann, N. F.; Kwon, H.; Liu, J.; Velizhanin, K. A.; Piao, Y.; Powell, L. R.; Meany, B.; Doorn, S. K.; Tretiak, S.; Wang, Y., *J. Phys. Chem. C* **2016,** *120*, 11268-11276.

51. Kwon, H.; Kim, M.; Meany, B.; Piao, Y.; Powell, L. R.; Wang, Y., *J. Phys. Chem. C* **2015,** *119*, 3733-3739.

52. Ma, X.; Hartmann, N. F.; BaldwinJon, K. S.; Doorn, S. K.; Htoon, H., *Nat. Nanotechnol.* **2015,** *10*, 671-675.

53. Högele, A.; Galland, C.; Winger, M.; Imamoğlu, A., *Phys. Rev. Lett.* **2008,** *100*, 217401.

54. Wilson, H.; Ripp, S.; Prisbrey, L.; Brown, M. A.; Sharf, T.; Myles, D. J. T.; Blank, K. G.; Minot, E. D., *J. Phys. Chem. C* **2016,** *120*, 1971-1976.

55. Bahr, J. L.; Yang, J.; Kosynkin, D. V.; Bronikowski, M. J.; Smalley, R. E.; Tour, J. M., *J. Am. Chem. Soc.* **2001,** *123*, 6536-6542.

56. Strano, M. S.; Dyke, C. A.; Usrey, M. L.; Barone, P. W.; Allen, M. J.; Shan, H.; Kittrell, C.; Hauge, R. H.; Tour, J. M.; Smalley, R. E., *Science* **2003,** *301*, 1519-1522.

57. Bekyarova, E.; Sarkar, S.; Wang, F.; Itkis, M. E.; Kalinina, I.; Tian, X.; Haddon, R. C., *Acc. Chem. Res.* **2013,** *46*, 65-76.

58. Schmidt, G.; Gallon, S.; Esnouf, S.; Bourgoin, J.-P.; Chenevier, P., *Chem.-Eur. J.* **2009,** *15*, 2101-2110.

59. Tour, J. M.; Bahr, J. L.; Yang, J. Process for derivatizing carbon nanotubes with diazonium species. 2007.

60. Liu, H.; Ryu, S.; Chen, Z.; Steigerwald, M. L.; Nuckolls, C.; Brus, L. E., *J. Am. Chem. Soc.* **2009,** *131*, 17099-17101.

61. Balasubramanian, K.; Burghard, M., *Small* **2005,** *1*, 180-192.

62. Liu, H.; Nishide, D.; Tanaka, T.; Kataura, H., *Nat. Commun.* **2011,** *2*, 309.

63. Powell, L. R.; Piao, Y.; Wang, Y., *J. Phys. Chem. Lett.* **2016,** *7*, 3690-3694.

64. Usrey, M. L.; Lippmann, E. S.; Strano, M. S., *J. Am. Chem. Soc.* **2005,** *127*, 16129-16135.

65. Naumov, A. V.; Ghosh, S.; Tsyboulski, D. A.; Bachilo, S. M.; Weisman, R. B., *ACS Nano* **2011,** *5*, 1639-1648.

66. Reich, S.; Dworzak, M.; Hoffmann, A.; Thomsen, C.; Strano, M. S., *Phys. Rev. B* **2005,** *71*, 033402.

67. Eaton, D. F., *Pure Appl. Chem.* **1988,** *60*, 1107-14.

68. Andrieux, C. P.; Pinson, J., *J. Am. Chem. Soc.* **2003,** *125*, 14801-14806.

69. Tanaka, Y.; Hirana, Y.; Niidome, Y.; Kato, K.; Saito, S.; Nakashima, N., *Angew. Chem. Int. Ed.* **2009,** *48*, 7655-7659.

70. Saito, R.; Dresselhaus, G.; Dresselhaus, M. S., *Physical properties of carbon nanotubes*. Imperial College Press: London, 1998.

71. Xie, X.; Wahab, M. A.; Li, Y.; Islam, A. E.; Tomic, B.; Huang, J.; Burns, B.; Seabron, E.; Dunham, S. N.; Du, F.; Lin, J.; Wilson, W. L.; Song, J.; Huang, Y.; Alam, M. A.; Rogers, J. A., *J. App. Phys.* **2015,** *117*, 134303.

72. Jain, R. M.; Howden, R.; Tvrdy, K.; Shimizu, S.; Hilmer, A. J.; McNicholas, T. P.; Gleason, K. K.; Strano, M. S., *Adv. Mater.* **2012,** *24*, 4436-4439.

73. Diao, S.; Hong, G.; Robinson, J. T.; Jiao, L.; Antaris, A. L.; Wu, J. Z.; Choi, C. L.; Dai, H., *J. Am. Chem. Soc.* **2012,** *134*, 16971-16974.

74. Hersam, M. C., *Nat. Nanotechnol.* **2008,** *3*, 387-394.

75. Ao, G.; Streit, J. K.; Fagan, J. A.; Zheng, M., *J. Am. Chem. Soc.* **2016,** *138*, 16677-16685.

76. Khripin, C. Y.; Fagan, J. A.; Zheng, M., *J. Am. Chem. Soc.* **2013,** *135*, 6822-5.

77. Darchy, L.; Hanifi, N.; Vialla, F.; Voisin, C.; Bayle, P.-A.; Genovese, L.; Celle, C.; Simonato, J.-P.; Filoramo, A.; Derycke, V.; Chenevier, P., *Carbon* **2014,** *66*, 246-258.

78. Wang, C.; Xu, W.; Zhao, J.; Lin, J.; Chen, Z.; Cui, Z., *J Mater Sci* **2014,** *49*, 2054-2062.

79. Kim, W.-J.; Usrey, M. L.; Strano, M. S., *Chem. Mater.* **2007,** *19*, 1571-1576.

80. Do, Y.-J.; Lee, J.-H.; Choi, H.; Han, J.-H.; Chung, C.-H.; Jeong, M.-G.; Strano, M. S.; Kim, W.-J., *Chem. Mater.* **2012,** *24*, 4146-4151.

81. Doyle, C. D.; Rocha, J.-D. R.; Weisman, R. B.; Tour, J. M., *J. Am. Chem. Soc.* **2008,** *130*, 6795-6800.

82. Chiu, C. F.; Saidi, W. A.; Kagan, V. E.; Star, A., *J. Am. Chem. Soc.* **2017**.

83. Doyle, M. P.; Nesloney, C. L.; Shanklin, M. S.; Marsh, C. A.; Brown, K. C., *J. Org. Chem.* **1989,** *54*, 3785-3789.

84. Frisch, M. J. T., G. W.; Schlegel, H. B.; Scuseria, G. E.; Robb, M. A.; Cheeseman, J. R.; Scalmani, G.; Barone, V.; Mennucci, B.; Petersson, G. A.; et al. *Gaussian 09*, Gaussian, Inc.: Wallingford, CT, 2009.

85. Tomasi, J.; Mennucci, B.; Cancès, E., *J. Mol. Struct.: THEOCHEM* **1999,** *464*, 211-226.

86. Zollinger, H., *Diazo Chemistry I: Aromatic and Heteroaromatic Compounds*. Wiley-VCH: Weinheim, Germany, 1994.

87. Bravo-Diaz, C. D., Diazohydroxides, diazoethers and related species. In *The Chemistry of Hydroxylamines, Oximes and Hydroxamic Acids*, Rappoport, Z.; Liebman, J. F., Eds. John Wiley and Sons: England, 2011; Vol. 2.

88. Hanson, P.; Jones, J. R.; Taylor, A. B.; Walton, P. H.; Timms, A. W., *J. Chem. Soc., Perkin Trans. 2* **2002**, 1135-1150.

89. Wang, C.; Meany, B.; Wang, Y., *Angewandte Chemie International Edition* **2017,** *56*, 9326-9330.

90. Weisman, R. B.; Bachilo, S. M., *Nano Lett.* **2003,** *3*, 1235-1238.

91. Chiu, C. F.; Saidi, W. A.; Kagan, V. E.; Star, A., *J. Am. Chem. Soc.* **2017**.

92. Tsyboulski, D. A.; Rocha, J.-D. R.; Bachilo, S. M.; Cognet, L.; Weisman, R. B., *Nano Lett.* **2007,** *7*, 3080-3085.

93. Leeds, J. D.; Fourkas, J. T.; Wang, Y., *Small* **2013,** *9*, 241-247.

94. Kadria-Vili, Y.; Sanchez, S. R.; Bachilo, S. M.; Weisman, R. B., *ECS J. Solid State Sci. Technol.* **2017,** *6*, M3097-M3102.

95. Xie, J.; Lee, S.; Chen, X., *Adv. Drug Delivery Rev.* **2010,** *62*, 1064-1079.

96. Lakowicz, R., *Principles of fluorescence spectroscopy*. Springer: New York, NY, 2006.

97. Streit, J. K.; Bachilo, S. M.; Ghosh, S.; Lin, C.-W.; Weisman, R. B., *Nano Lett.* **2014,** *14*, 1530-1536.

98. Ng, A. L.; Sun, Y.; Powell, L.; Sun, C.-F.; Chen, C.-F.; Lee, C. S.; Wang, Y., *Small* **2015,** *11*, 96-102.

99. Duggal, R.; Pasquali, M., *Phys. Rev. Lett.* **2006,** *96*, 246104/1-246104/4.

100. Kozák, O.; Sudolská, M.; Pramanik, G.; Cígler, P.; Otyepka, M.; Zbořil, R., *Chem. Mater.* **2016,** *28*, 4085-4128.

101. Viswanatha, R.; Pietryga, J. M.; Klimov, V. I.; Crooker, S. A., *Phys. Rev. Lett.* **2011,** *107*, 067402.

102. Koenraad, P. M.; Flatte, M. E., *Nat. Mater.* **2011,** *10*, 91-100.

103. Deng, S.; Zhang, Y.; Brozena, A. H.; Mayes, M. L.; Banerjee, P.; Chiou, W.-A.; Rubloff, G. W.; Schatz, G. C.; Wang, Y., *Nat. Commun.* **2011,** *2*, 382.